2023-08-01

The Effects Of Process Parameters On The Cyclical Life Of Ti-6al-4v Manufactured Via Laser Powder Bed Fusion

Brandon Ramirez
University of Texas at El Paso

THE EFFECTS OF PROCESS PARAMETERS ON THE CYCLICAL LIFE OF TI-6AL-4V MANUFACTURED VIA LASER POWDER BED FUSION

BRANDON RAMIREZ

Master's Program in Mechanical Engineering

APPROVED:

Francisco Medina, Ph.D., Chair

Ryan B Wicker, Ph.D.

Amit J. Lopes, Ph.D.

Stephen L. Crites, Jr., Ph.D.
Dean of the Graduate School

THE EFFECTS OF PROCESS PARAMETERS ON THE CYCLICAL LIFE OF TI-6AL-4V MANUFACTURED VIA LASER POWDER BED FUSION

by

BRANDON RAMIREZ

THESIS

Presented to the Faculty of the Graduate School of

The University of Texas at El Paso

in Partial Fulfillment

of the Requirements

for the Degree of

MASTER OF SCIENCE

Department of Mechanical Engineering

THE UNIVERSITY OF TEXAS AT EL PASO

August 2023

Abstract

Additive manufacturing via Laser Powder Bed Fusion (LPBF) has already proven revolutionary technology. Due to its favorable strength-to-weight ratio, ti-6Al-4V, a popular titanium alloy, has already been implemented in the aerospace industry for various components. However, the quality validation in additively manufactured parts has always been an issue of concern, specifically under cyclic loading. Ti-6Al-4V samples were printed using LPBF with various process parameters to investigate these conditions further. The build was stress-relieved; however, the samples underwent no other post-processes maintaining their as-built surface. The process parameters were separated into five categories, including various laser powers and printing speeds, allowing for defects such as keyholing and Lack of Fusion (LoF). Furthermore, the other three chosen parameters were printed within the process window at separate locations. Cyclical flexural loading experiments were conducted using a 4-point bending fixture and a servo-hydraulic testing machine by MTS to investigate the fatigue life at various stress levels within the elastic region. Preliminary data from the experimentation of these unmachined rectangular specimens are presented and categorized by their printing parameters to compare their fatigue life under flexural conditions.

Table of Contents

List of Tables

List of Figures

List of Equations

Chapter 1: Introduction.

Additive Manufacturing (AM), the process in which 3D CAD data is taken and manufactured in layer-by-layer methods, has revolutionized the manufacturing industry due to the ability to manufacture components with fewer limitations [1]. This has resulted in manufactured components with faster lead times, more geometric freedom, and less material waste [2]. The advantages of AM can be seen when compared to its opposite, subtractive manufacturing, where an excess of material is removed until the desired geometry is reached. Although subtractive manufacturing is widely used, its limitations are far greater than AM. These benefits have been noticed, and AM has been adopted by various industries, including but not limited to the healthcare, automotive, aerospace, and manufacturing industries [3]. One of the most popular forms of metal AM is laser powder bed fusion (LPBF) where a laser selectively melts a layer of powered feedstock to a specific geometry to sinter the powder together [4]. Each layer is collectively built upon one another until the desired 3D geometry is constructed, and the build plate removal and the stress-relieving process can begin. Although LPBF does allow for greater design freedom, the parameters in which a part is printed will vary the mechanical properties, density, and surface finish [5]. In addition, there is no set of optimal parameters that can always be used to manufacture high-quality parts because there are a great number of variables that impact the final result. Some of the many variables include laser power, laser velocity, layer height, and scanning strategies that can vary the outcome of a printed part [6]. However, as mentioned earlier, these parameters are user-defined and can easily be altered. On the other hand, powder density, morphology, and distribution are some parameters that cannot be altered but also significantly affect repeatability in manufacturing components [7].

The research on finding the optimal printing parameters is abundant and does give insight into what parameters should be considered when printing. However, these parameters must also be coupled with post-processing methods such as stress-relieving, surface machining, and heat treatments to achieve the desired porosity or mechanical properties [8]. This increases the lead time of LBPF printed components and significantly increases the variability of behavior amongst printed parts [8], [9]. For example, when testing different heat treatments on samples printed using the same parameters and powder feedstock, it is evident that mechanical properties are altered due to microstructural changes [10].

This paper aims to investigate some of the effects these process parameters have on the flexural cyclical life of Ti-6Al-4V, an aerospace-grade alloy. This material was chosen specifically due to its popularity and favorable mechanical properties. Four-point bending cyclical tests were conducted because most manufactured components will likely be exposed to repeated loadings throughout their life versus monotonic compression or tensile loadings. The tested specimens did not undergo post-processing methods other than general stress-relieving to maintain their as-built surface. The validity of additively manufactured parts is imperative to ensure they meet quality and safety standards while allowing for repeatability. To investigate and give insight into the effects of process parameters, the laser power and scanning velocity were changed between specific samples to allow for defects. The built specimens were printed using Power-Velocity (PV) map for 30μm layers as a guideline to print within the keyholing region, the processes window, and the lack of fusion (LoF) region. Five laser powers and scanning speeds were selected and randomly assigned to forty-five specimens of the three regions.

1.2 MOTIVATION

The Motivation of this project is to investigate how the as-built surface affects the cyclical life of Ti-6Al-4V when printed at various process parameters. 4-point bending testing was conducted to evaluate this effect and represented to investigate the following objectives+

1.3 OBJECTIVES

I. Manufacture Ti-6Al-4V specimens with different process parameters using Laser Powder bed Fusion.

II. Conduct defect characterization for the printed specimens categorized by process parameter.

III. Develop a procedure to standardize testing and eliminate variability within testing.

IV. Conduct cyclical experiments to assess the cyclical life of the printed specimens.

Chapter 2: Literature Review

2.1 What is Additive Manufacturing?

Additive manufacturing, better known as 3D printing, is a process where the material is selectively added in a layer-by-layer fashion until a desired geometry is made. Early techniques for AM date back to the 1980s where vat photopolymerization (VPP) printing was developed by Chuck W Hull of 3D systems. Since then, AM has broadened its meaning to incorporate various materials such as metals, polymers, and ceramics. In addition, AM has been implemented in various industries, such as the automotive, biomedical, and aerospace industries. Although AM does offer more freedom in manufacturing when compared to other methods, it is crucial to understand that this technology still has limitations that prevent it from becoming a mainstream manufacturing method.

To fully understand the AM process, it is essential to identify relationships between all seven categories of layer-by-layer manufacturing. For example, all AM technologies require a computer-aided design (CAD) file. A CAD file is a digital representation of a 3D object using 3D design software. Popular CAD software such as SolidWorks, Fusion 360, and Creo are some of the many used CAD packages in the industry today to represent designs digitally After products are designed, they are exported in another file format, such as an STL, then moved to slicer software where the CAD file is divided into layers of equal thicknesses and a print strategy is created. Advancements in slicer software have been made to where print strategies and lead times can be automatically generated. However, proprietary slicer software still requires print strategies to be manually generated. Figure 1 and Figure 1 show images of a CAD file taken and designed in Fusion 360, a 3D CAD software, then exported into Cura, a slicer software used for material extrusion printers.

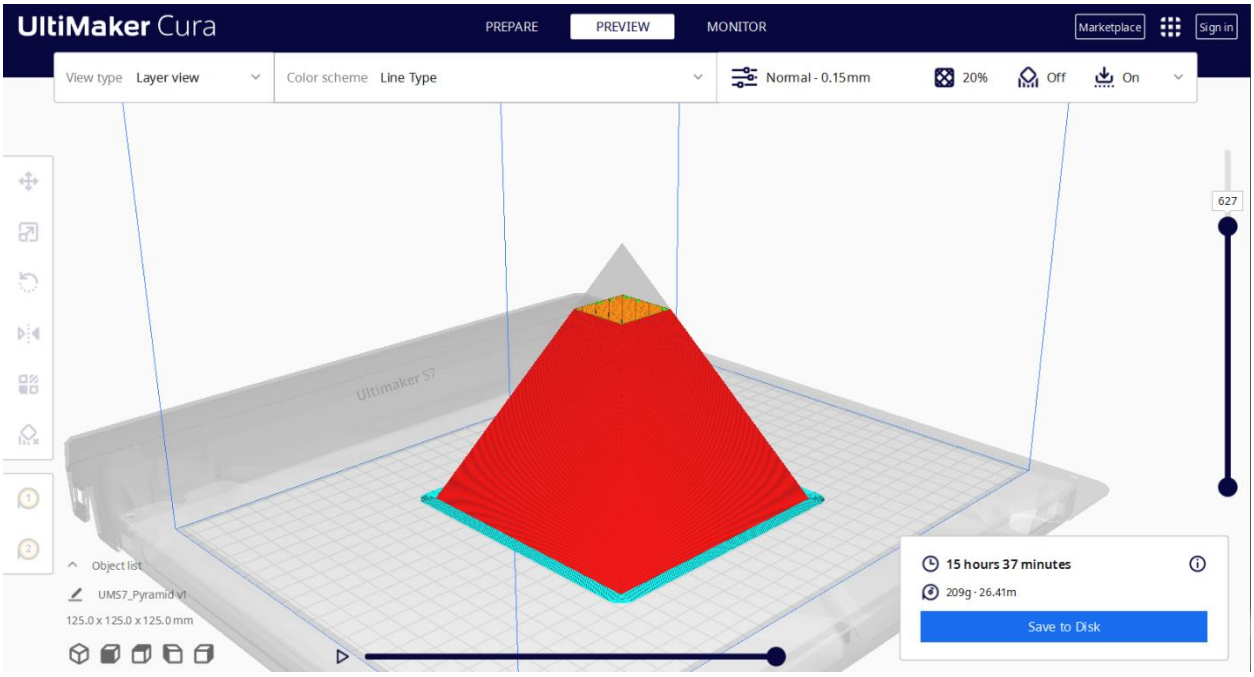

Figure 2. Sliced model of a pyramid using Cura.

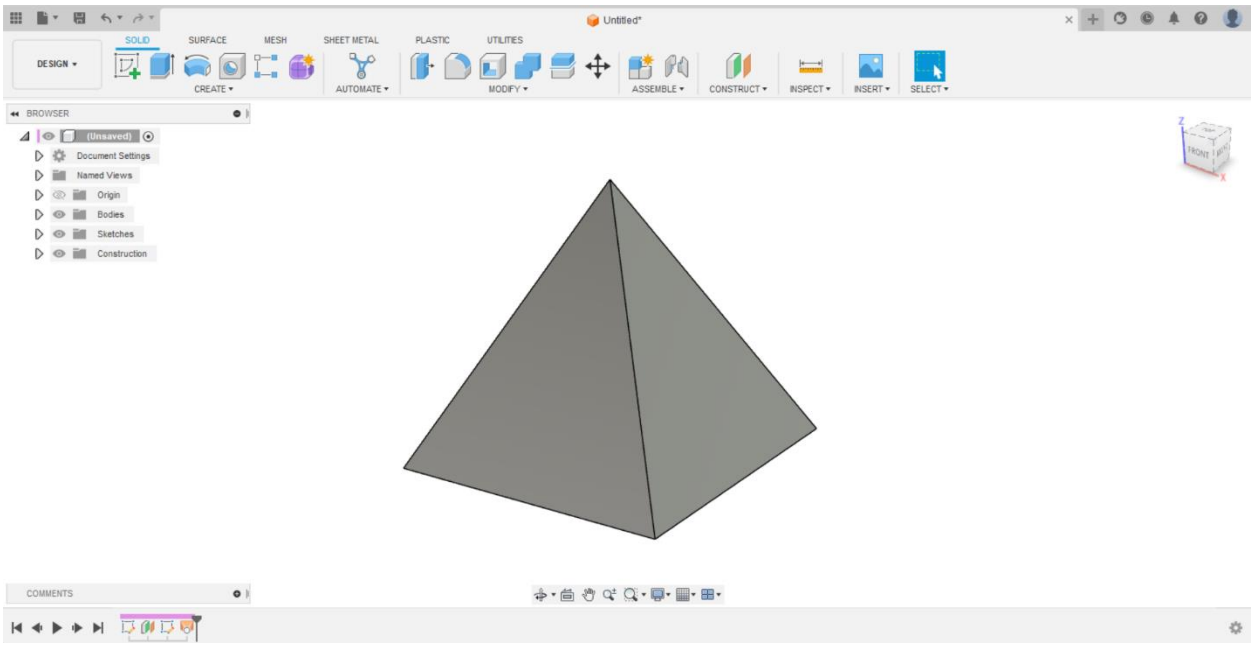

Figure 1. 3D model of a pyramid using the CAD software package Fusion 360

The benefits of using AM are greater design flexibility, less waste, faster lead times, rapid prototyping, and potentially lower-cost manufacturing. For these reasons, AM has begun to

be implemented in various industries. For example, the ability to create custom-made components on a mass production level has been utilized by align technologies, where fourteen million individualized treatment plans by manufacturing corrective orthodontic aligners using vat photopolymerization in their printing process since their founding. In addition, aerospace company Blue Origin has also begun to implement LPBF for their dual-expander cycle engine. The reasons may be because of the high cost of aerospace-grade materials. It may be beneficial to use powder metal for AM than wrought metal through traditional manufacturing methods to reduce waste.

While there are many benefits to additive manufacturing, the limitations of this technology include high equipment costs, expensive maintenance, extensive post-processing, and poor repeatability. For example, metal AM printers can cost upwards of $500,000 for machinery and still require gas purchases to create an inert environment, powdered metal for printing, and labor costs to operate the machine. Furthermore, the maintenance of filters, regular cleaning, and calibration are all factors that must be considered when purchasing a printing system. Extensive post-processing also prevents metal AM from becoming a mainstream form of manufacturing. The post-processing methods performed on AM components are usually heat treatments in addition to surface finishing. High costs are associated with heat treatments because of equipment and power requirements to operate the machinery. Also, AM creates rougher surfaces compared to traditional manufacturing, which can lead to stress concentrations and premature failure when exposed to loads. Therefore, CNC machinery may be required to remove material until the desired surface finish on a component is achieved.

Despite these drawbacks, the future of additive manufacturing shows promise in becoming a more mainstream manufacturing method. By developing more materials and

improving hardware within machinery, it may be possible to manufacture more components with faster lead times, greater dimensional accuracy, and more consistent mechanical properties.

2.2 VAT PHOTOPOLYMERIZATION

Vat photopolymerization (VPP) is a type of 3D printing where a light source is used to solidify a photopolymer to create a 3D component while on an ascending platform. The origins of VPP date back to 1980 by Dr. Hideo Kodama. However, developments have been made today to allow for different scanning strategies that can significantly affect manufacturing time while maintaining a high resolution in the printed parts. It is important to note that VPP printed components' resolution heavily depends on the material selected. In addition, the material properties between resins can drastically vary; therefore, material selection is vital to printing, like all engineering processes.

As described by Ali Bagheri and Jianyong Jin, "The strategy behind the 3D photopolymerization (also known as photocuring or photo-cross-linking) is based on using monomers/oligomers in a liquid state that can be cured/photopolymerized upon exposure to a light source of specific wavelength and form thermosets" [11]. In other words, photopolymers are placed in a vat or tank and then exposed to a luminescent source to create a chemical reaction and harden the liquid into a solid [12]. Typically, the light source can consist of a UV laser, a UV projector to cure the resin, or LED lights [13]–[15]. The mechanical properties of the resins can vary greatly; therefore, material selection is crucial for the intended application. In addition, material selection may also influence the resolution of printing. For example, Formlabs, a famous supplier of VPP printers and photopolymers, advertise their resins for dental applications with a resolution as high as 100μm; On the other hand, the general use clear resin is advertised with a resolution of 25 μm [16], [17].

As for mechanical properties, there are a variety of resins that can be selected depending on the specific application. Standard resins (aesthetic resins) such as clear, black, and grey are the most frequently used for personal use [15]. After post-processing, the resins respond well to tensile loads with a tensile modulus of about 2.2 GPa with an average ultimate tensile strength of 65 MPa. However, the standard resins are very brittle, with an average elongation of 6% and an impact strength of 25 J/m [16], [18], [19]. In contrast to the standard resin's mechanical properties, other photopolymers are designed with increased fracture resistance, impact resistance, and temperature resistance. An example can be seen in the Formlabs Durable and Tough 2000 resins. While both have lower ultimate tensile strengths of 28 MPa and 45 MPa, respectively, their fracture resistance and ductility are higher. Durable resin is designed for applications where the component will be exposed to low-fiction high-cycle environments. Therefore, the durable resin is rated with a fracture toughness of 40 J/m and a total elongation of 48% [20]. *Tough resin* is a structural resin designed for an environment where slight deflection of a component is required. Therefore, its high modulus of elasticity makes it stiffer than durable resin; additionally, it has a fracture resistance of 40 J/m and total elongation of 48% out, performing the standard resins [21].

Stereolithography (SLA) is a form of VPP where a laser is used as the energy source to cure the resin. With the use of galvanometers, the laser can be directed at various locations within the build plate to print layers with very high precision at a constant velocity; however dimensional accuracy of the printer is driven by the laser's spot size [15], [22]. Furthermore, the laser can vary in intensity to increase or decrease the overall layer thickness when printing affecting the overall print time [15], [23], [24]. Compared to the other methods of VPP, SLA can be a more desirable printing process when the model size is considerable, the model design is

geometrically complex, and precision is needed [24]–[26]. The most significant limitation of SLA printing is longer lead times for extensive parts because of the area the laser must travel to [26]. Shown Figure 3 is a general systems for SLA printing from A review of Stereolithography: Processes and Systems by Jigang Huang et al [25].

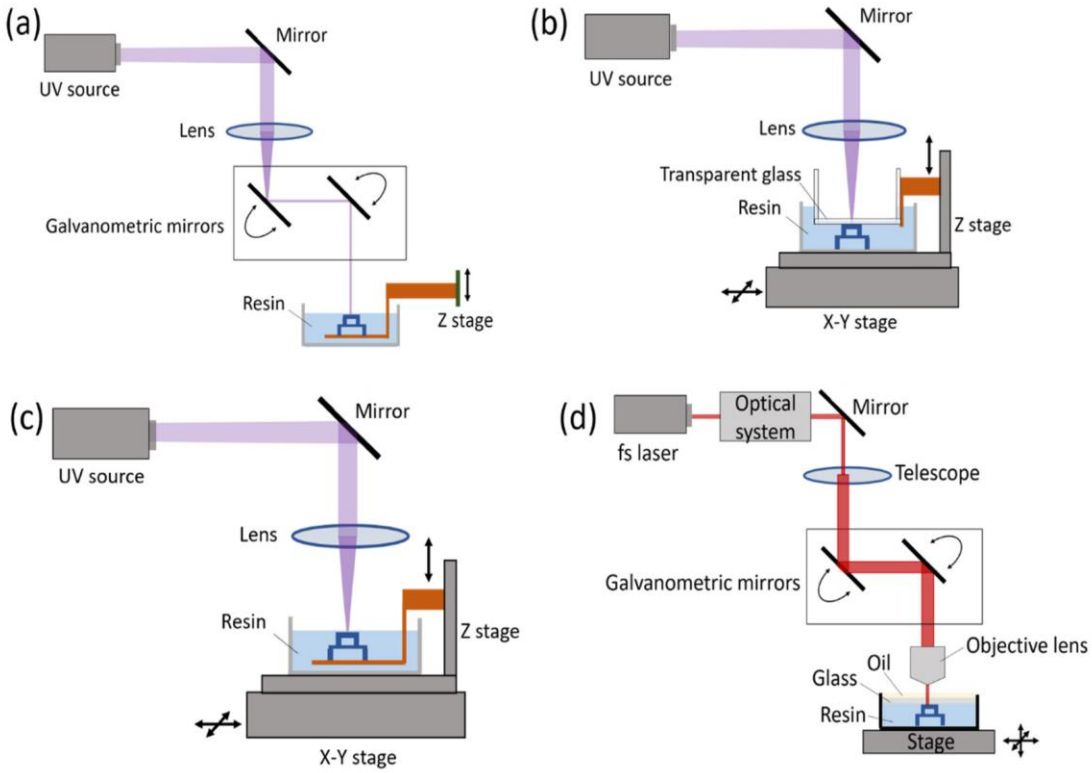

Figure 3 Types of printers used for the SLA printing process [25].

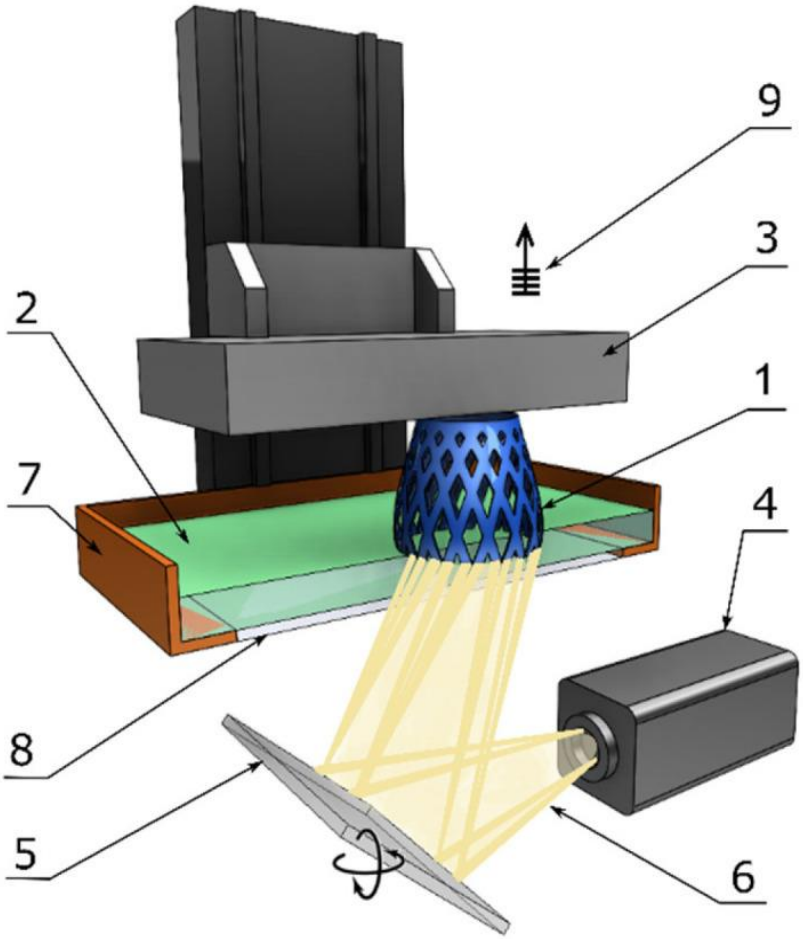

Figure 4 Illustration of the DLP printing process labeled as such. 1—printed part, 2—liquid resin, 3—building platform, 4—light source, 5—digital projector, 6—light beam, 7—resin tank, 8—window, and 9—layer-by-layer elevation [15]

Direct light processing (DLP), or projection SLA, is another popular form of VPP printing. The printing process is remarkably similar to SLA printing; however, the distinct difference of DLP is the projection printing method. Versus using a laser, DLP printers are equipped with a projector that creates an image of a cross-section. As a result, an entire layer can be faster than SLA printing because of the more excellent area coverage with the exact resolution of an SLA printed component. Despite that, to maintain the exact resolution as SLA printers, the DLP printers are in the component size. In other words, DLP is limited to smaller and high-resolution - low-volume components. Figure 4 depicts the DLP printing process from the 2021

review article A Review of Vat Photopolymerization Technology: Materials, Applications, Challenges, and Future Trends of 3D Printing by Marek Pagac et al [15].

Another modern method of VPP created in 2015 is continuous liquid interface printing (CLIP), where the component is always in contact with the liquid resin in the tank allowing for very high-resolution prints at very high printing speeds [27]. As in a 2016 study using the CLIP process for manufacturing as many as 64 microneedles in one print, the process could manufacture all components with features as small as 4.6μm and 1 mm in height in less than 10 minutes [28]. To further elaborate, the rate at which the height of a component is developed can be upwards of 500 mm/hr. The critical element to CLIP is eliminating the presence of oxygen, a destructive element in the curing of photopolymers, by using an oxygen-permeable window to create a dead zone [25], [27]. Vox, a self-described general interest news site for the 21st century, has reported on CLIP in their portrayal of the printing process in Figure 5 [29].

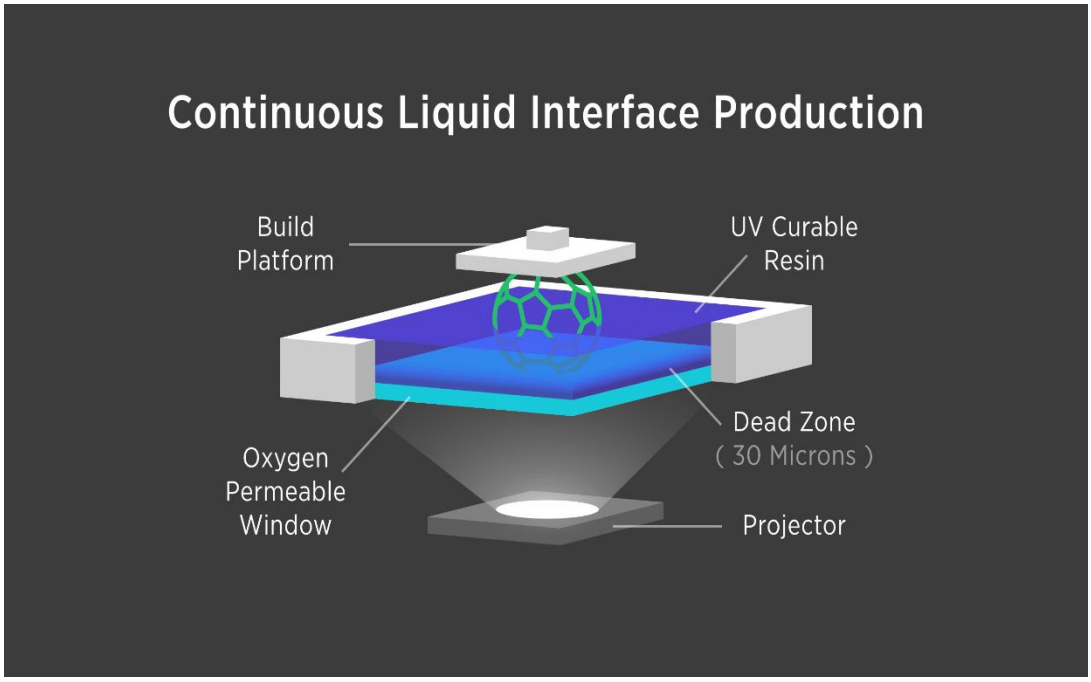

Figure 5 Image depicting the continuous liquid interface production (CLIP) printing process. [29]

In conclusion, VPP is an advanced form of AM that allows various photopolymers to be printed with various mechanical properties. The ability to chemically fuse the material is beneficial when the mechanical performance of a VPP component is evaluated. To further add, the dimensional accuracy of VPP is also highly desirable. However, the drawbacks of VPP are within the relationship between build size and manufacturing time. For DLP and CLIP, as manufacturing speed increases, the maximum build dimensions are further limited to prevent dimensional inaccuracies. As for SLA, larger prints are possible at the expense of significantly increasing manufacturing time. Overall, the research and future development of VPP technologies does look promising to improve the printing of photopolymers further.

2.3 Sheet Lamination

Sheet lamination, often laminated object manufacturing or ultrasonic consolidation, is a form of AM where sheets of specific geometries are bonded together through an energy source [30]. The workflow process and bonding method can vary depending on the material used. However, the central concept remains the same in creating 3D models. The advantages of sheet lamination are seen in its ability to rapidly create prototype parts at a relatively low cost [31]. Despite that, sheet lamination is one of the least accurate methods of AM and creates significantly more waste due during the forming process of the sheets [30], [32]. Nevertheless, manufacturing 3D geometries is innovative and noteworthy as one of the seven forms of AM.

The sheet lamination dates back to the early 1990s when paper sheets were formed using a CO2 laser [33]. Since then, sheet lamination has advanced by enabling the use of more materials, such as plastics and metals. The sheets are typically formed by rolling a sheet of material over the build plate and then having a laser follow a contour of a 2D image to cut the sheet [31], [34], [35].

The build plate is then lowered, and the rollers move the cut sheet aside to allow an uncut layer over the built plate. The process is then repeated numerous times until a 3D geometry is made.

Sheet lamination is applicable for many different materials and allows multi-material printing. The process for using multi-material printing for metals, plastics, and ceramics would be by adding a different material sheet or sheets during the printing process. However, the issue of concern would be the adherence between layers of different materials to prevent any adverse effects on the mechanical properties. Therefore, methods have been thoroughly researched to create robust components. The paper has also been used for single-material manufacturing to create 3D aesthetic models due to their sturdiness at thicknesses around 5 mm - 6 mm [33]. While sheet lamination does offer the fabrication of different materials, it still depends on the application of use.

Adherence methods for materials in the sheet lamination can be categorized into the following categories [33]:

- Thermal bonding
- Sheet metal clamping
- Ultrasonic welding

In addition, the sheet lamination process can be categorized into two distinct workflows, bond-then-form or form-then-bond methods. These two workflows mean the printing process will form a layer and then attach the part to the object. The bond-then-form process first bonds an entire sheet to the printed object or build plate before forming the layer into the desired shape.

Thermal bonding is a common technique used in sheet lamination to adhere subsequent layers to one another. Typically used with paper, a heat-activated adhesive is applied to both sides of a laminated sheet. Then, a heated roller is applied to a new layer to adhere the layer to the preceding layer [33]. Shown in Figure 6 is a schematic of the sheet lamination process with a heated roller created by Zhenzhen Wang and Yan Yang [36]. Here, the heated roller moves along the transversal axis while the laminated sheet is rolled over the 3D-printed model by the two rollers. The galvanometer and laser form the sheet of material into the desired geometry; then, the build plate is lowered to allow the uncut portion of the sheet to be placed in subsequent layers. While this method is very effective for polymers and paper, this approach is unsuitable for metals due to the adverse effects of the mechanical properties. Therefore, a form of ultrasonic

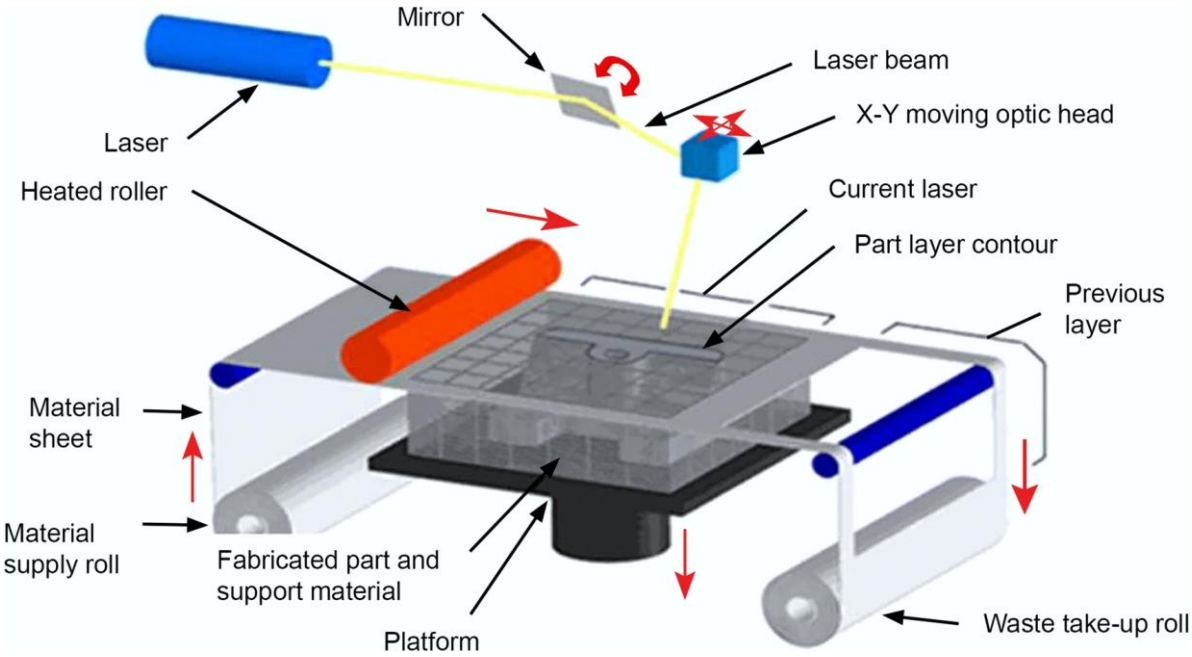

Figure 6 Schematic of the Sheet lamination process with a heated roller. [36]

AM (UAM) was created to adhere metals while maintaining the same level of mechanical performance.

UAM, developed in 2000, is a hybrid form of additive manufacturing by fully bonding metals to retain their mechanical properties [33], [37]. One of the most significant benefits of UAM is the ability to weld materials together at lower temperatures than other forms of metal AM [38]. To join the materials, high-frequency oscillation of a rotating sonotrode is used to bind thin layers of foiled metal to one another, as shown in Figure 7 [37]. Since the metal is being bonded at a temperature lower than their respective melting temperatures, metals with very different properties preventing them from being weldable can be joined [37]. For example, as

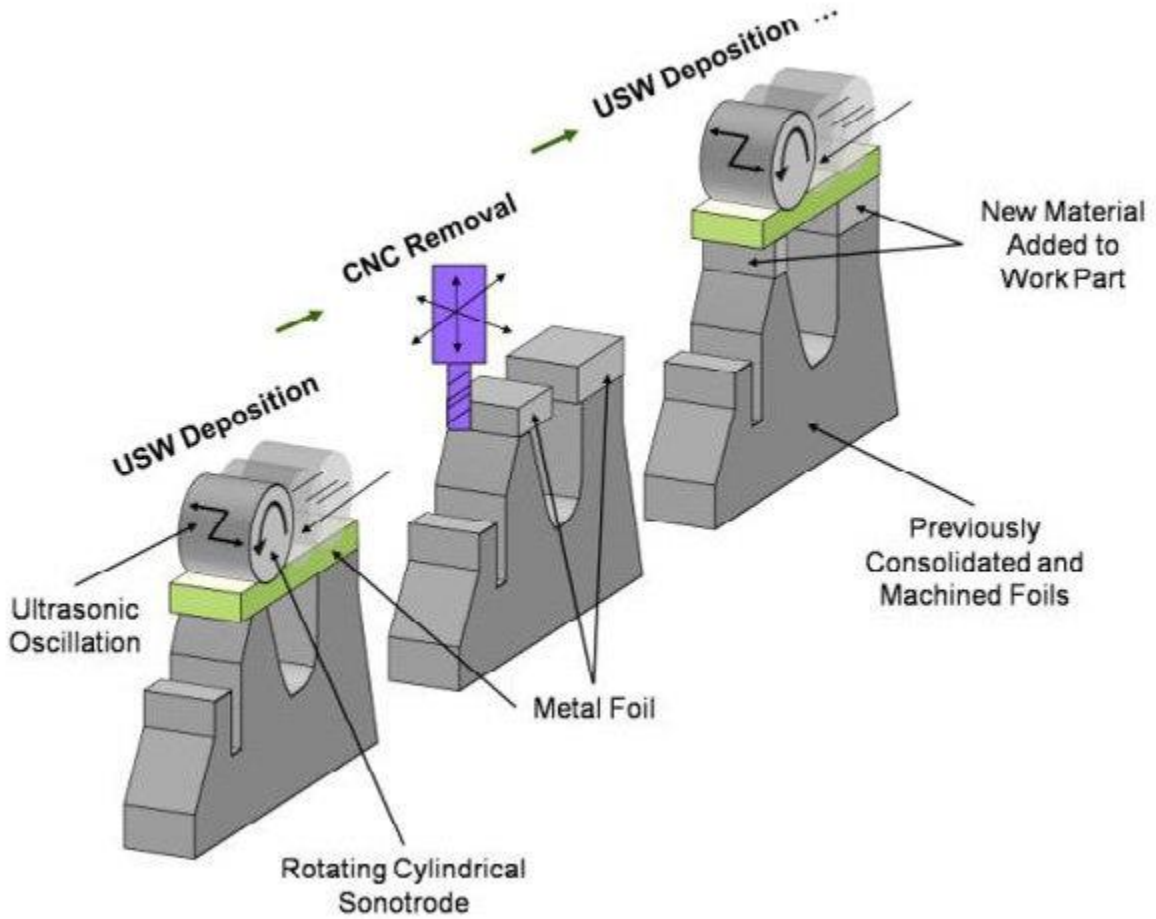

Figure 7 Illustration depicting the UAM bond them form process [37].

shown in , copper is bound to aluminum through sheet lamination, which cannot be achieved through adhesion methods that require metals to be melted to adhere to one another [33].

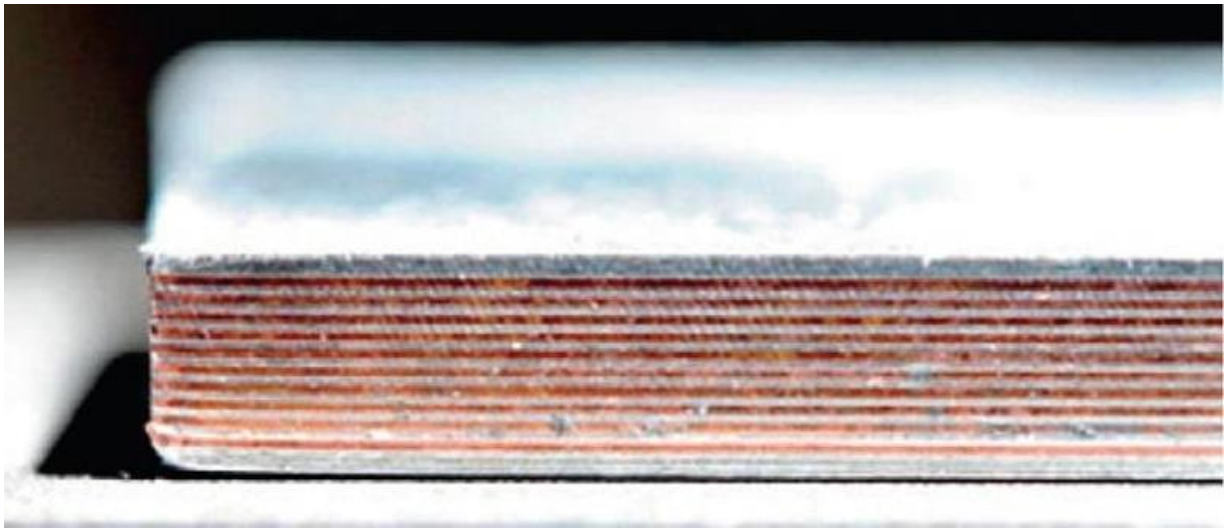

Figure 8 UAM sheet lamination adhering copper and aluminum sheets together. [33]

The applications and research of sheet lamination were seen in the early 1990s; however, this form of AM has yet to evolve into a popular form of manufacturing for commercial use [32]. Although sheet lamination has yet to gain widespread acceptance, companies were founded using sheet lamination in hopes of commercializing this manufacturing method. For example, Michael Molitch-Hou published his works about a company named Mcor Technologies, which aimed to create a 3D sheet lamination color printer by using a tungsten carbide blade to form sheets of paper [35]. However, as of 2023, the company could not compete in AM market, forcing themselves to declare bankruptcy. The reasons for bankruptcy may be because sheet lamination could not compete with other forms of AM. For instance, sheet lamination limits the manufacturer to less complex forms for manufacturing because it is the only process to incorporate subtractive manufacturing. Even though sheet lamination undergoes some post-processing, its layering method can leave components anisotropic. Shown in Figure 9 is an example of a sheet lamination component where the layers of the components are seen [32].

Lastly, the workflow process requires removing material from a manufactured component. This results in parts not being manufacturable because there would be no way to remove excess material from internal channeling. Compared to other AM processes where layer adhesion does not obstruct internal channeling, sheet lamination is unfavorable.

Figure 9 A sheet lamination component was produced and the layers are clearly visible upon completion [32].

In Conclusion, sheet lamination is an innovative form of AM and may be a feasible manufacturing approach depending on the application. While it has been seen that this form of manufacturing could have been more successful commercially, this is the only AM method that can create a bond between two metals with opposed mechanical properties without melting. In addition, this is the only form of AM that can also adhere the paper to 3D models classifying sheet lamination as its unique form of additive manufacturing.

2.4 MATERIAL JETTING

Material Jetting can be compared with the process of an inkjet printer, where tiny droplets of ink are strategically deposited to form an image; however, instead of printing with ink, a light-sensitive liquid photopolymer can be deposited and cured via UV light to create a layer of a 3D component. Repetition of this process material jetting allows the manufacturer to create multi-colored components applicable to various applications. For example, it has been seen that material jetting can be used for medical, mechanical, acoustic, electronic, and aviation applications [39]. Material jetting was first introduced to the AM market in 2000 by Objet Geometrics Ltd., but in 2012 Stratasys purchased the company and rebranded the material jetting technology [40]. Since then, there have been other manufacturers in the material jetting market, such as Mimaki, XJet, Solidscape, DragonFly, XYZPrinting, and 3D Systems.

While the workflow process for a material jetting printer may vary, the overall printing process is as follows [40], [41]:

1. The machine is prepared, loaded with the needed material, and the 3D CAD file is input into the printer.
2. Photopolymer liquid and support material is strategically deposited onto the build platform through some form of actuation. Using UV light, the newly deposited photopolymer is cured. The build plate is lowered, and the process is repeated on subsequent layers until the 3D component is fully manufactured. A schematic of the printing process can be seen in Figure 10 [42].
3. The component is removed from the build plate and post-processing methods such as water jetting are conducted for support material removal.

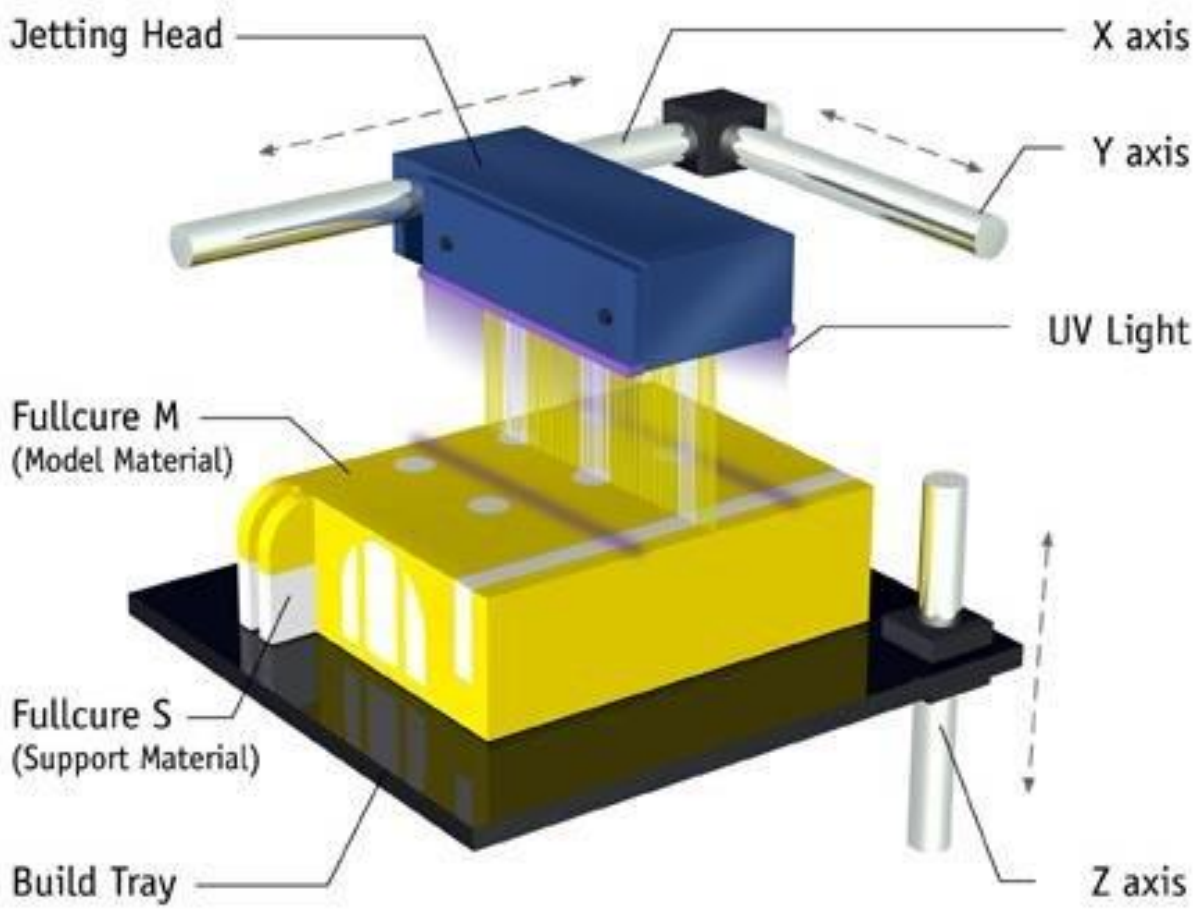

Figure 10. Schematic of the main components in a material jetting printer. [42]

Commercial materials used for material jetting are very limited to soluble waxes for support material and photopolymers. However, research materials have been expanded to ceramics and metals [43]. In the case of ceramics, the photopolymer acts as a binding agent to bond slurries of ceramic powder to form a shape. This can be seen in the works of E. Willems et al., where the process of printing zirconia ceramics through material jetting and mechanical properties were analyzed [44]. According to the works, it is said that through material jetting alone does not create a functional part because of the lack of structural integrity within a green part. The weak adherence can be reported in the density of the green part of printed components. Therefore, sintering is required to fuse the ceramic particles to increase the specimen's density and

mechanical performance at the expense of dimensional accuracy. As for metals, the research for applications of metal AM through material jetting is less abundant than other methods, such as laser powder bed fusion or directed energy deposition printing. The main limitation is that material jetting needs the energy to fuse metal particles with high melting temperatures. However, solder can be used for material jetting machines for electronic applications. As reported through various works, densities as high as 99% have been achieved through material jetting metal. However, due to the heat involved during manufacturing, printing components are susceptible to damage [43].

One of the most complex aspects of material jetting is the deposition method of the material. Figure 11 illustrates a chart categorizing all the actuation methods currently available to deposit material [45]. In a broad overview, material jetting can be classified into two main categories: continuous deposition and drop-on-demand deposition. A continuous deposition allows the material to be deposited with a constant stream of droplets ejected continuously using an electric field to deposit the material in specific areas [46]. On the other hand, drop-on-demand deposition uses actuators with different actuation methods to deposit droplets [43], [45].

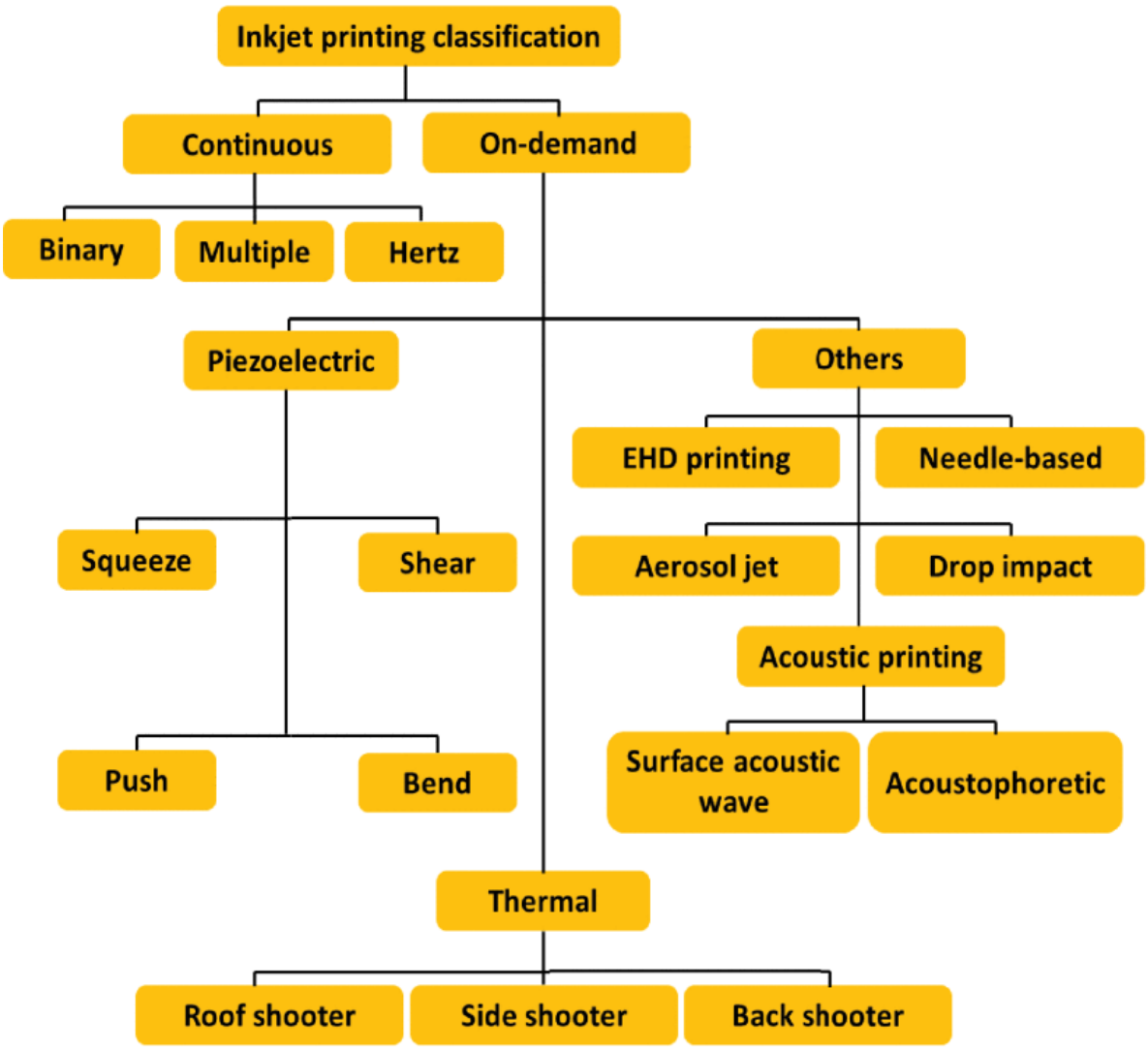

Figure 11 Tree diagram illustrating the types of droplet mechanisms in material jetting [45].

Piezoelectric actuators in material jetting are some of the most researched methods for drop-on-demand printing and are favored for their reliability [43], [45], [47], [48]. he principle of these actuators is taking advantage of the physical deformations that occur when an electrical load is applied [49]. In Figure 12 the images represent the methods by which a piezoelectric can form droplets of the photopolymer material [45]. While there are multiple methods for actuation, it is essential to note that all methods use the piezoelectric to alter the pressure of the pressure chamber to form droplets [47]. The advantage of this process is that the deposition process can print at speeds as high as 500 mm/s In addition, using piezoelectric actuators eliminates the need

for complex circuitry, such as those used in forms of continuous deposition printing where specialized software and hardware are required to ensure droplet formation of material is consistent throughout the printing process [48]. However, the disadvantages of piezoelectric actuation are the pressure oscillations undergone after the initial voltage is applied and the susceptibility to clogging due to small orifice sizes. Various wave methods of applying an electrical load have been created to counter the pressure oscillations from the actuator to mitigate the effects. To further elaborate, by altering the polarity of the voltage or the dwell time of which a voltage magnitude is applied, it is possible to make the effects of pressure oscillations negligible [45].

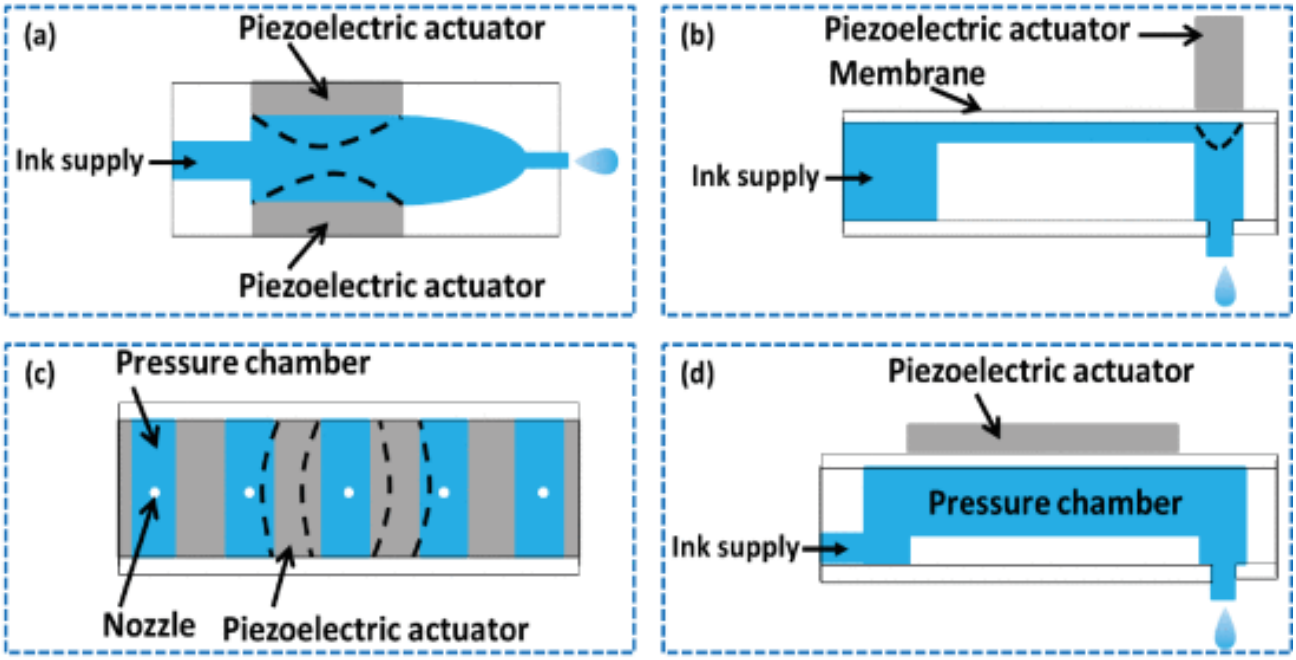

Figure 12 Types of piezoelectric actuation methods. (a) squeeze mode, (b) push mode, (c) shear mode, (d) bend mode [45].

Thermal actuation is another method of material jetting actuation used to dispense droplets. Relying on the vaporization of the material through a heating element, a vapor bubble forms inducing pressure on the liquid [50]. The pressure from the vapor bubble then forces a droplet out, collapsing in on itself, creating a suction force that creates a cycle allowing more material droplets to be dispensed. While this technology does work in terms of reliability, the

heating element is prone to failure because of electromigration [45]. Figure 13 is an illustration of the type of thermal inkjet printheads [45].

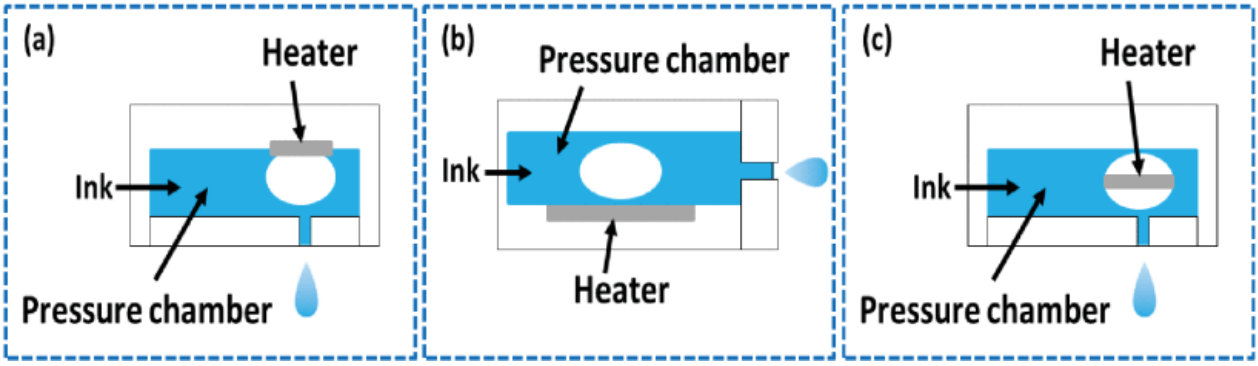

Figure 13 Illustration of a thermal printhead with the heater located at various locations within the material jetting process [45].

Continuous deposition printing is the final, most frequently used deposition type in material jetting. The continuous deposition is favorable compared to another drop–on–demand methods because it generates droplets at a rate as fast as 60 kHz [51]. Unlike drop-on-demand, where the printer's droplet of material is formed by an actuator forcing the material out of the nozzle, continuous deposition constantly expels material, forming droplets through the Rayleigh instability phenomenon [51]. The liquid material in a continuous deposition is constantly pressurized, forcing the liquid to exit a small orifice uniformly. To control the location at which the droplets are dispensed, a charging field is located near the exit of the nozzle to charge the material electrostatically [43]. Charging the liquid using deflector plates, the material can be guided onto the building platform or placed into a reservoir for later use. Material reusability is commonly used for regular printer applications; however, in terms of R&D or industries where material purity is of profound concern, continuous deposition methods can be seen as very wasteful due to the inability to recycle material due to the risk of contaminates [51]. Figure 14 & Figure 15 show the primary components used for continuous deposition printers and a droplet

comparison between continuous deposition and drop-on-demand deposition, respectively [43], [51].

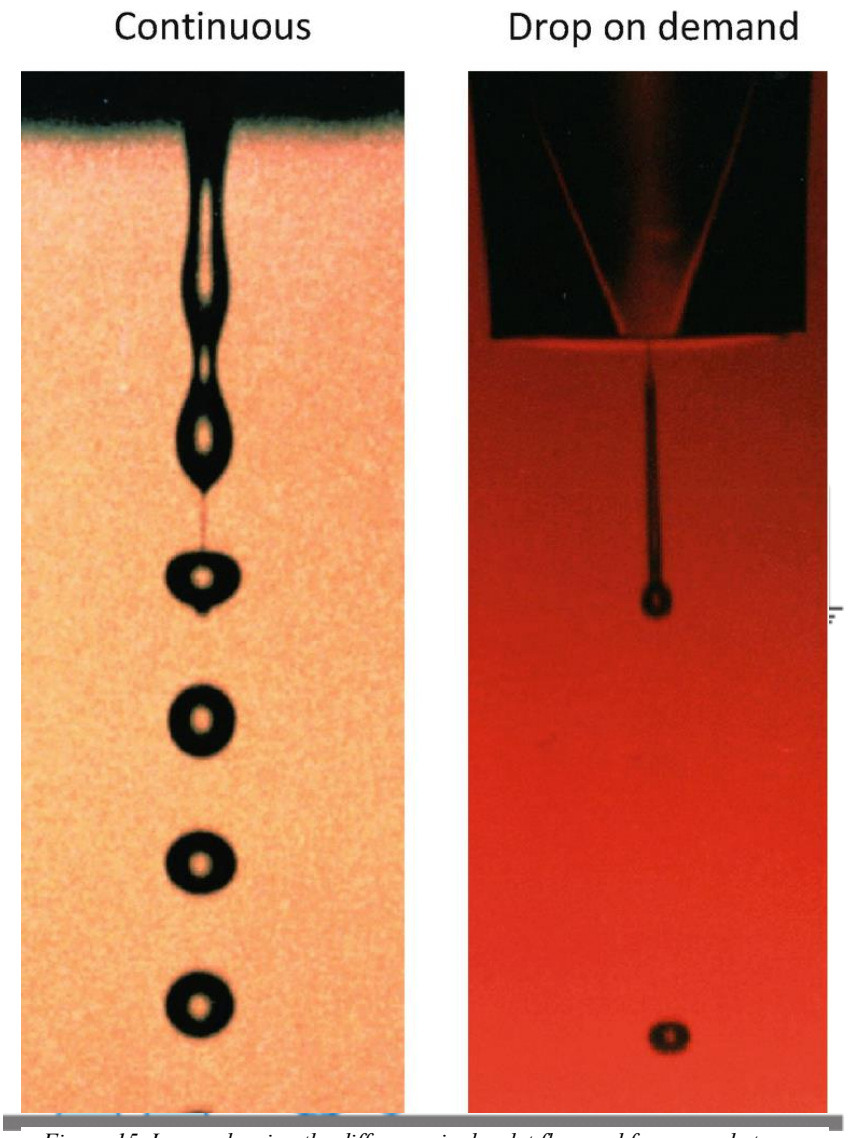

Figure 15. Image showing the difference in droplet flow and frequency between continuous and drop-on-demand deposition [51]

While the process does not apply to metals or ceramics, material jetting is a viable option for printing multi-color polymers. It is shown that the process for printing, while similar to VPP

printing, is unique and complex to manufacture 3D components. Material deposition and droplet formation are by far the most extensively studied characteristics in material jetting. Three distinct actuation methods were shown to give more insight into the process of material jetting by investigating piezoelectric actuators, thermal actuators, and continuous deposition printing. While future research is still required, material jetting remains a unique form of AM that will revolutionize the manufacturing of photopolymers.

2.5 Material Extrusion

Material extrusion, the process of extruding material through a small orifice, is one of the most common forms of AM to date. Offering a wide range of materials and the ability to produce 3D components rapidly at a very affordable cost makes material extrusion an ideal choice for 3D printing. Scott Crump, the founder of the 3D print company Stratasys, acquired a patent for fused deposition mode (FDM) printing [52]. In addition to printing polymers, material extrusion methods are applicable for biomedical uses in gel formation and melt extrusion printing [53], [54]. Current research within the last five years aims to investigate the behavior of newer composite materials, metal-polymer, wood-polymer, and carbon fiber-polymer composite materials [55]–[57]. A schematic of a polymer material extrusion printer can be shown below in Figure 16 where the workflow process can be described as the following [58]:

1. After designing and slicing the file, load the printer with the respective material (filament, cartridge, or pellets).
2. Preheat the extruder to allow for material to liquefy before extruding.
3. Allow printer to deposit material on the build plate and regularly clean nozzle during the printing process.
4. After printing and cooling, remove the printed component from the build plate.

5. If necessary, follow post-processing procedures to remove support material, to achieve the desired surface finish, or to enhance the mechanical properties.

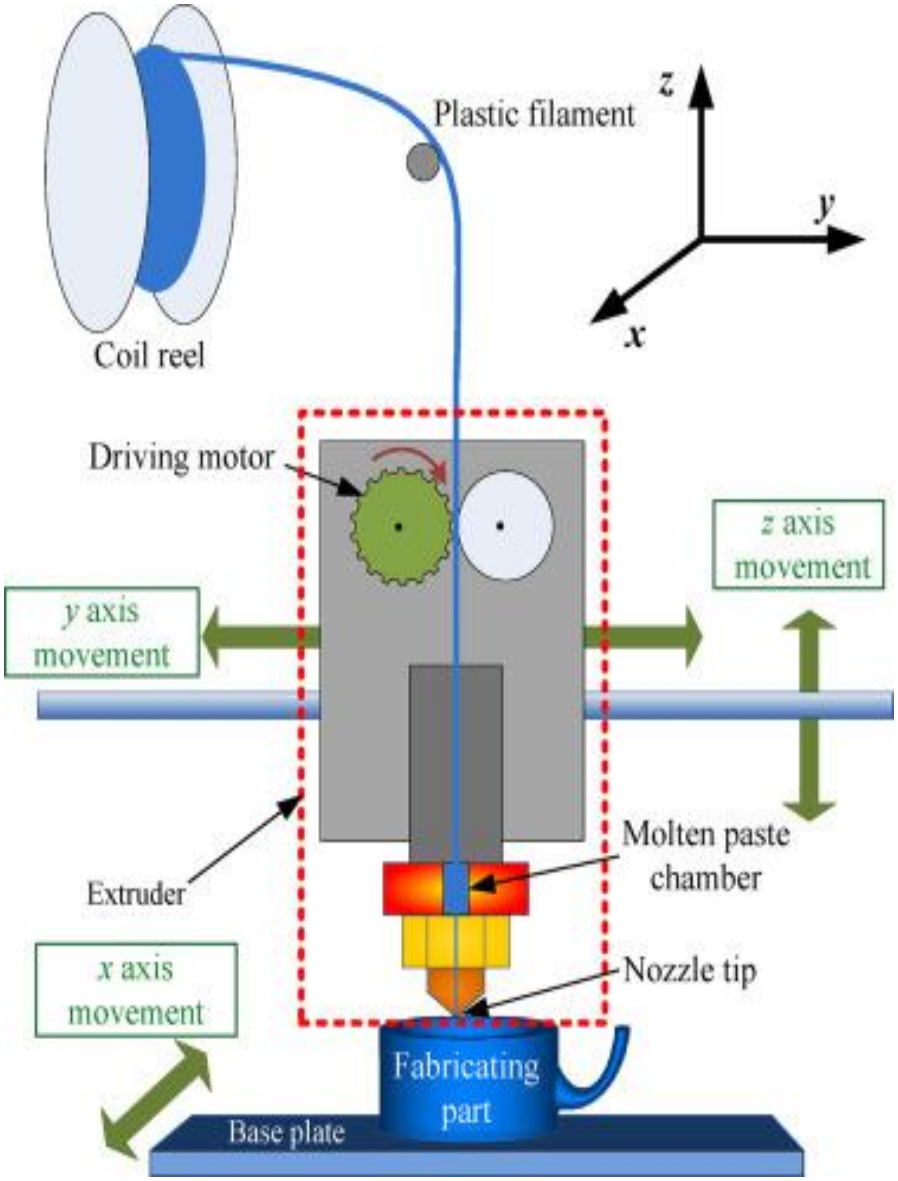

Figure 16 Schematic of filament based material extrusion printer [58].

There are multiple advantages to manufacturing through material extrusion, especially in lead time, cost-effectiveness, scalability, and accessibility. The most significant advantage of material extrusion is that it is one of the most cost-effective forms of additive manufacturing,

with printing systems costing as low as $200 [59]. While this may be the cost for desktop printers marketed for the hobbyist or small business demographic, industrial material extrusion printers exist for large-scale operations, allowing large quantity production and multiple unique components to be built into one print with higher resolution. In terms of waste, material extrusion is one of the AM methods that can produce components without any material waste because it only deposits material where needed making it a favorable manufacturing method.

While there are undoubtedly many benefits to using material extrusion, depending on the application can certainly be a limiting factor. For instance, material extrusion is limited in material compatibility; this method is not typically desirable for manufacturing metals and ceramics. While in ceramics, it is seen that parts can be printed with mechanical properties that are similar to already commercially available ceramics, repeatability of manufacturing is an issue. As seen in the works of Frank Clemens et al., it is possible to manufacture ceramics through material extrusion. However, post-processing methods affect the overall dimensions of the component [60]. As for metals, parts production is also in the post-processing portion of manufacturing. Antonio Cañadilla et al. characterized copper manufactured via material extrusion, and his works found porosity in values upwards of 15% after sintering which can negatively affect the mechanical behavior of any material [61].

The last major disadvantage in material extrusion is that the orientation of a component heavily affects the mechanical behavior because printed components are anisotropic. Anisotropy refers to the physical behavior of a material when a load is applied in various directions and must be considered when material extrusion is used as the manufacturing method of choice. In material extrusion, the layer-by-layer deposition of material results in different stiffness and strength values, where the build direction is typically seen as the weakest under tensile

conditions [62]. Through literature, it has been seen mechanical properties of additively manufactured components have been assessed at various printing orientations in order to fully understand a material's mechanical properties [56], [57]. Despite the anisotropic behavior of parts manufactured through material extrusion, the benefits outweigh the limitations, making it a viable option when manufacturing.

The printhead is the most vital component in material extrusion because it determines a printed component's dimensional accuracy, lead time, and quality. Even though various types of extruders exist, they all function on the same principle of liquefying a material and extruding it through an orifice. In Figure 17, three different types of extruders illustrate the methods used for extruding filament [63]. The material loading for plunger-based extruders are cartridges that can be inserted into the heating element before building. The uses of plunger mechanisms are for polymer composite material for ceramics and metals because the high pressure in the nozzle allows for extrusion at low temperatures [63], [64]. Filament-based modeling is the most common form of extrusion for desktop printers, using drive gears to feed filament through a heater to liquefy and extrude material [52]. The materials used for filament-based extruders are polymers such as ABS and PLA [65]. Screw-based extrusion is found in large industrial printers that require high-volume output. An example of a screw-based extruder is the pellet-fed Big Area Additive Manufacturing (BAAM) printer that allows for multiple materials such as ABS, PPS, PC, and PLA-based materials mixed with carbon fiber or glass to extrude up to 80 lbs of material per hour [66].

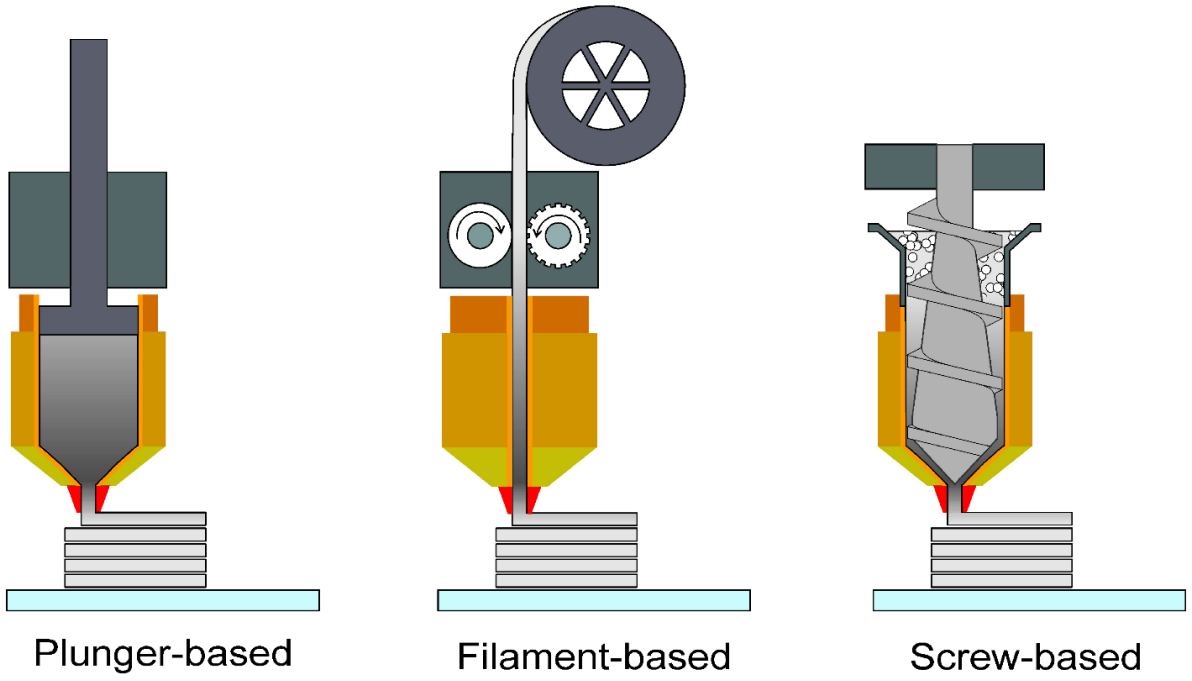

Figure 17 Types of extrusion methods used for filament through material extrusion [63].

Manufacturing through material extrusion is relatively the same regardless of extruder type. However, there are a variety of methods to traverse across the XYZ axis when printing; For example, the Ender 3 by Creality utilizes an open gantry system powered by stepper motors where the extruder assembly travels in the Z and X directions while the build plate travels in the Y direction [67]. On the other hand, the Stratasys uPrint uses belts and stepper motors to move the extruder assembly along the X and Y directions making the build plate move in the Z direction.

Layer height and resolution are critical for the material extrusion process because they influence the final component's mechanical properties and surface finish. Layer height is the thickness of each layer and heavily affects the outcome of the final print and the speed at which a component is printed. For the average desktop printer, layer height can vary between 50-300 microns depending on the diameter of the nozzle. Slicer software can quickly generate tool paths for varying layer heights; however, when designing, engineers must be wary of the detail lost

when printing. Although thicker layer heights print faster and have a higher material flow rate than smaller layer heights, a significant amount of detail is lost when printing with thicker layer heights. Shown in Figure 18 shows an illustration showing a tracing on the original cad model vs. the tessellated sliced file and the printed component [68].

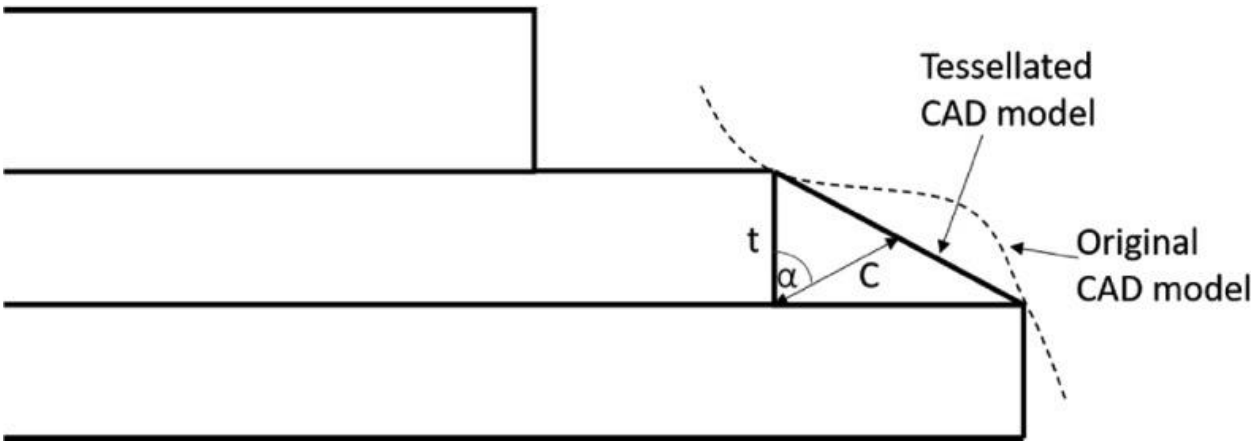

Figure 18 Layer height, t, is compared with a CAD model and its sliced tool path. C represents the distance between the actual print and the sliced toolpath where the angle is defined by alpha is the angle between the two [68].

The resolution of a material extrusion printer is the minimum feature that can be printed. This parameter is heavily dependent on the diameter of the nozzle. Smaller nozzle diameters allow for more intricate designs with finisher surface finishes while increasing the manufacturing time. In addition, smaller nozzles are more susceptible to clogging and inconsistent extrusion [69]. The mechanical properties also vary between different nozzle diameters, as seen through various studies where the material's tensile strength and impact hardness were different as nozzle diameter changed [70], [71].

The future of material extrusion is promising as there are continuous evolution and developments to shape further and mature this form of additive manufacturing. Current works aim to optimize mechanical performance while minimizing mass—for instance, Md. Qamar Tanveer et al. investigated the effects of variable infill densities on the tensile strength of

samples [72]. Other than optimizing mechanical properties, improvements in scalability are also being investigated in BAAM. BAAM is favorable due to its ability to create substantial components with very little manufacturing time, and increasing layer adhesion has been investigated within the last six years. Vidya Kishore et al. publish findings stating that mechanical properties can be significantly enhanced by preheating layers using an infrared lamp [73].

In conclusion, material extrusion is a versatile, low-cost, low-waste, and widely accessible manufacturing method. From polymers to specialized materials, material extrusion is applicable in many scenarios. As mentioned, there are many advantages to this manufacturing method, but there are still drawbacks associated with material extrusion. It will become a more mainstream manufacturing method with future developing and maturing material extrusion technologies.

2.6 Binder Jetting

Binder jetting is a unique form of powder AM that does not use a light or heat source to adhere material together, allowing parts to be manufactured at room temperature and eliminating potential part distortion or residual stresses in a component. Buster jetting printers can strategically deposit droplets over compacted powder using a binding agent to create a material layer. Repeating this process over a new layer of powder continues until a 3D object is manufactured. Much like all AM processes, binder jetting still allows for the personalization of components at a very high degree of precision; however, this can still be accomplished without using support material.

1990 the Massachusetts Institute of Technology created the first successful binder jetting printer [74], [75]. Since then, binder jetting has been adopted in various industries, such as

aerospace, automotive, and medical. Binder jetting AM has also been used to manufacture various components from various materials, such as metals, polymers, and ceramics. While binder jetting is a revolutionary form of additive manufacturing, apparent challenges must be investigated to optimize this manufacturing method further.

Manufacturing through binder jetting is a pervasive process that involves many components, unlike the simpler forms of AM, such as material extrusion. The main components in any binder jetting system are the build platform, powder spreading system, and the binder deposition system. The method for powder distribution can consist of a hopper that deposits powdered material onto the build plate or a powder supply platform that is gradually raised during printing. A roller or recoated evenly distributes and compacts the powder onto the build plate. Two general schematics of binder jetting systems are shown in Figure 19 and Figure 20 [76], [77].

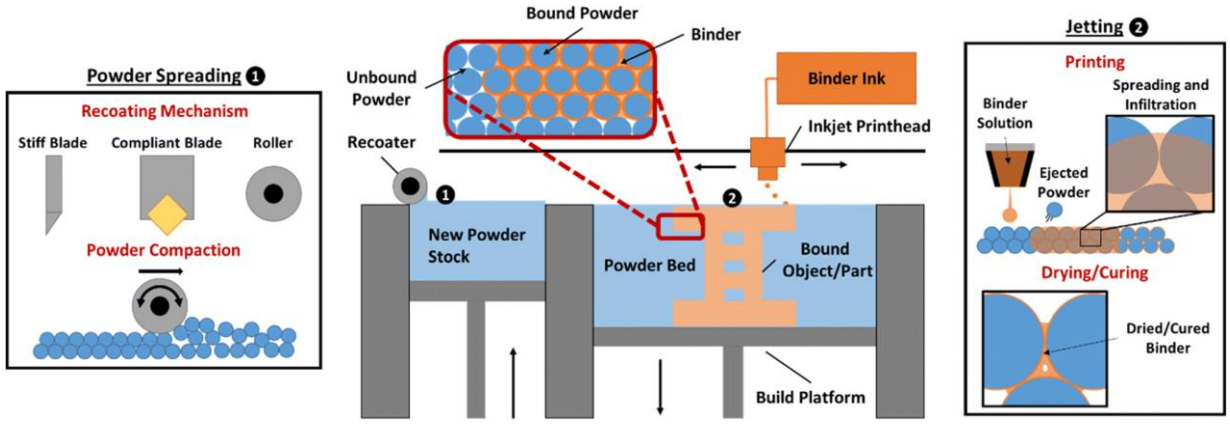

Figure 19 Binder jetting system using a recoater and powder platform to distribute material [76].

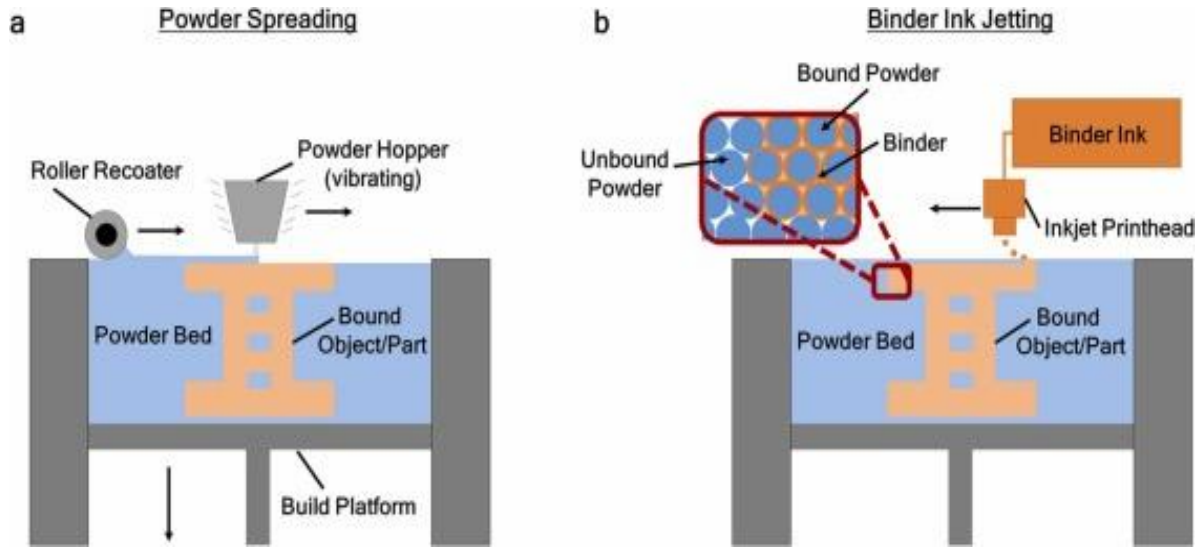

Figure 20 Binder jetting system with a powder hopper and roller recoater[77]

Figure 19 and Figure 20 do an excellent job of the process in which binder jetting occurs. As seen the typical workflow can be described as follows:

1. The powder bed is filled with the desired printing material evenly across the entire build plate.
2. The printhead is primed and inspected to ensure the binder nozzles are not clogged.
3. Binder is deposited on the build plate as a cross section on the 3D component.
4. After depositing the binder, the build plate is lowered, and new powder is deposited and packed over the build plate to ensure the layer is even.
5. Steps 3 and 4 are repeated until the entire 3D shape is printed.
6. After printing the component is allowed some time to cure to harden the part before the exbeing moved into a furnace to fully cure the component.
7. Once cured, the excess powder can be removed from the component revealing the entire green part.
8. The component can be subjected to post-processing methods such as sintering or infiltration depending on the desired application of the material.

The advantages of binder jetting over other AM methods are seen in its versatility in material selection, scalability for large volume applications, ability to print without a heating element, and ability to manufacture complex components without the need for support material. These advantages make binder jetting applicable to many industries and have been seen in companies such as Volkswagen, Cummins Inc., and General Electric.

Other methods of AM are very limited in their material selection; for example, VPP and material jetting are limited to specific photopolymers and material extrusion is limited to polymers. Although there is literature that investigates composite materials being printed through these three forms of AM, the material selection is often a composite material of a base and ceramic or metal [78]–[80]. In contrast, binder jetting allows for components to be printed without the need for a base material and composite material mixture. In other words, metals, polymers, and ceramics can all be printed via binder jetting [81], [82]. This flexibility in material selection allows for component manufacturing for many applications.

Binder jetting may be a favorable option for significant components or high-volume manufacturing for AM. Metal AM and VPP often use a laser to draw the entirety of a cross-section of a component. Using only a single laser significantly increases manufacturing time because parameter changes can greatly affect the final part outcome; therefore, using a laser with a fixed speed will take longer than binder jetting because contours and infill must be printed with a single laser. Binder jetting multiple nozzles in a single pass makes it possible to rapidly create a component cross-section at a faster lead time than other AM applications [83].

Metal AM often uses a high-energy system such as a laser, electron beam, or welding system to adhere to metal. This poses a significant challenge because the need for intense energy can create residual stresses or deformations in part geometry if process parameters are

incorrectly developed [84]. The binders used in binder jetting can rapidly adhere to metal to create a 3D geometry without using any heating element. While it is important to note that the bond created between binder jetting and any other form of AM is significantly weaker, binder jetting can still create green parts with some mechanical strength [85].

The last significant advantage of binder jetting is the ability to manufacture components without supporting structures on components' overhangs. For example, some AM processes require many support structures for components because structures fail to support themselves during the printing process. This leads to additional post-processing that may be needed to remove support material and remove defect marks where the support material attaches to the component. As stated in the works of Wenchao Du et al., there is no need for support material during the printing process because the powder surrounding the material can support overhangs [81]. Another benefit is that components do not need to be attached to the build plate to begin manufacturing, unlike all other forms of AM.

While there are clear advantages to binder jetting, there are disadvantages to this process that must be considered when designing for binder jetting. Some of the most notable disadvantages of binder jetting are the extensive post-processing needed after printing or surface finish and the dimensional accuracy of fully sintered parts. As advancements are made in binder jetting, these issues will be addressed; however, these are the most concerning drawbacks of binder jetting.

While the binder does an excellent job creating a green part, the powder used to create the component is not fully bonded. To address this issue, specialized furnaces and depowering equipment are needed to effectively post-process components without damage. This, however, comes with the expense of having to purchase the equipment and operate it for many hours in a

single use. Furthermore, the lack of bonding in green parts is notorious for being very porous. For general applications, a successful green part is considered to have densities more significant than 50%, dramatically reducing mechanical properties [86].

Consequently, this is the main reason sintering is vital to the binder jetting manufacturing process. Moreover, the challenge of green parts is that the varying densities within green parts also affect shrinkage during the sintering process. As the literature shows, sintering can lead to nonuniform shrinkage while sintering[87].

After sintering, rough surfaces and uneven shrinkage within the sintered component can be possible. Shahrooz S. Borujeni et al. investigated part deformations through sintering shown in Figure 21 [88]. It is evident from the figure that the sintering process significantly affects the outcome of the final part, so current literature heavily focuses on computational models to compensate for these changes in dimension [89]. Also, the literature investigates the effects of ramp rates in temperature and dwell times to mitigate uneven shrinkages in components [90]. Nevertheless, the accommodations that must be made for the sintering process do significantly add to the lead time of components and provide an extra expense to purchase simulation software for the sintering process.

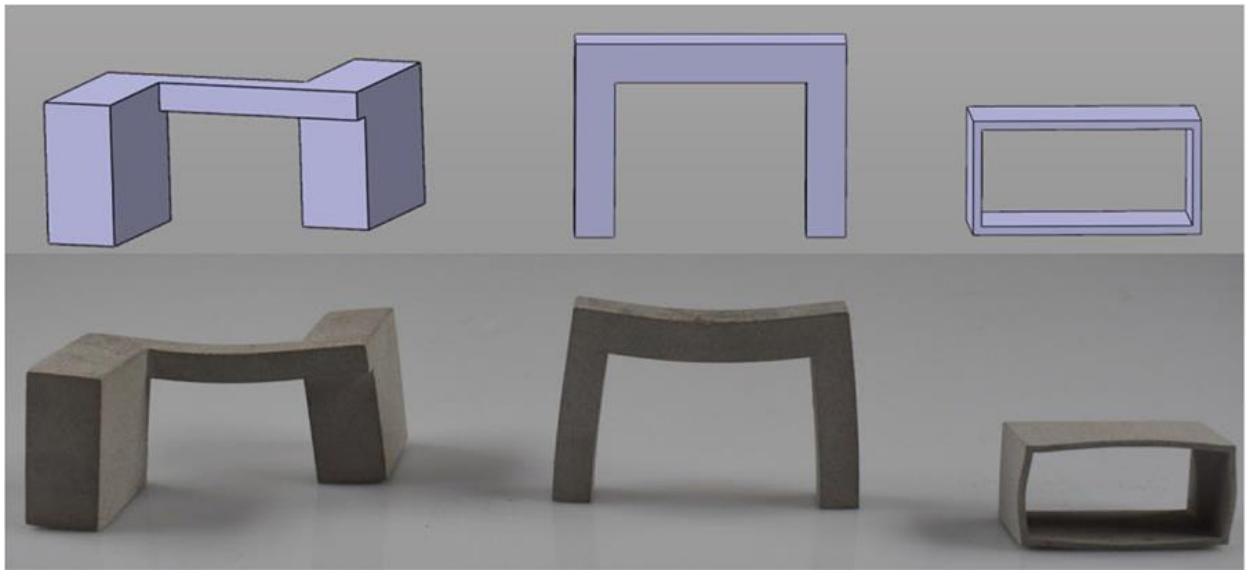

Figure 21 Comparison between the CAD file and sintered components manufactured through binder jetting [88].

As seen, binder jetting is a revolutionary form of AM, but it has its limitations. Future developments are expected to further evolve this manufacturing method in various areas, such as enhancing mechanical properties through printing and post-processing, developing sintering profiles for defect mitigation, and expanding its already vast material compatibility. Although much research must be conducted for binder jetting, it continues to be a mature manufacturing method.

Printing and post-processing optimization has been investigated in Hadi Miyanaji et al. and Marco Mariani et al.'s recent works. In the works of Miyanaji, the effect of particle size was evaluated on the overall quality of binder jetted parts, and it was found that finer powder sizes lead to increases in density and the ultimate tensile strength of the component [91]. At the same time, Mariani investigated how powder morphology affects the mechanical properties and microstructure of the refractory metal, Tungsten carbide-cobalt [92]. The applications to enhance the material properties of components manufactured through binder jetting will make its manufacturing method with traditional manufacturing for mechanical applications.

Overall, binder jetting is a unique form of manufacturing that adheres to material without any heating unit. Though it has many benefits, such as supportless printing, vast scalability, and compatibility with a wide range of materials, it still needs to be improved. The need for extensive and highly complex post-processing increases lead time, cost, and manufacturing risk but still poses a significant challenge for binder jetting today and must be further developed to mature this manufacturing method. Nevertheless, this technology is evolving rapidly with plentiful research to increase the effectiveness of binder jetting.

2.7 Directed Energy Deposition

Directed Energy Deposition (DED) is a large-scale AM process unique in its manufacturing method. Like material extrusion, DED uses a build plate, a printhead to manufacture components, and thermal energy to adhere material together; however, the printhead can consist of a higher energy system such as an electron beam, laser, or arc-welding system. In addition, the feedstock is also significantly different from the feedstock of material extrusion by being either wire or powdered metal. Because of the specific feedstock requirements, DED is one of the most expensive forms of AM. However, it is still applicable in many industries for its ability to create the most prominent components compared to the other AM methods.

DED needed to develop significant components that may have been costly to manufacture through other forms of manufacturing while still maintaining quality. For example, the desire to manufacture refractory alloys was of very high interest in the late 20th century. To investigate this idea, the first wire and laser DED systems were developed in the 1990s, but laser DED was not entirely constructed until 1997 by Sandia National Laboratories [93]. Sandia laboratories first began investigating laser DED through what is now known as laser-engineered

net shaping (LENS). Also, it was not until 2007 that NASA contributed another significant development to DED by creating DED AM through electron beam printing [93].

Material deposition and build can vary depending on the DED system; for example, DED systems using powdered feedstock are equipped with a nozzle that ejects the powder using an inert gas as a propellant. On the other hand, wire feedstock DED systems are driven using a wire feeding mechanism [94]. While both methods differ, they are similar in that they all require a shielding gas to prevent unwanted reactions with the atmosphere when printing. Shown in Figure 22 and are illustrations of methods of feedstock distribution according to their respective form of printing [95].

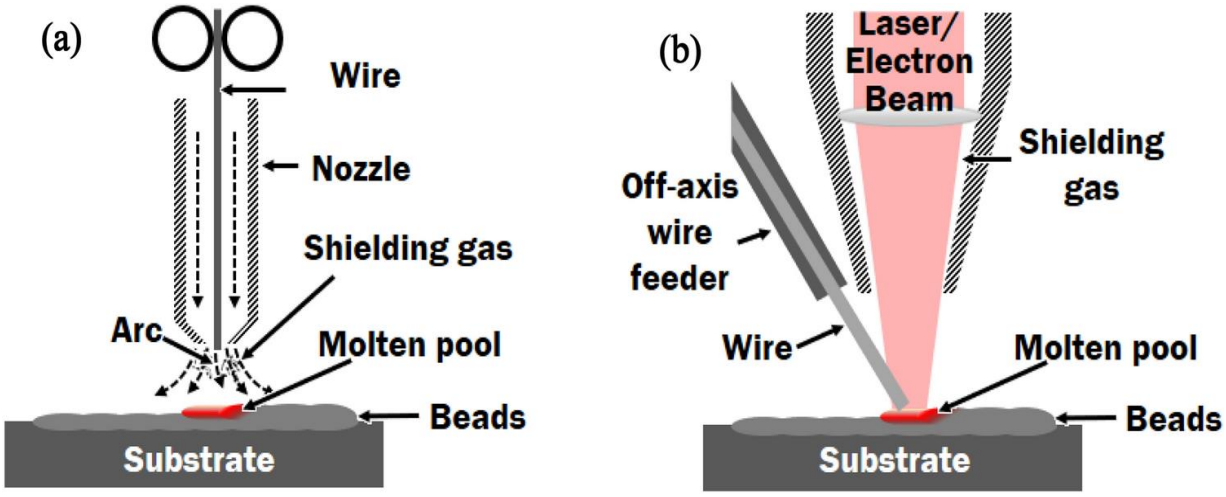

Figure 22 Wire-Fed DED printing shown with WAAM and LENS/ Electron Beam printing.[95]

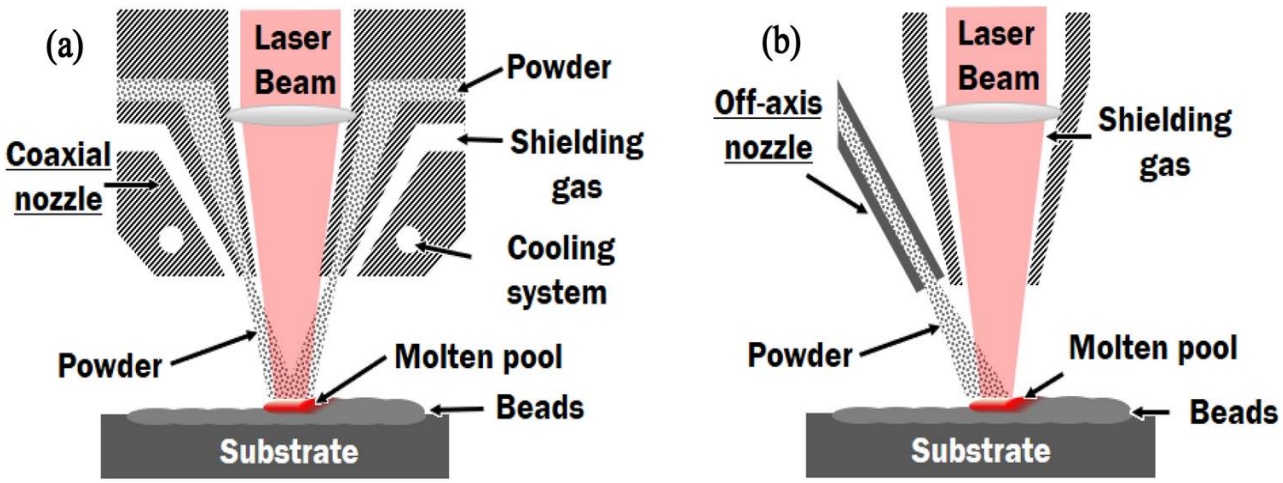

Figure 23 Powder-fed DED printing shown as LENS printing.[95]

While the material deposition methods differ significantly, the general manufacturing process is the same. The general printing process for DED systems after material preparation and setting machine offsets is as follows:

1. The building environment is atmosphere is evacuated or replaced with a non-reactive gas to create an inert environment.
2. The material deposition head prepares to dispense material by moving to the location of the initial user set offsets.
3. While the material deposition head is moving, material then begins to be deposited on the build plate to adhere the two together using an energy source.
4. After a layer has been successfully printed, there is a brief period that can be allotted to allow for the material to cool and allow the component to completely solidify before resuming.
5. The process is then repeated continuously for the following layers until the component is printed.
6. Once printing is completed, the component can then be removed from the printer and undergo post processing treatment.

Shown in Figure 24 is a schematic of a wire/powder-fed DED system, including the primary components found in all DED systems [96].

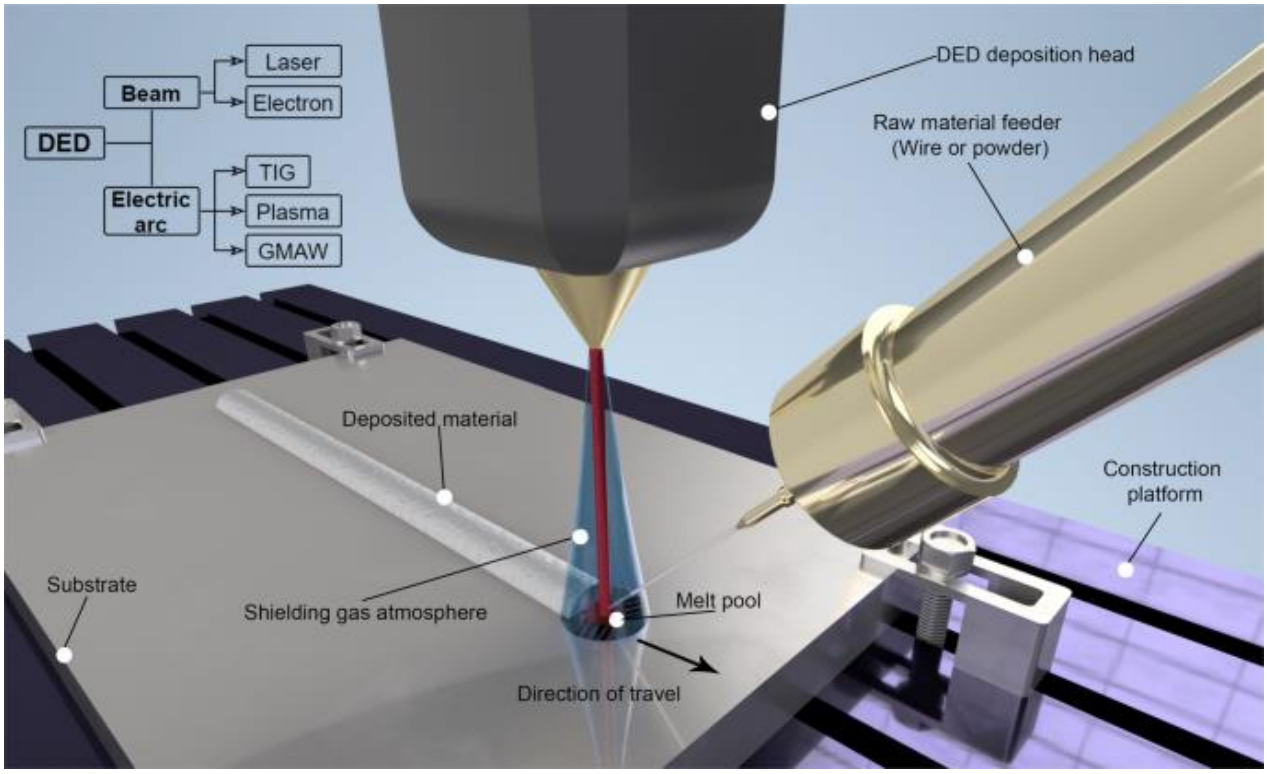

Figure 24 Wire/Powder fed DED system schematic [96].

Regarding large-scale metal AM, DED is the optimal choice for manufacturing. The advantages of DED printing are seen in its versatility amongst multiple metal alloys, the ability to repair components , and the ability to print with very high material deposition rates. Customizability in the manufacturing process can produce various components suited for many applications.

DED systems with multiple powder hoppers can be filled with different materials allowing for multi-material deposition when printing. The advantage is that different geometries can be manufactured with different materials allowing for different mechanical or thermal behavior across a printed component. For example, in the works of Boyuan Li et al., a nickel-aluminum-bronze/15-5PH stainless steel (NAB/15-5PH) alloy was created using a laser DED

system. The experiment concluded that the DED system could successfully adhere to a layer of NAB with a layer of 15-5PH and assess its mechanical behavior [97]. Other muti-material works have been conducted, seen by Catherine Schneider-Maunoury et al., where using a powder DED system, a wall of Ti-6Al-4V/Mo alloy was able to be constructed with varying concentrations of Mo as the component was being fabricated [98].

The second significant advantage of DED, making it a unique form of AM, is its capability to repair manufactured components. By printing on existing components, DED can repair components in damaged or worn states, restoring them to their original specifications and allowing for significant savings if refabrication is not a financially viable option. This has been investigated in literature seen by Matthieu Rauch et al., where Ti-6Al-4V aeronautical components were repaired using DED. The article found that using the same material to repair, Ti-6Al-4V gave the repaired comparable stress performance significantly different elongation behavior compared to printed and wrought specimens [99]. Additionally, Abdollah Saboori et al. also concluded, reviewing multiple case studies, that repairing components through DED is a viable solution in terms of cost savings and lead time [100].

The last advantage of DED is the high material deposition rates that allow for the rapid fabrication of significant components. DED printing can deposit material with deposition rates as fast as 2.5 kg/h – 10 kg/h with very high build volumes [101]. An example of large components manufactured through DED is rocket nozzles for NASA's Rapid Analysis and Manufacturing Propulsion Technology (RAMPT) team. Using DED, the RAMPT team successfully manufactured a metal rocket nozzle with a diameter of 40 in and a height of 38 inches [102].

While there are numerous advantages to DED, there are also several disadvantages associated with the technology—for instance, part resolution, minimum feature size, equipment

cost, and parameter development. When selecting DED, these drawbacks must also be considered to mitigate the effects of these disadvantages.

Resolution and minimum feature size are essential factors when manufacturing. When comparing DED to other metal AM processes, such as powder bed fusion, the printing resolution and minimum feature size can vary significantly. The typical print resolution, also known as layer height, of DED printing is typically between 250µm-500µm [103]. However, powder bed fusion printing techniques can vary between 20 to µm-80 µm, which is considerably smaller and significantly affects the minimum feature size of a component [104], [105]. Andrey Vyatskikh et al. compared the minimum feature size of metal AM printing methods. They found that the minimum feature size for powder bed technologies ranges between 10µm – 100µm, but the minimum feature size for DED printing ranges between 100µm – 2000µm, a magnitude higher [106]. In other words, DED printing is suitable for large-scale manufacturing at the expense of surface finish and detail.

Cost is another major drawback in DED systems ranging between tens of thousands of dollars to upward of a million dollars for industrial-grade systems. When combined with the high material cost for significant components, the cost can significantly impact the affordability of manufacturing or purchase of such a system. Hence, the cost of such a system can be a disincentive for the widespread adoption of this manufacturing technology.

Parameter development is also an issue of concern for DED significantly affects a component's outcome effect on the outcome of a component. For instance, laser power, deposition rate, feedstock velocity, and feedstock trajectory can significantly impact defect formation, residual stress, and microstructure [94]. Compared to other processes, such as

material extrusion, a manufacturing method is much more forgiving with its parameter sets, and the complexities of metal additive manufacturing can be seen.

DED is a revolutionary form of AM, and the current challenges of DED are within the process stability, surface finish, and investigating new materials. Today's research focuses on further understanding the topics to understand this printing process fully. The future work of DED investigates incorporating hybrid systems that allow for subtractive manufacturing to decrease post-processing significantly.

Process stability can be related to surface finish because constant parameters aid in a more consistent surface finish. In-situ monitoring using a vision-based approach to detect spatter and analyze melt pool formation are some of the methods currently being used today to optimize the process [107]. In addition, printing techniques are also being investigated to conclude if embedding sensors is possible for DED printing, as seen in the work of SEON Il Kim et al., where miniature nickel alloy turbine blades were embedded with high-temperature sensors [108]. Lastly, process parameters and heat-treatment methods are being explored to see how the AISI D2 Steel microstructure and hardness are affected [109]. The current research gives insight into the capabilities of DED and the improvements that can be made to understand the process better.

One of the significant future developments of DED printing is the addition of CNC surface post-processing methods after printing a component. An illustration in the works of Ian Gibson et al. depicts several DED systems combined with subtractive manufacturing, seen in Figure 25, where four setups are shown that can perform both additive and subtractive manufacturing [110].

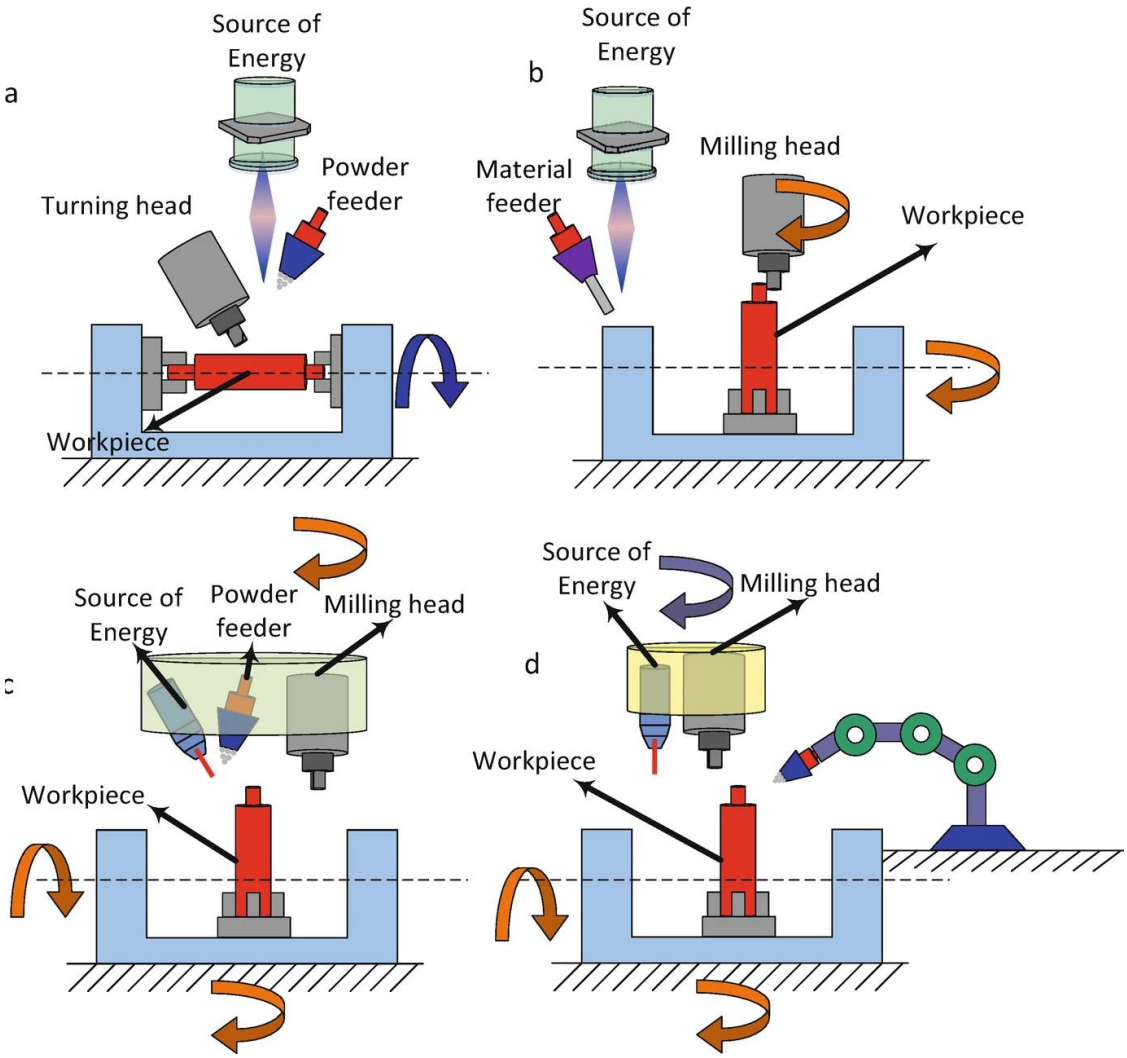

Figure 25 Hybrid DED setup a) Turing work hold with a separate turning head and printhead system b) Milling work hold with a separate milling head and printhead system c) integrated milling and printhead with multi-axis milling capabilities d) milling and laser integration with a separate powder feeding mechanism.[110]

In conclusion, DED is a revolutionary additive manufacturing technique allowing substantial components to be manufactured additively. By allowing for cladding, repairing, and multi-material manufacturing, it is evident why this is a desirable fabrication method. Nevertheless, the drawbacks, such as dimensional accuracy, surface finish, and the need for a consistent printing process, are issues that still require attention today. However, as improvements in DED continue to be made, applications across more industries can be expected.

2.8 Powder Bed Fusion

The seventh primary method of AM is Powder bed Fusion (PBF) which uses a powder bed and energy source to melt 2D contours until a solid object is created selectively. PBF can be separated into laser PBF (LPBF) and electron beam PBF (EB-PBF). LPBF is credited to Carl Deckard, who developed the technology in the late 1980s at the University of Texas at Austin using an inert environment to print, and commercial EB-PBF is credited to the company Arcam founded in the late 1990s, which prints in an evacuated environment [23], [111]. PBF is a versatile manufacturing method applicable to numerous metals, polymers, and ceramics, creating complex components. However, like all AM processes seen, the need for post-processing after manufacturing is still prevalent. Furthermore, the challenges of PBF are typically in the limited build volume, costly investment, and need for support structures when printing. Nevertheless, various industries use PBF manufacturing today, and it is one of the most extensively researched manufacturing methods in the literature.

PBF is a generic term encapsulating various manufacturing methods; while there may be slight differences amongst specific PBF methods, all methods operate on the same principle. A powder bed is placed on top of a building substrate and then welded to form a solid foundation to print. Two schematics of an LPBF printer and an EB-PBF printer can be seen in Figure 26 and Figure 27, depicting the major components of the printing process. The steps shown are a general process followed for PBF printers encapsulating the general printing process [112], [113]:

1. The build chamber is either evacuated or replaced with a non-reactive gas to create an inert environment.

2. A powder reservoir is raised a used defined distance above a building substrate, and a recoater evenly spreads powdered material over the entire substrate. Excess powder falls into a reserve reservoir.
3. An energy sources traces a 2D contour of the model and bonds a thin layer to the building substrate.
4. The building substrate is then lowered, and the powder reservoir is once again raised to allow for recoater to spread another layer of powdered material.
5. After powder is evenly distributed, another layer is then sintered to the preceding layer.
6. Steps 3 & 4 are repeated until a fully sintered component is successfully manufactured.
7. After manufacturing excess powder can be removed before taking the building substrate out of the build chamber.
8. The component can then undergo post processing treatment.

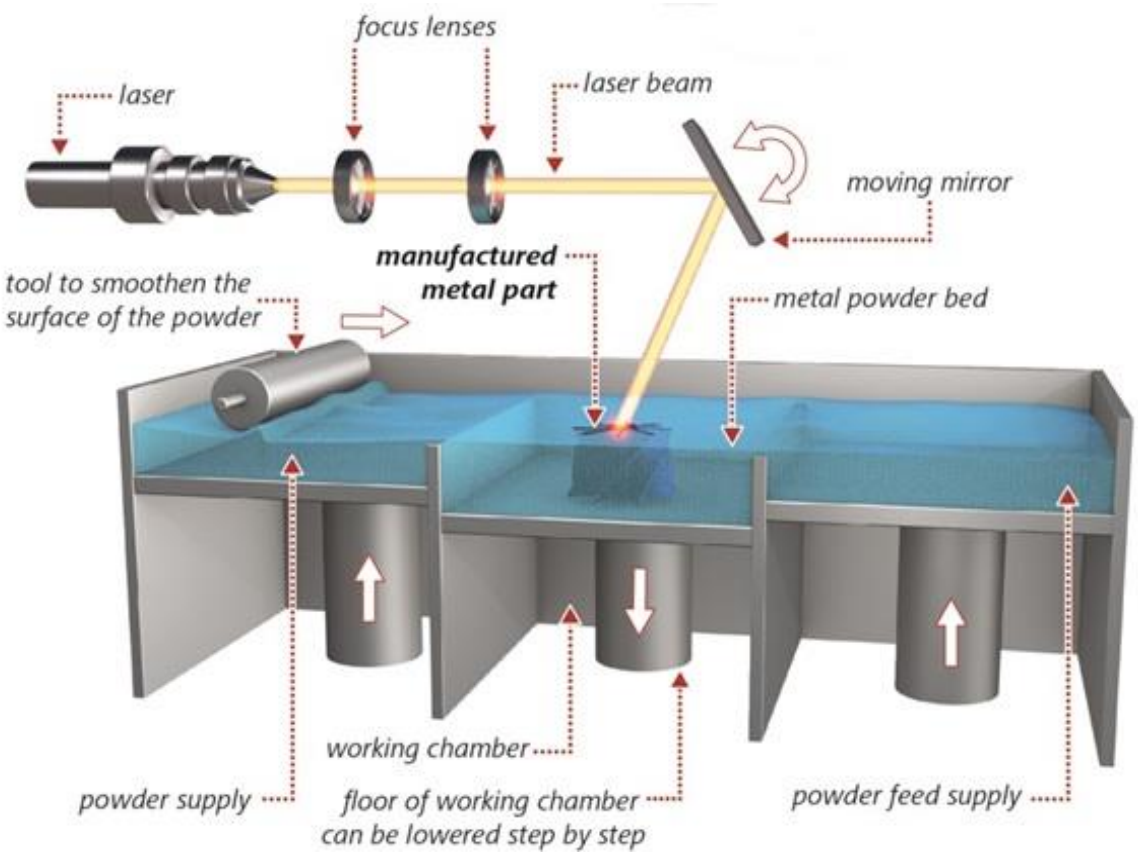

Figure 26 Schematic of a LPBF printer[112].

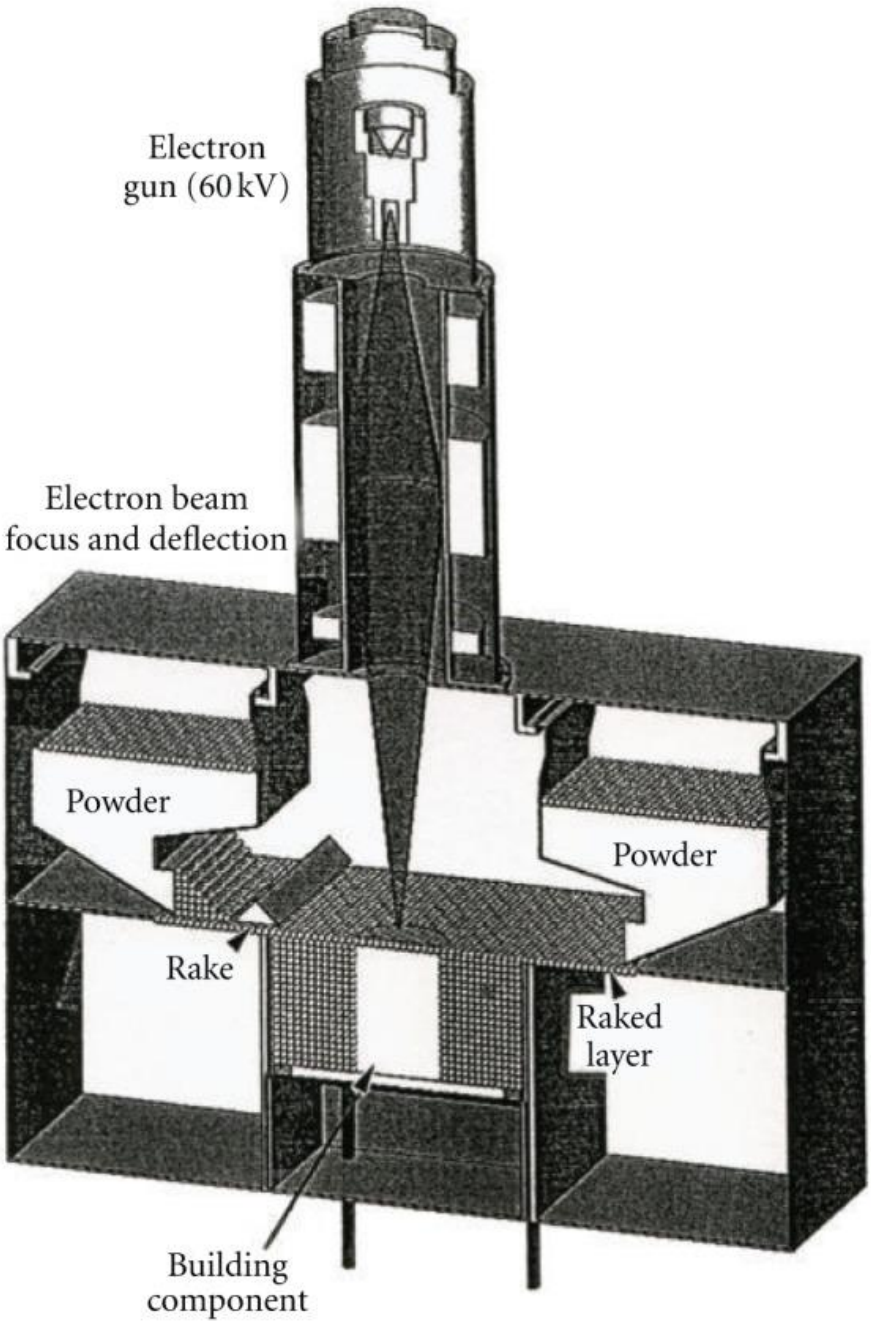

Figure 27 Schematic of EB-PBF Printer [113].

An advantage of PBF is its versatility spans various materials, making it applicable to most engineering applications [23]. However, the main advantage of PBF is its capability to sinter very complex geometries with intricate details that cannot be achieved through other methods of AM. The minimum feature size can vary depending on the method of PBF, but in the case of LPBF, it can achieve very high accuracy, as small as 10μm [114]. While it can be argued that binder jetting can achieve the same level of detail, PBF techniques can manufacture the component without sinter-post-processing at higher densities. In a recent article by Memgchen Xu et al., 316L stainless steel specimens were manufactured via binder jetting and LPBF to assess their mechanical properties. It was concluded that the LPBF samples had superior tensile properties and hardness at 99.20 ± 0.3%, while the binder jetting specimens achieved an overall density of 96.85 ± 0.54% [115].

The last significant advantage of PBF processes is reducing the need for stress-relieving components after printing. Most notably, while manufacturing significant components, DED requires stress relief from all the heat induced by the printing process. On the other hand, EB-PBF can print metal components with little residual stresses after printing. This is because, in the evacuated chamber, EB-PBF can preheat the powder bed to a near melting point before sintering. Nikolas Hrabe et al. investigated internal defects and residual stresses. They stated that the constant preheating of each layer for the duration of the print could mitigate much residual stress formation. The article concluded no significant residual stresses existed in Ti-6Al-4V samples printed via EB-PBF [116].

Advantages certainly qualify PBF as a fantastic form of manufacturing, but the limitations of PBF must also be considered when designing for PBF. The most notable

significant drawbacks are the need for support structures, limited build volume, and high operation and equipment costs.

Although offering heat dissipation, reduced thermal stress, and prevents deformation, the need for support structures can be defined as a disadvantage. Support structures limit geometric freedom and increase post-processing times with their removal. For instance, components with complex internal features may not be manufacturable through PBF because support structures may not be accessible after printing or may cause powder entrapment. In addition, much consideration must be taken into the design of support structures because of the effects on material usage, lead time, and part deformation [117], [118].

The maximum part size is also a significant limitation in PBF. The build volume of printers can vary depending on the system's manufacturer. However, as of today, large components manufactured through PBF must be multi-component assemblies because of the inability to accommodate larger projects. To provide more insight, EOS and Arcam printers are among the most popular systems used for research or industrial applications. The largest printers, EOS M 400-4 and Arcam Spectra L have built envelopes of 400 mm x 400 mm x 400 mm and ⌀350 mm x 430 mm, respectively [119], [120]. Meanwhile, the RPMI DED printers can manufacture metal components in build volumes as large as 5ft x 5ft x 7ft [121]. While both methods offer greater detail in the outcome, it is at the expense of maximum build volume.

Lastly, LPBF and EB-PBF are some of the costliest forms of manufacturing in all AM processes. For example, PBF systems can cost between $500,000 and $3,000,000 for the equipment [122]–[124]. In addition, other necessary expenses would be energy costs to create an inert atmosphere or vacuum. Since this is a significant concern affecting part quality, it is

necessary to maintain the environment. Coupled with the operational costs of the laser electron beam, in turn, it creates enormous expenditures.

Challenges and future developments include residual stress control, powder properties, and improving repeatability. There is extensive research in all fields in efforts to improve PBF processes, with new developments being made to enhance the effectiveness and efficiency of PBF. The most common issue in manufacturing with PBF is residual stresses, the internal stresses within an object due to the rapid heating and cooling inherent in the printing process [125]. The processing parameters and heat treatments have been investigated to counter these effects. Naresh Nadammal et al. investigated the effects four different scan strategies had on the microstructure and residual stresses when printing Inconel 718 via LPBF. The works concluded that scanning strategies significantly impact the microstructure and that hatch length, a standard printing parameter, can induce high residual stress [126]. These findings were also prevalent in the work of J. Robinson et al., where printing multiple samples of pure titanium via LPBF with different scanning strategies, including unidirectional, alternating X and Y scanning, and varied chequerboard patterns. Using ASTM measuring techniques, it was concluded that all methods had high magnitudes of stress except alternating X and Y scanning because of the uniformity of heat distribution during printing [127]. Regarding EB-PBF, a fatigue study investigated how hot isostatic pressing, stress-relieved, and as-built samples behave under cyclical conditions. However, it was concluded that the as-built and stress-relieved samples had relatively comparable fatigue life because of the low residual stress in the as-built samples [116].

Powder morphology is also a significant concern that is currently being researched. While powder manufacturing has been a standard method for many decades, applications in PBF are very recent. The morphology of the powder is crucial to the outcome of any printed

component as it can significantly affect the printing process and outcome of a printed component [128]. As seen in various studies, there is a consensus that poor powder distribution and circularity affect the flowability and spreadability of powder, leading to poorly printed components [128]–[130].

Lastly, the repeatability of manufactured components through AM is also a significant concern because the current printing process involves numerous variables that inherently prevent repeatability. These variables include complex printing parameters, powder morphology, build orientation, and layer thickness affecting numerous properties in the printed component, including mechanical properties and microstructure [131]. The most recent research has proposed solutions with in-process monitoring and applications of machine learning algorithms to predict and identify common behaviors in PBF [131], [132]. Overall, the research will give a deeper understanding of PBF and improve the quality of printed components.

PBF is a broad term that encapsulates a complex additive manufacturing method. There are many advantages to PBF. Namely, highly complex components will have nearly 100% density and, in some instances manufacturing without the need for stress-reliving. It is also essential to note that PBF has limitations, such as the need for support structures, high cost, and limited build volume, which prevent it from becoming a more widely adopted manufacturing method. Well, future research continues to evolve PBF. This form of AM will continue to revolutionize manufacturing.

2.9 Lack of fusion defects in Laser Powder Bed Fusion

Process parameters are vital to LPBF by affecting a printed component's surface quality, mechanical properties, microstructure, defect formation, and density. Some parameters include laser power, scanning speed, hatch spacing, and layer thickness. These parameters define the

energy density shown in Equation 1, where p is the laser power (W), v is the scanning velocity, h is the hatch distance, and t is the layer thickness. The energy density used with processing parameter values gives insight into the outcome of the printed component. While not an infallible approach to the manufacturing process, specific defects can be predicted based on the energy density value.

$$Energy\ Density = \frac{P}{v\ h\ t}$$

Equation 1 Energy density defined by processing parameters in LPBF.

Lack of fusion is a defect in LPBF where a low energy density leads to poor melt pool formation, not allowing for proper fusion between adjacent layers [133]–[137]. Changing process parameters alters the melt pool's overall size, altering the sintering between powder and subsequent layers. Therefore, decreasing the melt pool size makes components more vulnerable to a lack of fusion defects. This lack of binding within subsequent layers due to LoF also increases the porosity, affecting the overall mechanical performance of the built component [138], [139]. Although the defects may not always be seen on a macroscopic scale, the defects are apparent in stronger microscopy methods. Detection of lack of fusion defects exists through non-destructive testing, such as CT scanning, and newer methods, such as seen by Sam Coeck et al., where the light emitted from the laser spot can be recorded to predict a lack of fusion porosity [140]. Destructive testing for lack of fusion defects can also be analyzed through cross-sectional analysis and a pycnometer. Figure 29 illustrates a melt pool printing without fusion defects [141], [142].

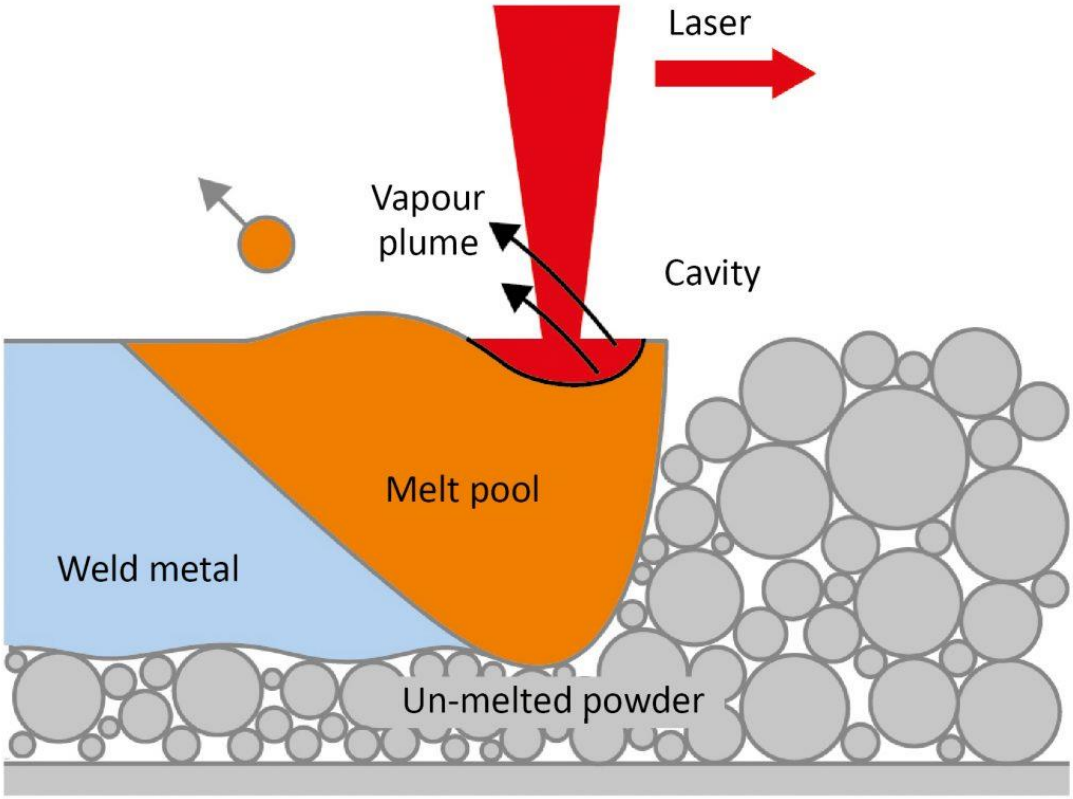

Figure 28 Melt pool illustration for lack of fusion defect printing via LPBF [142]

2.10 KEYHOLE DEFECTS IN LASER POWDER BED FUSION

In contrast to the lack of fusion, keyhole defects, named after their distinct keyhole shape, occur with high energy densities with high laser powers or low scanning speeds [143]. Keyhole defects are tiny pores formed due to either melt pool instability or metal vaporization when the laser interacts with unmelted powder [144]. Because the energy density is so high, a sizeable unstable melt pool collapses, leaving behind unique circular pores of entrapped gas, affecting the printed material's mechanical performance [145], [146]. Seen in Figure 29 are micrographs of stainless steel 316L with apparent keyhole pores, and Figure 30 illustrates the melt pool formation of keyhole pores during LPBF printing [141], [147].

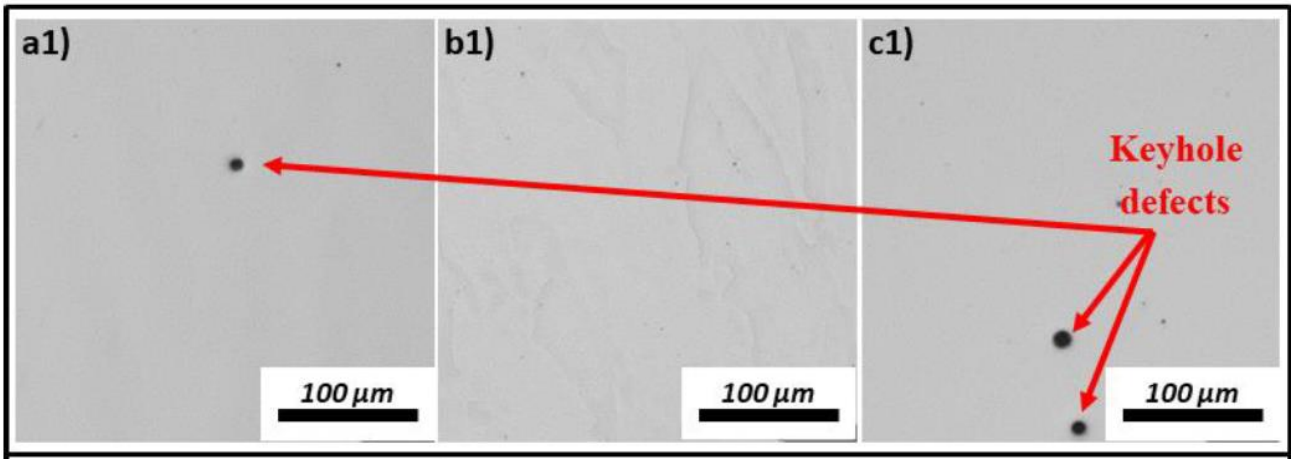

Figure 29 Micrographs of stainless steel 316L with keyhole defects [141].

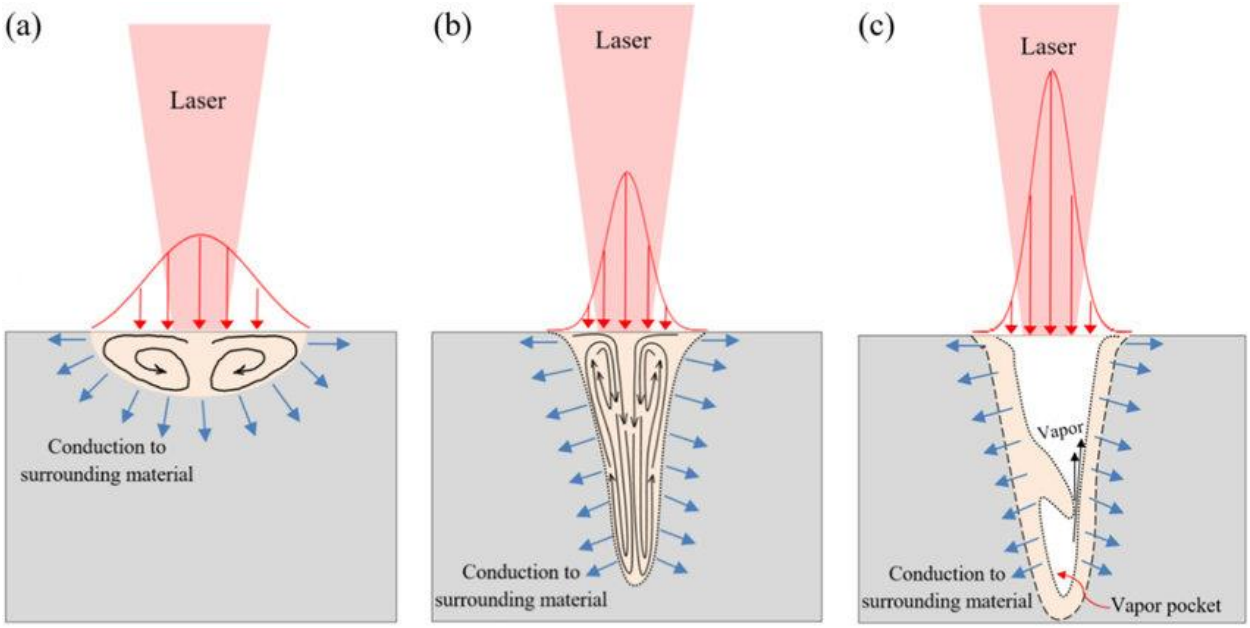

Figure 30 Melt pool formation of keyhole mode and collapsing melt pool[147].

Detection for keyhole defects is similar to the methods for detecting the lack of fusion defects. However, in recent literature, methods for detecting defects with in-situ monitoring have also been proposed. For example, Jean- Baptiste Forien et al. investigated the relationship

between in situ pyrometry and ex-situ x-ray radiography. They concluded that there is a relationship between the two and are necessary for process monitoring when manufacturing through LPBF [148].

2.11 Process window parameters in Laser Powder Bed Fusion

Process window parameters are parameter sets with a higher possibility to increase the density within printed components limiting the occurrence of keyholes and lack of fusion defects. Typically found experimentally, as seen in the works of Holden Heyer et al. where AlSi10Mg was printed via LPBF with varying hatch spacings, laser powers, scanning speeds, and layer heights. In the study energy densities created from the varying parameters were evaluated ranging between 6.4 J/mm^3 and 640 J/mm^3 across a total of 55 12mm x 12mm x 12mm cubes . Microstructure, melt pool morphology, and density measurements were then conducted to analyze the effect of the varying parameters. It was concluded that lower energy densities significantly impacted density of the printed component ranging between 75.3% and 99.5% dense when measured by Archimedes method [149]. No mechanical testing was conducted however it is accepted in literature that process induced defects do worsen mechanical performance[150]–[152]. Shown in Figure 31 is a modified figure from Holden Heyer et al work

depicting micrographs printed at varied process. The figure was modified to group the parameters by defect [149].

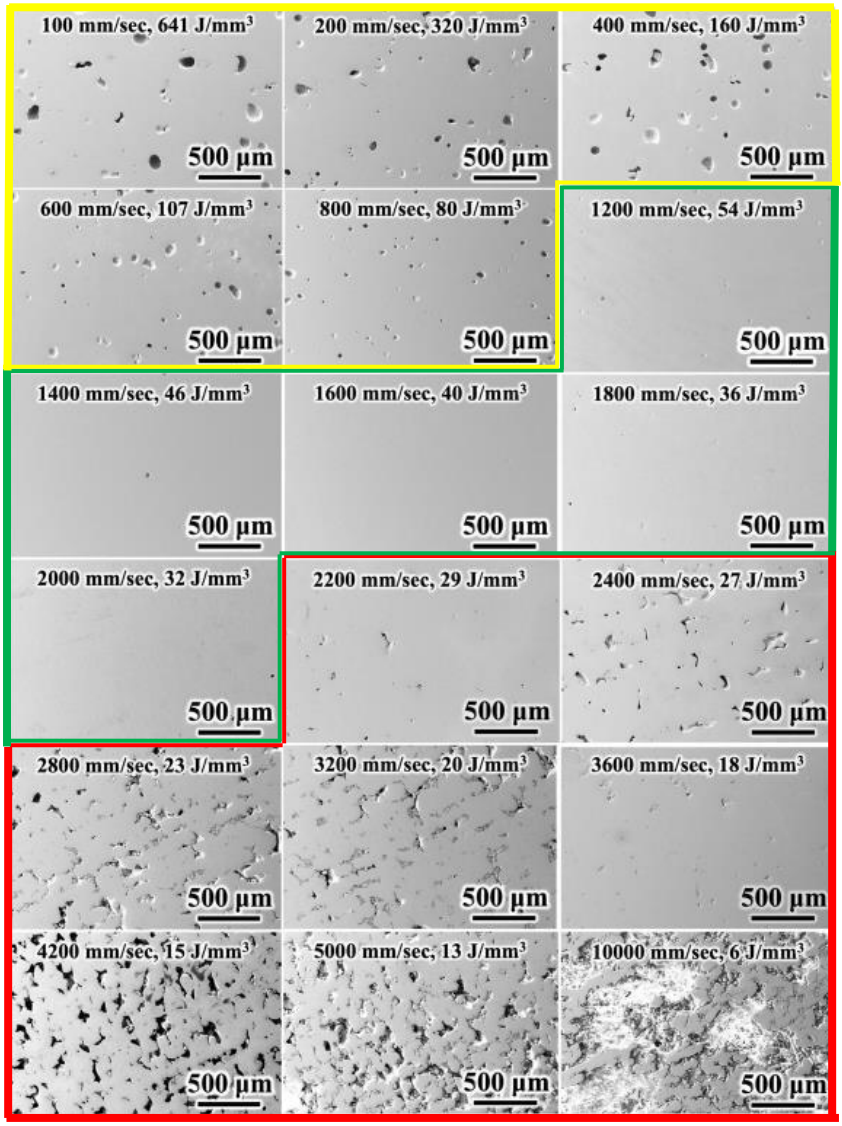

Figure 31 Modified figure showing micrographs printed at 250 W laser power and 30µm layer hight at varying laser scanning speeds. The lower group (Red) represents lack of fusion printing, the middle group (Green) is the process window, and the top group (Yellow) depicts keyhole parameters. [149]

2.12 Surface Roughness

Surface roughness, also known as surface finish, is a measurement of the height variations on an object's surface [153]. This critical attribute is an inherent characteristic of the LPBF manufacturing process responsible for the mechanical behavior of components. Many parameters affect the outcome of the surface roughness; for example, the laser, as mentioned

earlier, power and scanning velocity significantly affect surface roughness, but the roughness can also be affected by powder size, powder morphology, and scan strategy. Understanding surface roughness's impact on AM components is vital to optimizing mechanical performance and part quality.

Rough surfaces in powder AM occur naturally within the process for many reasons. For example, large layer heights lead to the stair-step effect, as seen in Figure 18 for material extrusion. Another contributing factor to rough surfaces in metal AM is powder morphology, where irregular powder geometry leads to rougher surfaces. Andrew H. Chern et al. investigated the effects surface roughness and built orientation have on the microstructure and mechanical behavior of Ti-6Al-4V fabricated via EB-PBF. The study involved printing 5 Ti-6Al-4V blocks horizontally or vertically along a build plate. The samples were removed from the build plate and machined for flexural 4-point bending fatigue testing. The study concluded that the as-built surface roughness must be removed to increase fatigue life through surface post-processing [154].

One of the most common methods to measure surface roughness is profilometry, a contact method that uses a stylus across a line. The most common variables seen throughout the literature are Ra or Rz, where R signifies a straight segment measured across a surface, subscript *a* signifies the average surface depth over a measured segment, and *z* signifies the absolute depth over a measured segment. While there are many pros to using profilometers in terms of accuracy, the main limitation is that the measurement area is only a line in one axis of travel.

Optical profilometry may also be considered for more extensive analysis methods to measure surface roughness. Unlike a profilometer with a stylus, optical profilometry can obtain

surface roughness measurements with no contact. In addition, an entire surface can be measured versus a line segment, usually expressed as S_a or S_z, , where S signifies a specified area measured within a surface.

The last popular method used is also SEM profilometry, where the surface roughness is highly precise. However, SEM is typically very time-consuming and may require conductive coatings for non-metallic material manufactured through AM. In addition, equipment and operation cost is exceptionally high for SEM.

2.13 FATIGUE TESTING

One of the most popular methods to assess the mechanical properties of a material is fatigue testing. *Fatigue* is defined as the failure of a component subjected to cyclical loadings [155]. The importance of fatigue testing is understood across many industries, such as the automotive, aerospace, biomedical fields, and civil engineering, because all components undergo some form of cyclical loading. Therefore, it is paramount to assess the fatigue life of materials to predict the number of cycles a material can be subjected to before failure.

Various modes of failure can also be assessed for fatigue testing; for example, standard fatigue testing methods are tension-compression testing, torsional fatigue testing, and flexural fatigue testing. However, all methods can be categorized by repeated loading until failure. In addition, the fatigue life stresses of fatigue testing can be defined by two types of cyclical loading: low cycle fatigue and high cycle fatigue.

Low cycle fatigue (LCF) is a method of fatigue testing that evaluates the fatigue failure of a material at high stresses that subject the material to plastic deformation with every cycle accumulating plastic strain. The accumulation of plastic strain with every cycle induces changes to the microstructure and indications of cracks within the specimen [156]. LCF testing is

conducted at higher stress amplitudes at a lower frequency because failure is expected at fewer cycles, typically between 10^4 and 10^5. The importance of LCF is to assess how components fail under specific conditions with very high stresses, and the results generated from LCF testing create stress-life (S-N) curves that are useful for determining a material's LCF properties.

On the other hand, high cycle fatigue (HCF) evaluates fatigue behavior at lower stress levels at failure at a higher number of cycles. The stress levels tested are within the elastic region, meaning that failure is primarily due to the propagation of cracks formed from cyclical wear on the surface. HCF testing is critical because most engineered components do not undergo monotonic loading and are subjected to cyclical loads throughout their service life; Therefore, it is imperative to understand the fatigue behavior to ensure the reliability of the components. Like LCF, the data obtained from HCF testing can also be plotted along an S-N curve.

2.14 Analysis of Fatigue Data

Other than experimentation, data analysis is also imperative to fully understand a material's fatigue behavior. There are various methods to analyze fatigue data, the most popular method being the Wöhler Curve, also known as an S-N curve. However, for a statistical approach, various methods are used to analyze fatigue data, such as Basquin's Equation, the Goodman Diagram, Miner's Rule, and the Coffin-Manson relationship..

A visual representation of common terminology in fatigue testing can be shown in Figure 32 where Stress vs. Number of cycles is plotted as a sinusoidal waveform [157]. σ_r is defined as the range difference between the maximum stress (σ_{max}) and minimum stress (σ_{min}) shown in Equation 2. The stress range is also used to define a test's amplitude (σ_a) by taking half of σ_r shown in Equation 3. Equation 4 shows the formula to calculate the mean stress (σ_m) , an

essential test parameter that can influence the fatigue life by adding extra load to specimens [158].

$$\sigma_r = \sigma_{max} - \sigma_{min}$$

Equation 2 Stress Range defined by the difference between the maximum stress and minimum stress.

$$\sigma_a = \frac{\sigma_r}{2} = \frac{\sigma_{max} - \sigma_{min}}{2}$$

Equation 3 Stress amplitude defined by half of the stress range.

$$\sigma_m = \frac{\sigma_{max} + \sigma_{min}}{2}$$

Equation 4 The mean stress defined by half the sum of the maximum and minimum stress.

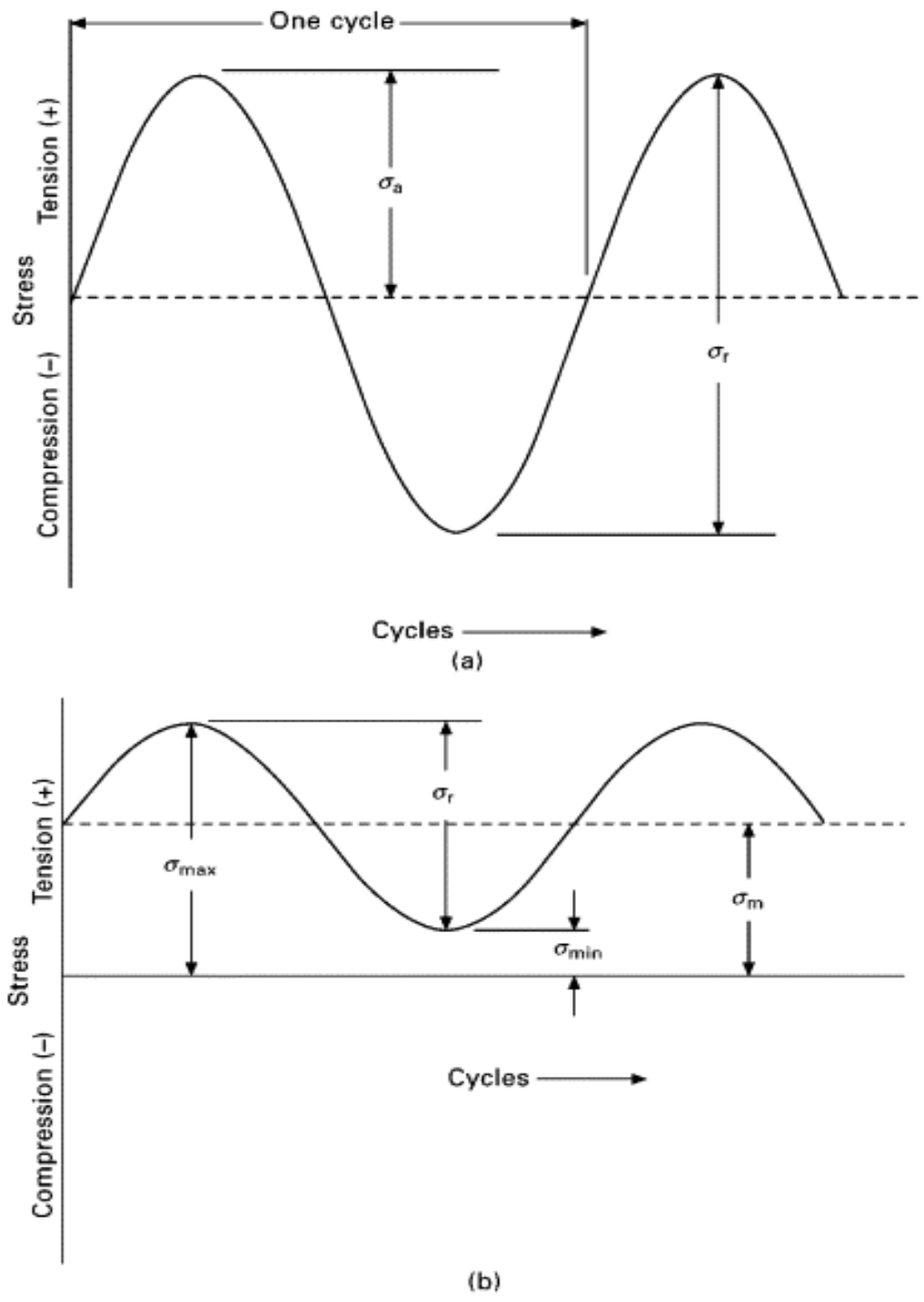

Figure 32 Stress vs Time waves used in fatigue testing labeled with common terms used in fatigue testing [157].

The Wöhler Curve (S-N Curve) is most commonly used to graph fatigue life data. The term S-N stands for stress vs. the number of cycles, and the curves depict the relationship between the fatigue life of a material at a given magnitude of stress. The Y-axis stress is typically reported as the stress amplitude, as seen from Equation 3 The X-axis represents the number of cycles until failure, usually reported in a logarithmic scale because the number of cycles until fracture significantly varies between high and low stresses. At low amplitudes of stress, some materials never fracture, creating an area known as the endurance limit where material can be expected to undergo an infinite number of cycles without failure. However, it is essential to note that some materials, typically non-ferrous metals, do not have a specific endurance limit but can be designed for high-fatigue life applications. Seen in Figure 33 are defined regions on S-N curves, where the infinite life region also refers to the endurance limit of material [159].

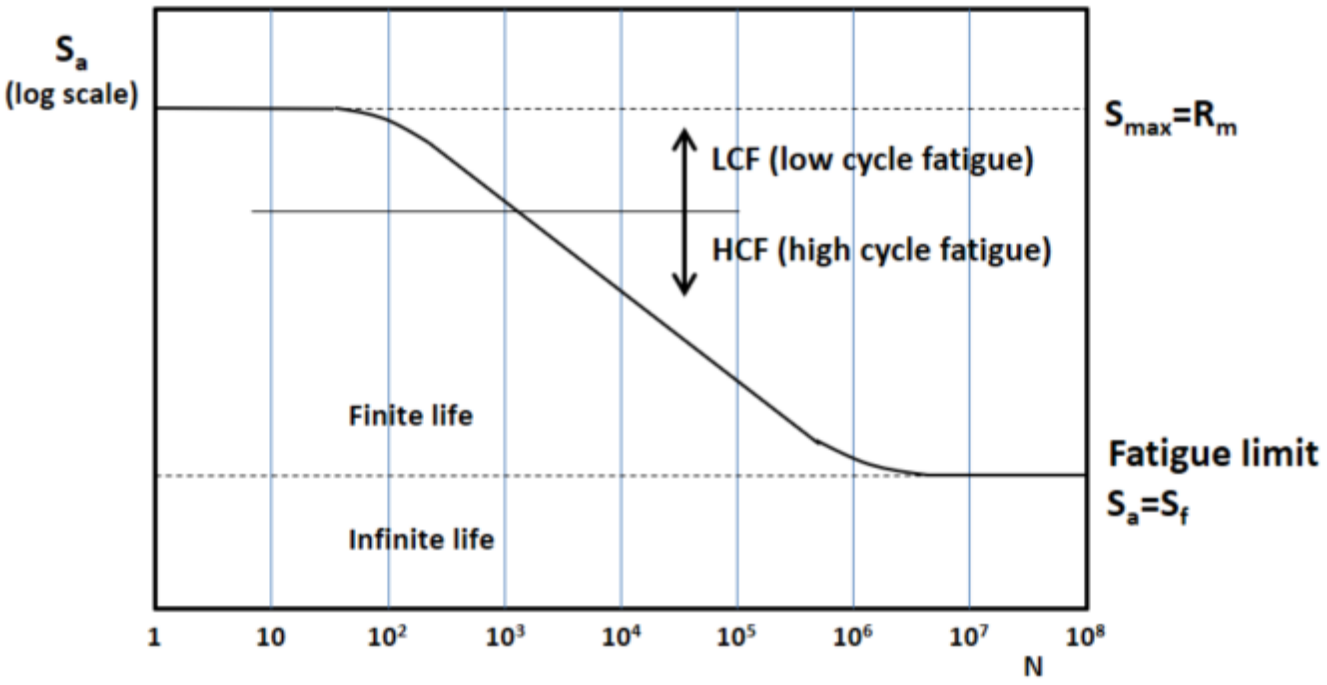

Figure 33 Wöhler Curve (S-N Curve) with logarithmic X-Y axis indicating important regions for fatigue behavior [159].

Basquin's Equation is a fundamental formula that describes the relationship between the stress range and the number of cycles until failure. In a sense, this is a more mathematical approach to the Wöhler Curve. Basquin equation is defined by Equation 5:

$$\sigma_r = a\ (N_f)^b$$

Equation 5 Basquin's Equation were σ_r is the stress range, a and b are material properties, and N_f is the number of cycles until failure.

Equation 5 Basquin's Equation where σ_r is the stress range, a and b are material properties, and N_f is the number of cycles until failure. Basquin's Equation predicts the number of cycles a material can endure before fracture. However, it is essential to note that this estimation can be used for HCF and does not consider the surface finish, temperature, size effect, or environment. In addition, Basquin's Equation does not apply once the endurance limit is reached because the fracture is not expected within that region.

The Goodman Diagram is a line that describes the relationship between the stress amplitude and the mean stress on a material. It is a graphical representation where the Y-axis represents the stress amplitude, and the X-axis represents the mean stress. A line is then drawn intersecting the X and Y-axis at the ultimate tensile stress and endurance limit stress, respectively. The intersecting line creates a region where any coordinate pair under the line is considered safe and will not fracture, and any coordinate pairs on or above the line will fracture the component. While this line only approximates the fatigue behavior, many other similar methods, such as the Soderberg, Gerber, or Yield (Langer) lines, are similar to the Goodman line. However, they are methods that try to accommodate the complexities of fatigue behavior. Figure 34 shows all the lines mentioned earlier to illustrate the differences between their classification of the safe region for cyclical loads [160].

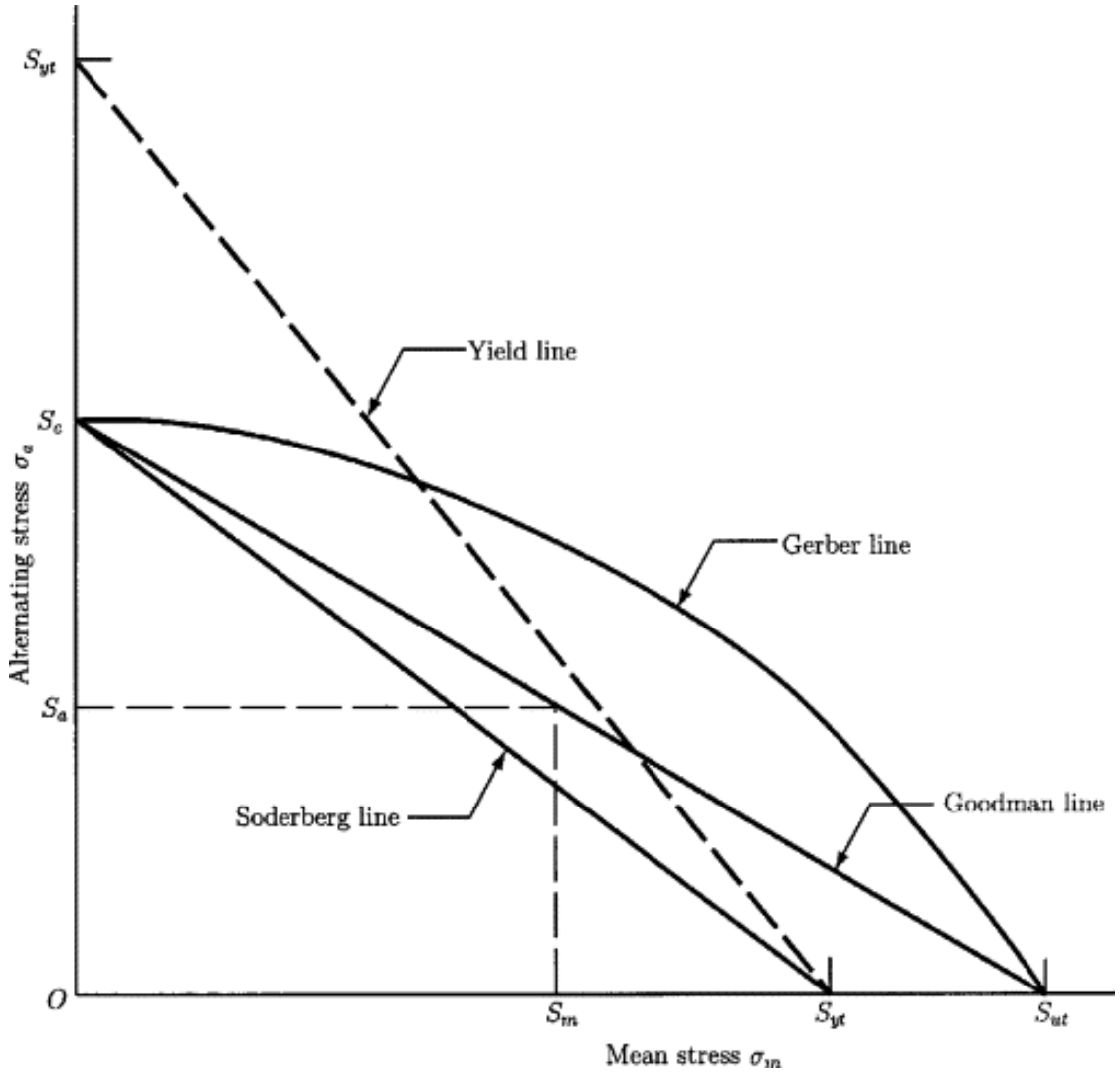

Figure 34 Graph showing a modified Goodman line, Gerber line, Soderberg line, and Yield line.[160]

Miner's rule is a method used to predict the failure of a component subjected to multiple cyclical loads over an extended period. The general concept of Miner's rule assumes that cyclic damage is accumulated and can be represented as a ratio between the number of cycles a component has been subjected to divided by the number of cycles required to fracture a component. This accumulation of damage is then summed up, and if the sum is equal to or greater than 1, the component is expected to fail, but if the sum of the ratios is less than 1, then the component is not expected to fracture. Shown in Equation 6 is the general Equation for

Miner's rule expressed as a summation. The only limitation of Miner's rule is that it is a generalization and does not account for many variables, such as the order in which loads are applied, surface finish, or variable-amplitude loading. Nevertheless, it is an approximation that can give insight into the fatigue life of a component.

$$D = \sum \frac{n}{N_f}$$

Equation 6 General equation of Miner's Rule where D is the total accumulation of cyclical damage, n is the number of cycles experienced at a certain stress, and N_f is the number of cycles until failure is expected .

For LCF, a standard method to assess the data obtained from testing is the Coffin-Manson relationship. The principles are similar to Basquin's law, where material properties are used to predict the number of cycles until failure; however, the Coffin-Manson relationship predicts the cycles of failure using plastic strain amplitude, whereas Basquin's law uses the elastic stress on a component [161]. Equation 7 shows the Coffin-Manson relationship defined by the material properties, stress amplitude, and number of cycles to failure. The Coffin-Manson equation combined with Basquin's law is essential to describe the relationship between plastic and elastic cyclical behavior fully. Seen in Figure 35 are linear fittings of the plastic and elastic strain amplitudes where the Y-axis represents the strain amplitude on a logarithmic scale and the X-axis represents the number of cycles until failure also on a logarithmic scale [162].

$$\frac{\Delta\varepsilon_p}{2} = \varepsilon_{f'}(2N_f)^b$$

Equation 7 Coffin-Manson equation where $\Delta\varepsilon_p$ is the amplitude of plastic strain, $\varepsilon_{p'}$ is the fatigue ductility coefficient, N_f is the number of cycles until failure, and b is the fatigue ductility exponent.

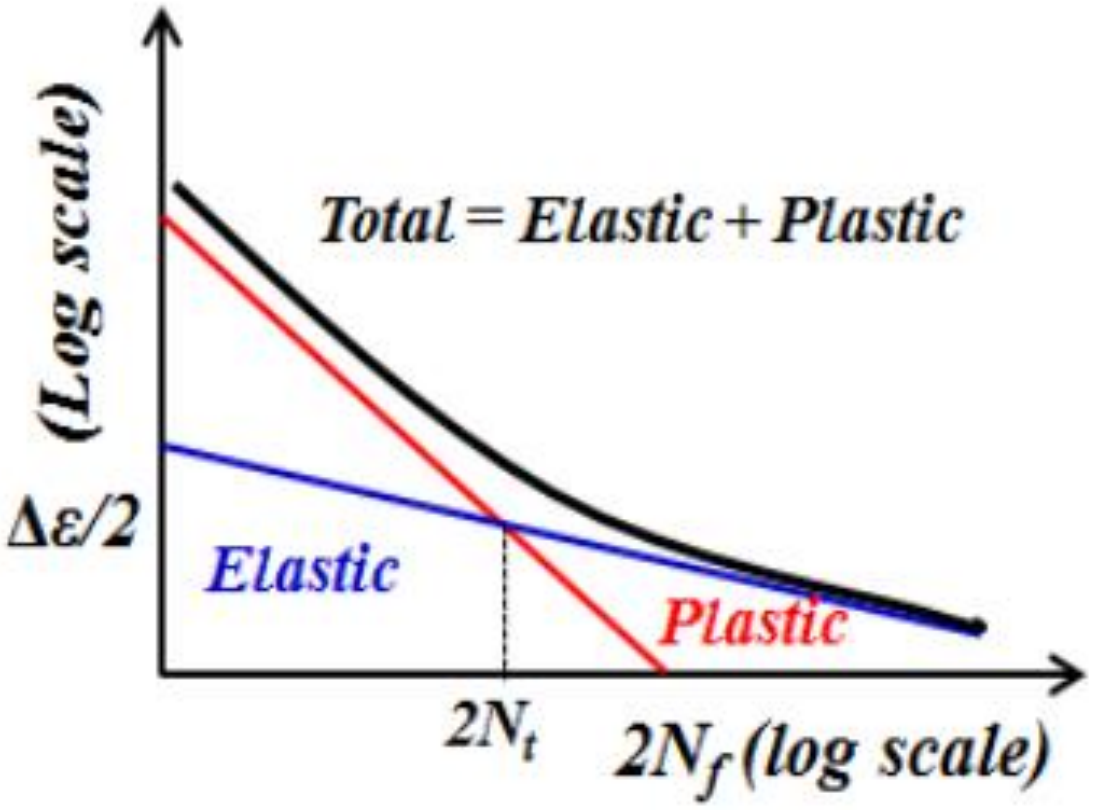

Figure 35 The relationship between plastic strain amplitude and elastic strain amplitude with linear fittings to identify the transition point bet for a material [162].

Chapter 3: Materials and Methods

3.1 Powder Feedstock

AMS 4928 Ti-6Al-4V (Ti64) powder feedstock was supplied by Allegheny Technologies Incorporated (North Carolina, USA) and made through electrode induction melt-gas atomization. The particle size range is +15µm/-53µm with a particle distribution of D10 = 26.4µm, D50 = 27.2 µm, and D90 = 54.7 µm. The chemical composition of the Ti64 feedstock was certified through combustion/IR detection (CIR), inert gas fusion (IGF), and inductively coupled plasma emission (ICPE) testing following their respective ASTM standards. Seen in Table 1 is the chemical breakdown of the Ti64 feedstock represented by their percentage of weight present.

Table 1 Chemical composition of the Ti64 powder feedstock by %-weight, and their respective material characterization method

Element	% Measured	Testing Method
Ti	Balance	N/A
Al	6.09 %	ICPE
V	3.89 %	ICPE
Fe	0.22 %	ICPE
O	0.149 %	IGF
C	0.011 %	CIR
N	0.013 %	IGF
Y	$< 9*10^{-4}$ %	ICPE
H	$8*10^{-4}$ %	IGF

3.2 LPBF SETUP AND PROCESS PARAMETERS

The specimens were manufactured using an EOS (Krailling, Germany) M290 printer. The M290 contains a 250 mm x 250 mm x 325 mm (.0203 m3) build envelope and is equipped with a yttrium fiber laser with a maximum laser power of 400 W. The samples were manufactured with a layer height of 30 µm and varied in scanning speed and laser power. Five laser scanning speeds and powers were chosen to manufacture the samples using a power-velocity curve for Ti64 at 30µm shown in Figure 36. The keyhole and lack of fusion (LoF) parameters have different scanning speeds (800 mm/s and 2000 mm/s, respectively) but the same laser power (370 W). The process window (PW) parameter used the same laser power at a different scanning speed (1400 mm/s). EOS Nominal (NOM) and EOS Nominal improved (Nom IM) had the same laser power and scanning speed (280W and 1200 mm/s).

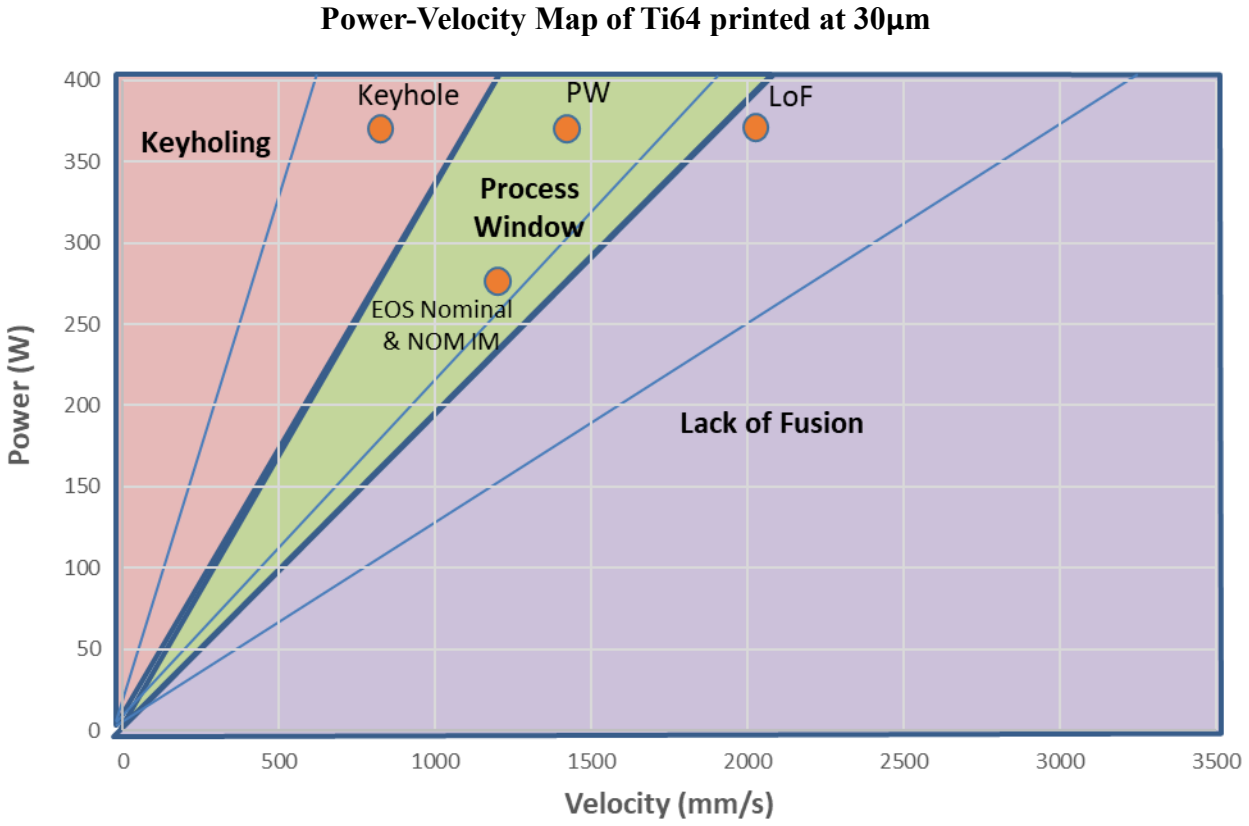

Figure 36 Power Velocity map of Ti64 at 30µm showing the 5-scanning speed - laser power pairs chosen named by the region which the parameter is in.

Table 2 The scanning speeds and laser powers chosen.

Process Parameters by Laser Speed and Power			
Process Parameters	Laser Power (J)	Scanning Velocity (mm/s)	Hatch Distance (mm)
Keyhole	370	800	.140
Process Window (PW)	370	1400	.140
Lack of Fusion (LoF)	370	2000	.140
EOS Nominal (NOM)	280	1200	.140
EOS Nominal Improved (Nom IM)	280	1200	.140

3.3 MANUFACTURING STRATEGY

The test specimens were manufactured with a 5 mm x 5 mm square cross-section and 70 mm in height. A total of 85 samples were manufactured, with 45 samples placed in the center in a diamond orientation for the baseline study (Figure 37). The remaining 40 samples were separated into equal groups and printed on all four corners of the build plate to be used for future testing.

Nine samples of each process parameter were printed and randomly selected from the baseline group. Two scanning strategies were selected for printing. NOM followed the recommended EOS scanning strategy for Ti64, and the other process parameters used a custom scanning strategy that included an additional contour remelting the surface. An illustration of the printing strategy can be seen in Figure 38 with Table 3 & Table 4 as reference to the parameters used for the contouring strategy.

After printing and depowdering, the 45 samples were stress relieved at 600°C for 120 minutes in a vacuum environment with a heating/cooling rate of 5°C/min before the samples were removed from the build plate. No surface post-processing was conducted on the specimens.

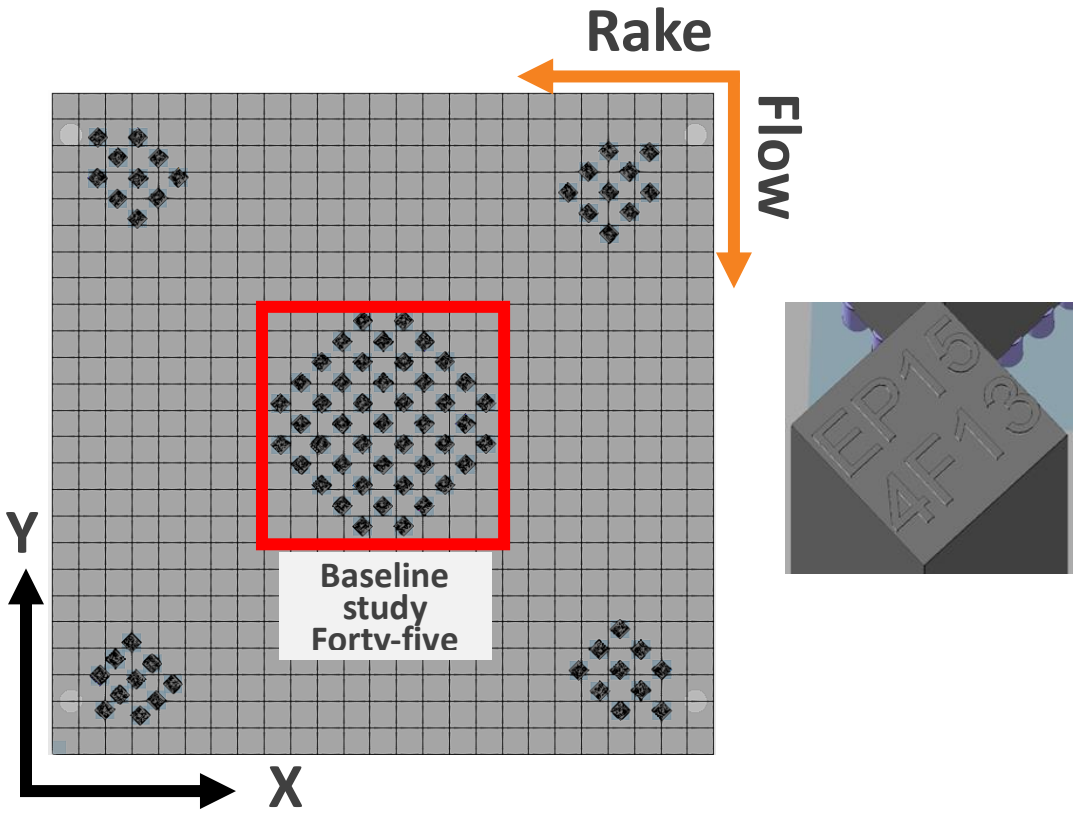

Figure 37 (a) Built plate orientation for the fatigue specimens. (b) isometric view of the top of the specimen with the sample identifier

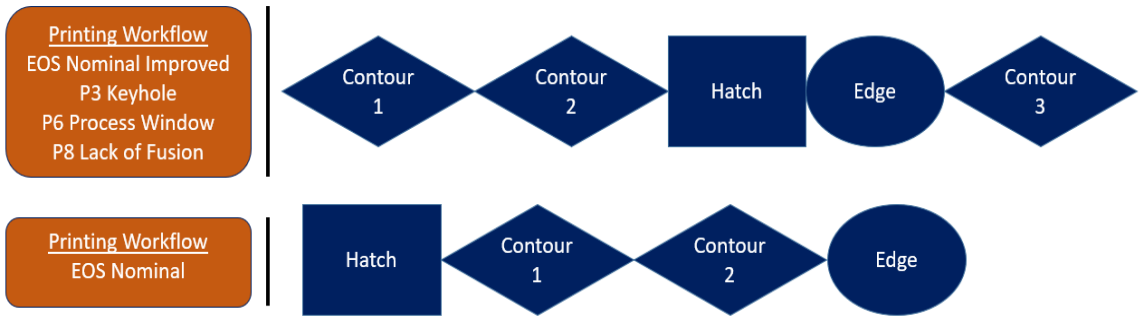

Figure 38 Scanning strategy used for the baseline build.

Table 3 Number of contour layers and offsets used by process parameter.

Process Parameter	Hatch Offset (mm)	Contour 1 Offset (mm)	Contour 2 Offset (mm)	Contour 3 Offset (mm)	Contour 1 Layers	Contour 2 Layers	Contour 3 Layers
EOS Nominal Improved	0.12	0	0.08	0	4	4	4
Keyhole	0.12	0	0.08	0	4	4	1
Process Window	0.12	0	0.08	0	4	4	1
Lack of Fusion	0.12	0	0.08	0	4	4	1
EOS Nominal	0.015	0.02	0	None	2	2	None

Table 4 Laser Power and Scanning Speeds used by process parameter

Process Parameter	Contour 1 Speed (mm/s)	Contour 2 Speed (mm/s)	Contour 3 Speed (mm/s)	Contour 1 Power (W)	Contour 2 Power (W)	Contour 3 Power (W)
EOS Nominal Improved	450	450	550	100	100	150
Keyhole	450	450	550	100	100	150
Process Window	450	450	550	100	100	150
Lack of Fusion	450	450	550	100	100	150
EOS Nominal	1250	1250	No Contour 3	150	150	No Contour 3

3.4 Surface Roughness analysis

Surface roughness measurements were conducted using a Keyence VR-5000 optical microscope. Average surface roughness (S_a) measurements were taken before sectioning and imaging samples. The obtained data were then averaged and reported per process parameter.

3.5 Sample preparation for Imaging

Thirty samples were sectioned, six per process parameter, with a Brilliant 220 precision cutoff machine and a silicon carbide cutting wheel by QATM (Rheinland-Pfalz, Germany). Each sample was sectioned into two pieces, one across the XY axis and another across the YZ axis. After sectioning, the samples were hot-mounted using a mixture of black phenolic powder and black epoxy powder in a QATM Opal 460. Once hot-mounted, the samples were ground down and polished in a QATM Saphir 530. The planes cut across are shown in Figure 39.

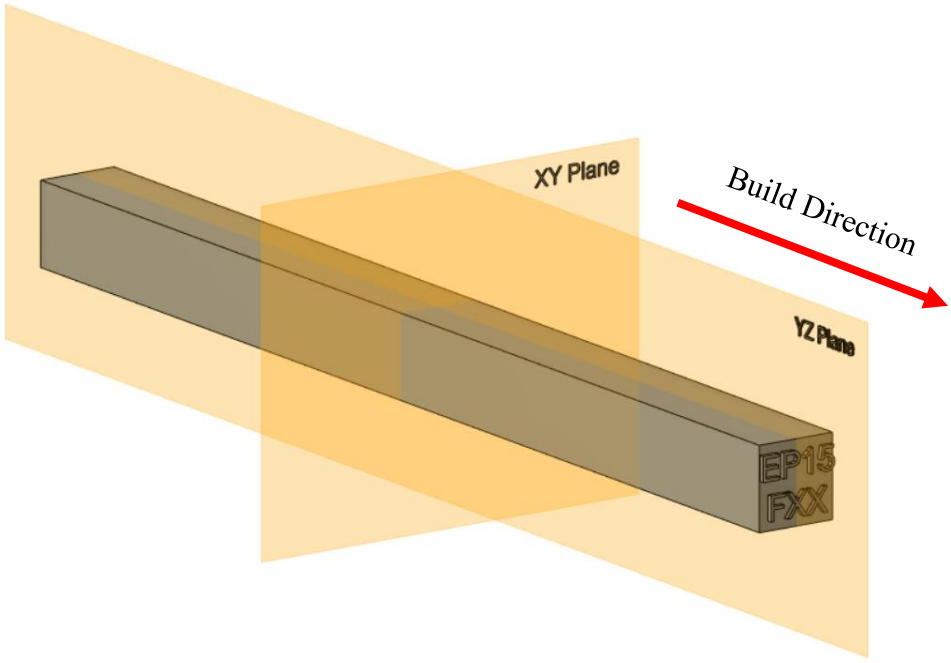

Figure 39 Illustration of the XY plane and YZ plane used to take photographs of the samples. Illustration was made using Fusion 360

3.7 POROSITY CHARACTERIZATION

The mounted samples were photographed using an optical microscope by Keyence VHX-7000 (Illinois, USA). The photographs were then processed using ImageJ, the National Institutes of Health image processing software, to characterize the number of pores, pore size, and pore circularity.

The number of pores is calculated by adjusting the image's hue, saturation, and brightness. The adjustments created significant contrasts between pores and the Ti64, which ImageJ can quickly identify. All pores within a cross-section could be automatically counted, and the average defect size for each process parameter was later found using Excel. Porosity was also separated into three groups: total porosity, bulk porosity, and near-edge porosity, where the near-edge porosity is defined as pores located within 300μm of the surface.

The circularity of the pores was found using ImageJ's circularity feature seen in Equation 1. Results from the circularity measurements were reported as a ratio between 0 and 1, where one is defined as entirely circular. Circularity averages were then taken for each pore and reported as average circularity for every process parameter.

$$Circularity = \frac{4\pi\ (Area)}{permeter^2}$$

Equation 8 Circularity of a geometry defined by ImageJ.

3.6 HARDNESS TESTING

The ZY cross sections of the specimens underwent micro-hardness assessments using QATM's CHD Master+ Micro Hardness Tester.

3.7 Fatigue Testing

4-point bending flexural fatigue testing was conducted using an MTS Landmark (Minnesota, USA), a servo-hydraulic tension-compression testing apparatus. The MTS Landmark was fitted with a 100kN loadcell and a stainless-steel articulating 4-point bending flexure fixture provided by Material Testing Technologies (Illinois, USA). A completed assembly of the MTS Landmark with the MTT 4- point bending fixture can be seen in Figure 40.

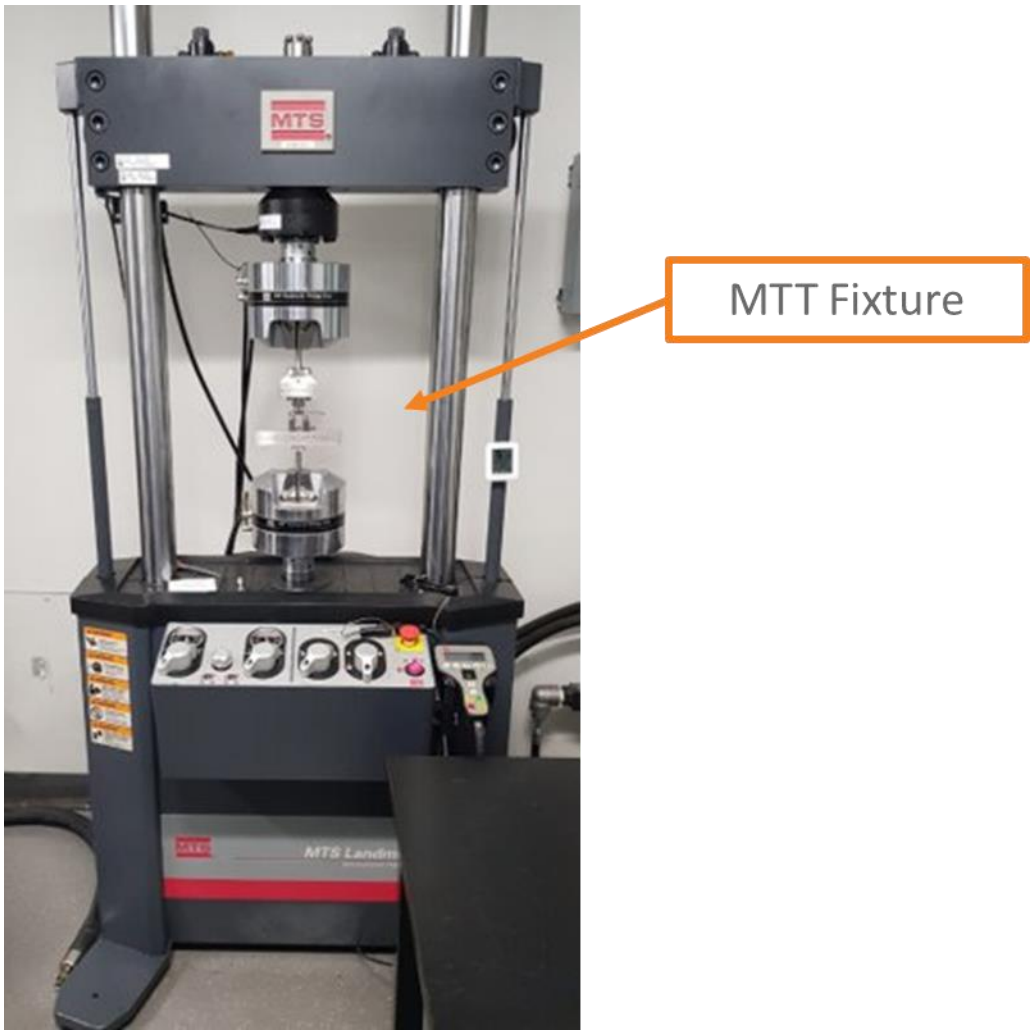

Figure 40 MTS 4 Point Bending Testing apparatus

Six of the nine printed samples were randomly selected for 4-point bending fatigue testing for 60 tests. The testing conditions were conducted at 10 Hz with an upper support distance of 10 mm and a lower support distance of 30 mm. The yield stress (Sy) of the Ti64 was 1050 MPa, and five stress levels were chosen to evaluate the fatigue life. Samples were evaluated until fracture or until $7*10^6$ cycles had been reached. Table 5 are the testing parameters defined for 4-point bending testing. A total of two tests were conducted per sample at two different stress levels. An illustration of the testing breakdown is shown in Figure 41.

Table 5 Testing parameters used for 4-point bending fatigue testing.

Testing Parameters	
Testing frequency	10 Hz
Maximum cycles evaluated	$7 * 10^6$ cycles
Stress levels evaluated	[30%, 40%, 50%, 80%,90%] of S_y
Inner support distance	10 mm
Outer support distance	30 mm

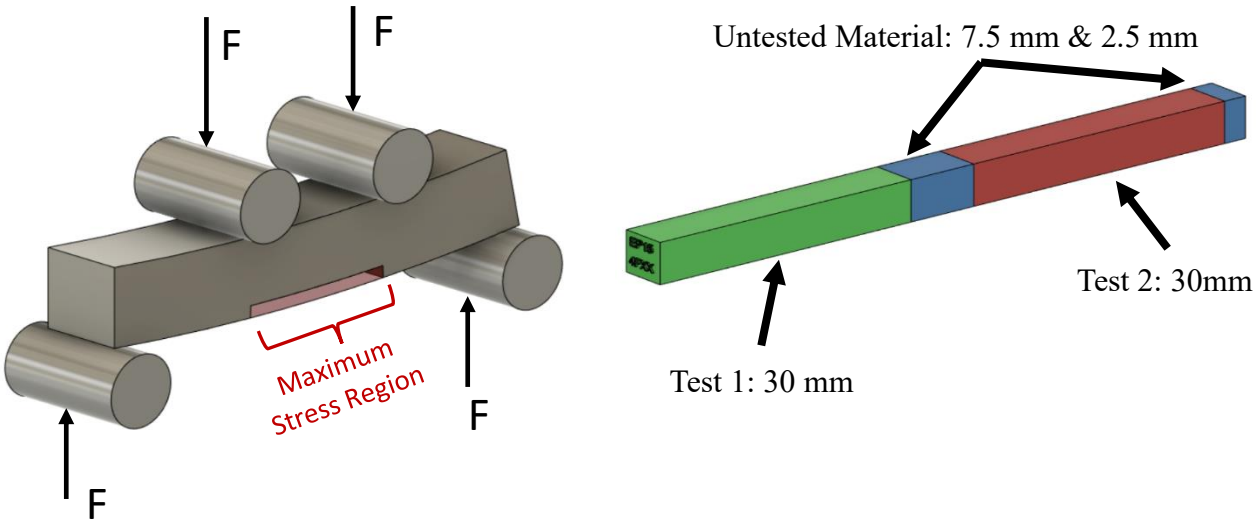

Figure 41 CAD (Computer aided design) illustration of the 4-point bending testing with the maximum stress region highlighted (left) and a testing breakdown of ta sample.

Testing was standardized using the Test Suite Multipurpose Elite software by MTS. The software allowed for the automatic calculation of the desired maximum stress on the sample determined by the maximum flexural fatigue stress (Equation 9). In addition, the software could compensate for slight differences in the specimen dimensions to ensure the proper stress level was evaluated.

$$\sigma = \frac{Mc}{I} = \frac{Flc}{I}$$

Equation 9 Maximum flexural stress on a specimen where M is maximum moment on the sample, c is the half average height of the sample, and I is the, I is the moment of inertia of the square cross section. F is the maximum force exerted on the sample from one support

Chapter 4: Results and Discussion

4.1 Analysis of Porosity

The number of pores and pore geometry per process parameter varied greatly. As seen in Table 6 and associated Figure 42 , the Keyhole exposure set saw the most significant number of pores at 3861 measured for every cross-section, which was ~29.8% higher than the exposure set with the 2nd most significant number of pores ,LoF. In addition, the keyhole exposure set also saw the highest porosity and highest circularity between defects.

The exposure set for the Keyhole parameters induced the expected defects and was compared to other process parameters. Figure 43 shows the difference between the defect morphology of Lof and Keyhole exposure sets. While the defects within the sample did not show any evidence of affecting the fatigue life, it is essential to note that the different exposure sets did affect the internal characteristics of the components.

Regarding defect location, EOS Nominal saw the highest pore concentration in the near edge region (within 300 μm from the surface). The presence of high porosity suggested a potential weakness along the surface that may have a negative impact on fatigue life. Furthermore, relationship fatigue life, porosity location, and surface integrity may exist.

The average defect size, Process Window exposure set, was also found to have the most prominent pores among all exposure sets studied. Such porosity must lie within the contouring strategy as the bulk region showed very low porosity (.106% porosity), especially when compared to Lof and Keyholing. However, the pore size did not significantly affect the overall fatigue performance. Photographs of near-edge porosity per process parameter are shown in Figure 44.

Table 6 Breakdown of porosity characterization by amount, circularity, and location.

Porosity by Process Parameter					
Process Parameter	Total Number of Pores	Average Pore Circularity	Percentage of Porosity	Percentage of Near Edge Porosity	Percentage of Bulk Porosity
Keyhole	3861	0.76 ± 0.04	.385± .004%	38%	62%
Lack of Fusion	2708	0.58 ± 0.05	.215± .046%	68.1%	31.9%
Process Window	1363	0.63 ± 0.06	.106± .012%	98.8%	1.2%
EOS Nominal	231	0.66 ± 0.06	.008± .004%	10.5%	89.5%
EOS Nominal Improved	143	0.57 ± 0.05	.017± .012%	98.8%	1.2%

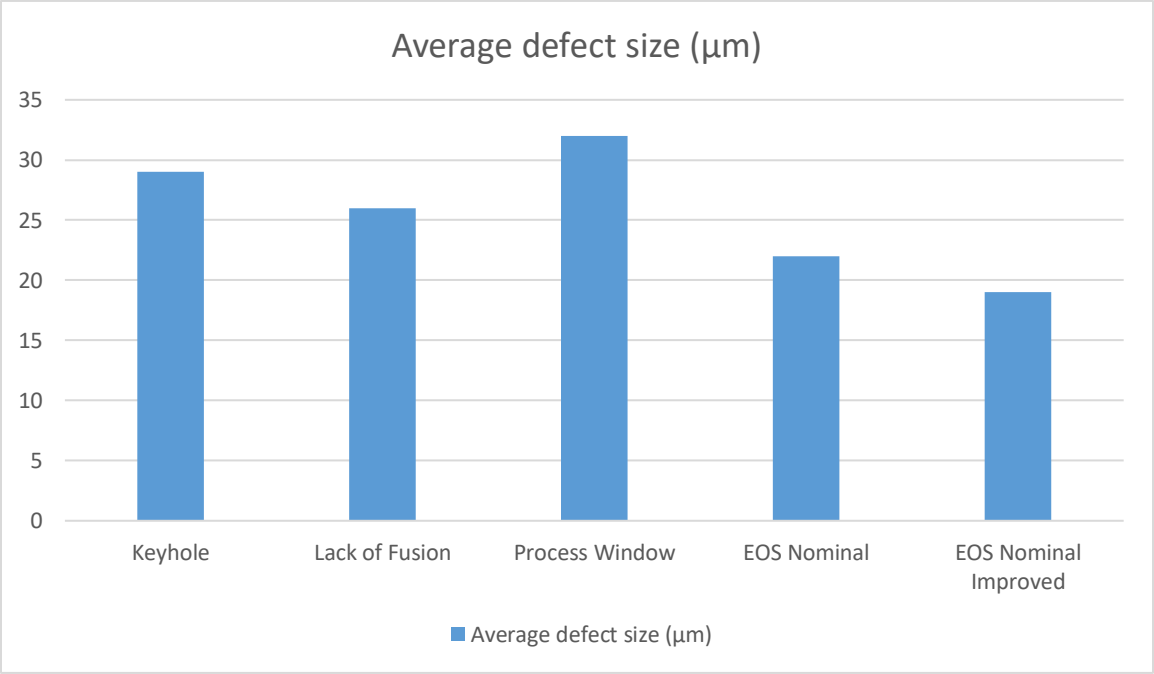

Figure 42 Average defect size (by equivalent diameter) per process parameter,

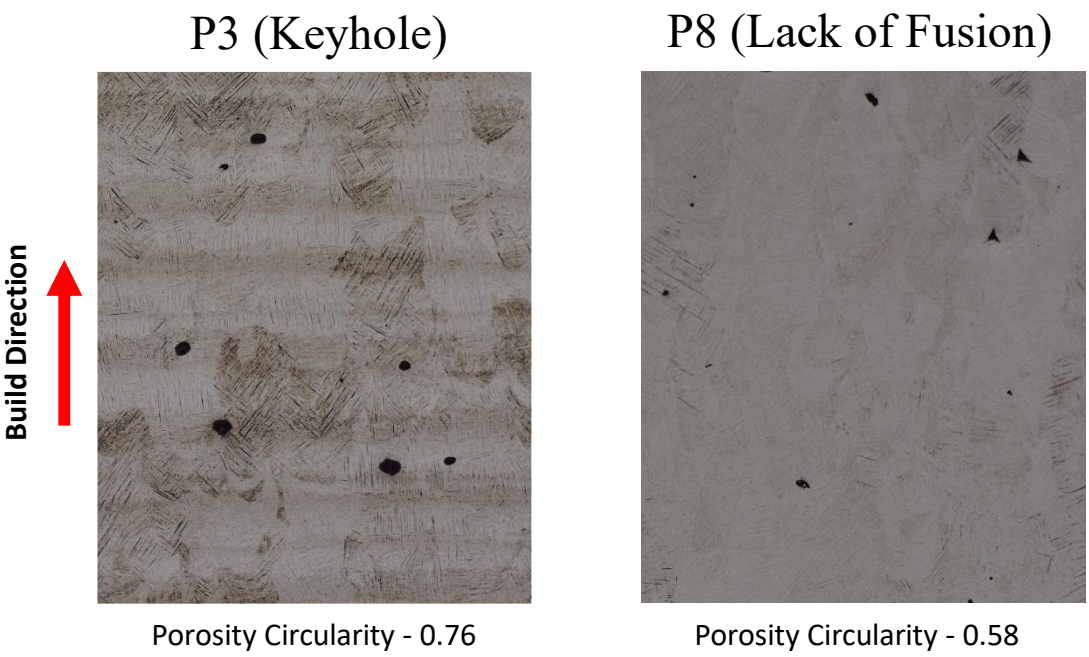

Figure 43 Side-by-side comparison between

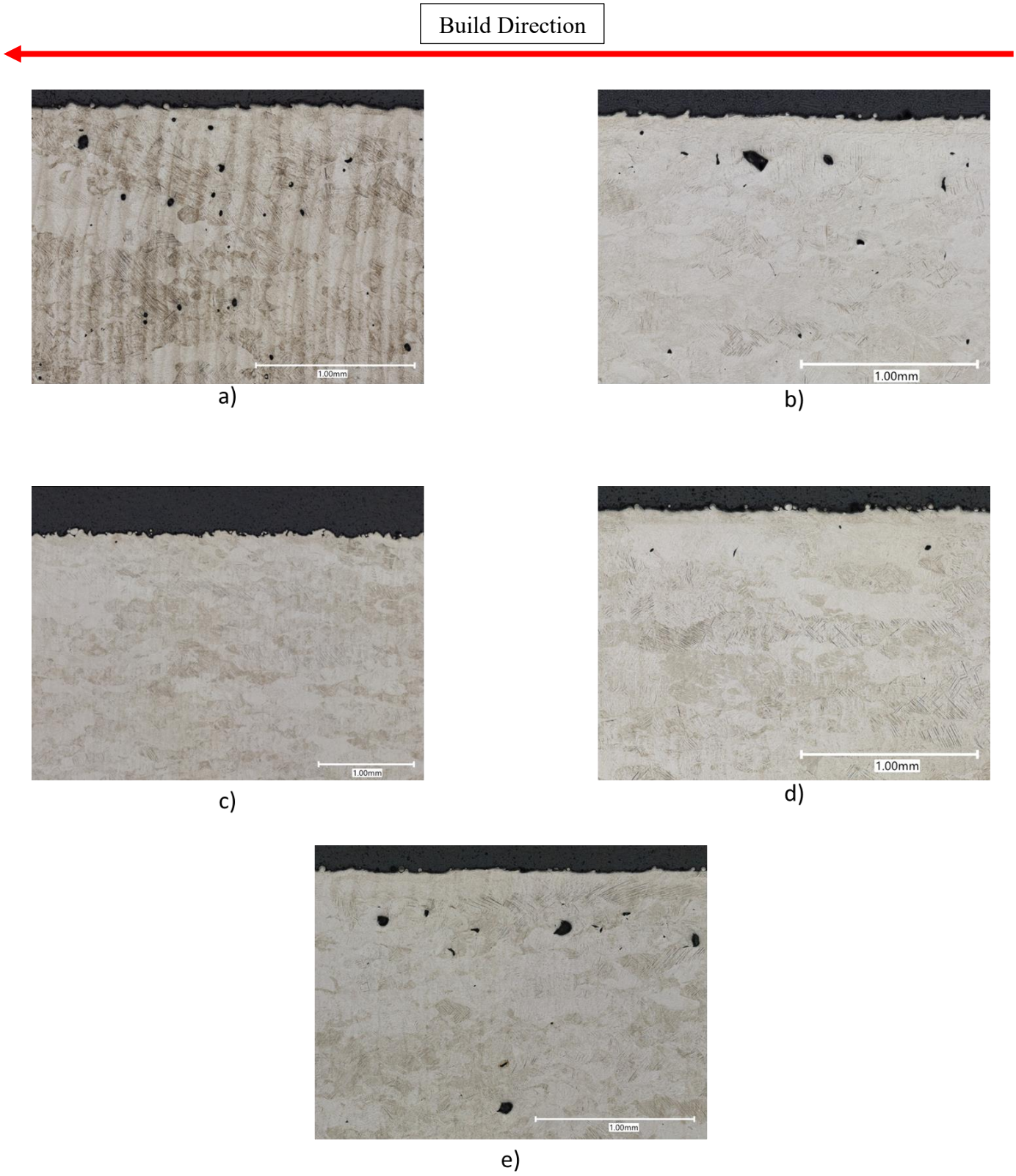

Figure 44 Digital images of micrographs showing near edge porosity within 300 microns of the surface at 50x magnification . a)Keyhole process parameter b) LoF process parameter c)NOM process parameter d) NOM IM process Parameter e) PW process parameter.

4.2 Surface Roughness Analysis

The average surface roughness from NOM to NOM IM shows a decrease in value where the average surface roughness of NOM is Sa = 15µm, whereas NOM IM surface roughness was decreased by more than half with an average surface roughness of Sa = 7µm. As seen in Figure 45 there is also a visual difference between the two surfaces where NOM has significantly more partially sintered powdered Ti64 is located on the surface than NOM IM. In addition, NOM appeared to have the roughest between other exposure sets.

Visual inspection of the as-built surfaces (Figure 46) at high magnification shows micro-cracks on the surface that may act as stress concentrators. The effect of these micro-cracks can decrease the ability of a component to withstand cyclical load, initiating early crack growth. Fractography analysis of the samples suggested cracks initiated from the surface rather than defects in the samples tested at 40% of their yield strength. This trend was also seen in samples tested at 80% and 90%, where near-edge internal defects did not seem to be initiation sites of cracks.

Table 7 lists all surface roughness values categorized by the measurements taken. NOM reported the highest S_a values ~15 µm with a significantly higher S_v = 121.9 µm. The presence of rough surfaces predicts poor fatigue despite having high density (Table 6).

Table 7 Table depicting the average surface roughness, maximum valley depth (S_v), and average valley depth (S_{vk})

Surface Roughness by Process Parameter			
Process Parameter	S_a (µm)	S_v (µm)	S_{vk} (µm)
EOS Nominal	15±1	121.9	16.8
EOS Nominal Improved	7±1	91.8	8.6
Keyhole	12±2	78.19	14.66
Lack of Fusion	8±1	47.8	8.17
Process Window	9±2	63.49	10.62

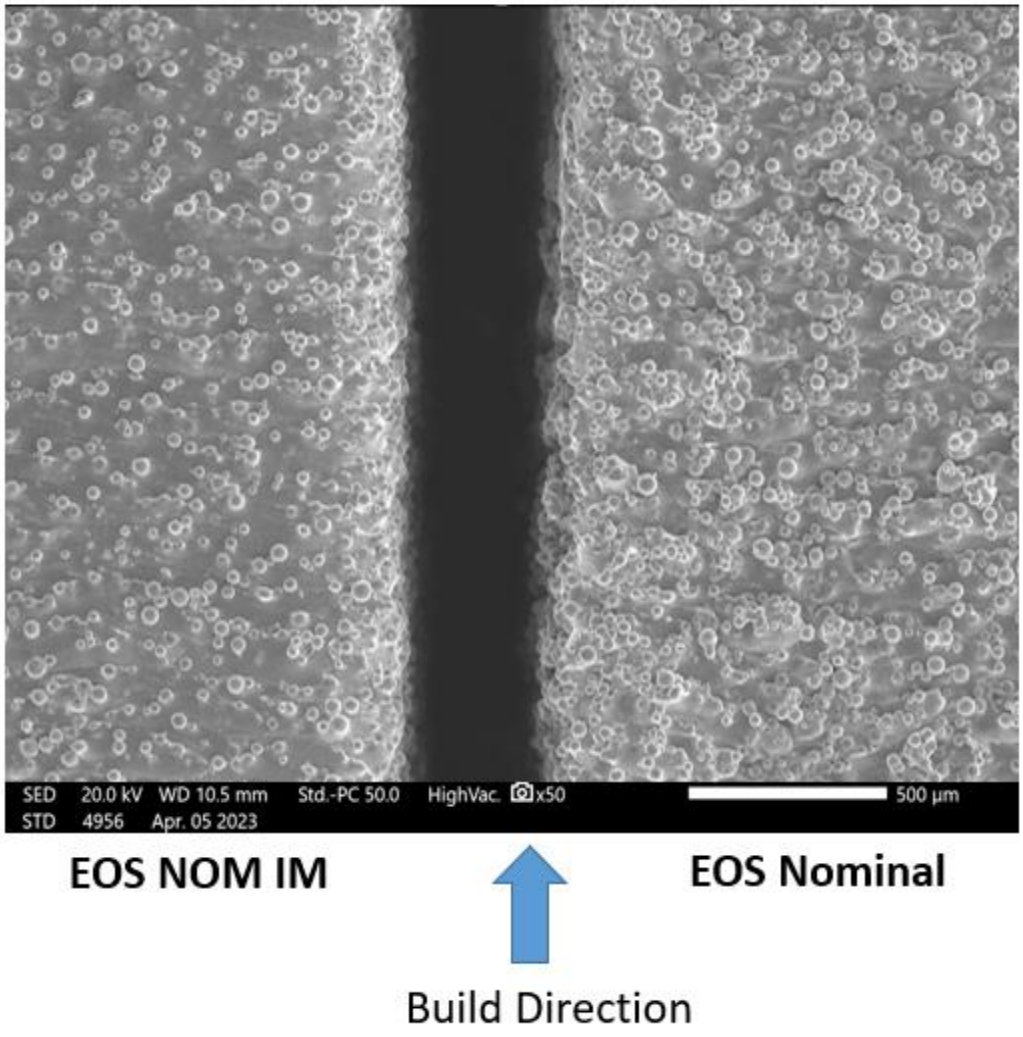

Figure 45 SEM surface comparison of EOS Nominal Improved and EOS Nominal at 50x

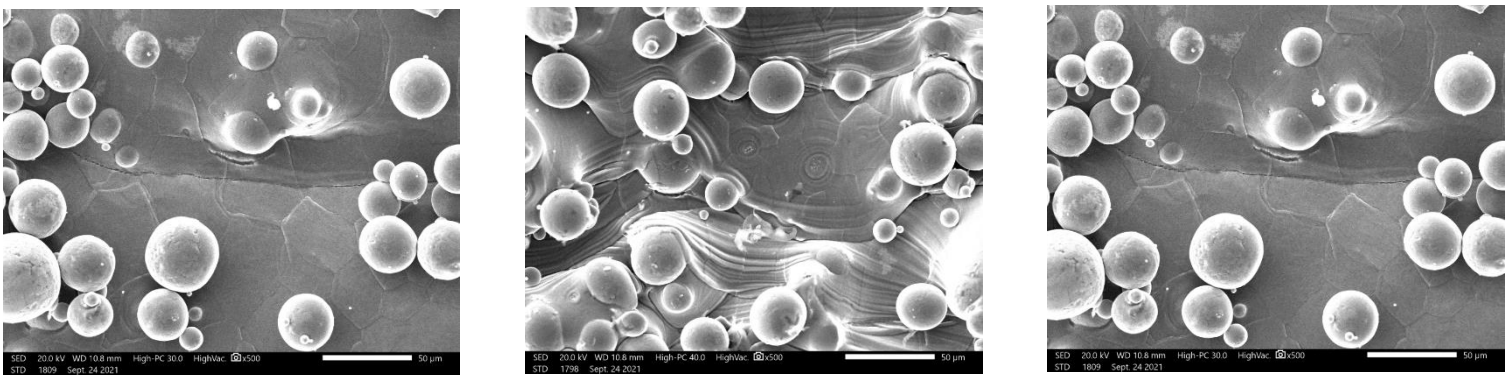

Keyhole NOM NOM IM

Figure 46 Surface comparison of all exposure sets at 500x magnification.

4.3 HARDNESS TESTING & MICROSTRUCTURE

For all process parameters, a martensitic α' was formed. Ti64 is a two-phase α -β, where the high temperatures form a body-centered cubic structure, and the lower temperatures form a hexagonal close-packed structure. However, the rapid heating and cooling induced for LPBF do not allow the Ti64 to transform into any equilibrium phase making a martensitic-like microstructure entirely. The highly irregular microstructure makes characterization extremely difficult.

Microhardness results in comparable results slightly higher than seen in literature such as Kaushik et al.[163]. Given that there is a 2.9% difference between the greatest and least microhardness values tested, exposure sets likely do not significantly affect the microhardness of as-built components. Shown in Figure 47 and Table 8 are microstructure images and hardness values, respectively.

Table 8 Microhardness values categorized by process parameter.

Microhardness Values	
Process Parameter	Hardness Value (HV)
Keyhole	407 ± 10
LoF	419 ± 8
PW	412 ± 3
NOM	413 ± 6
NOM IM	419 ± 3

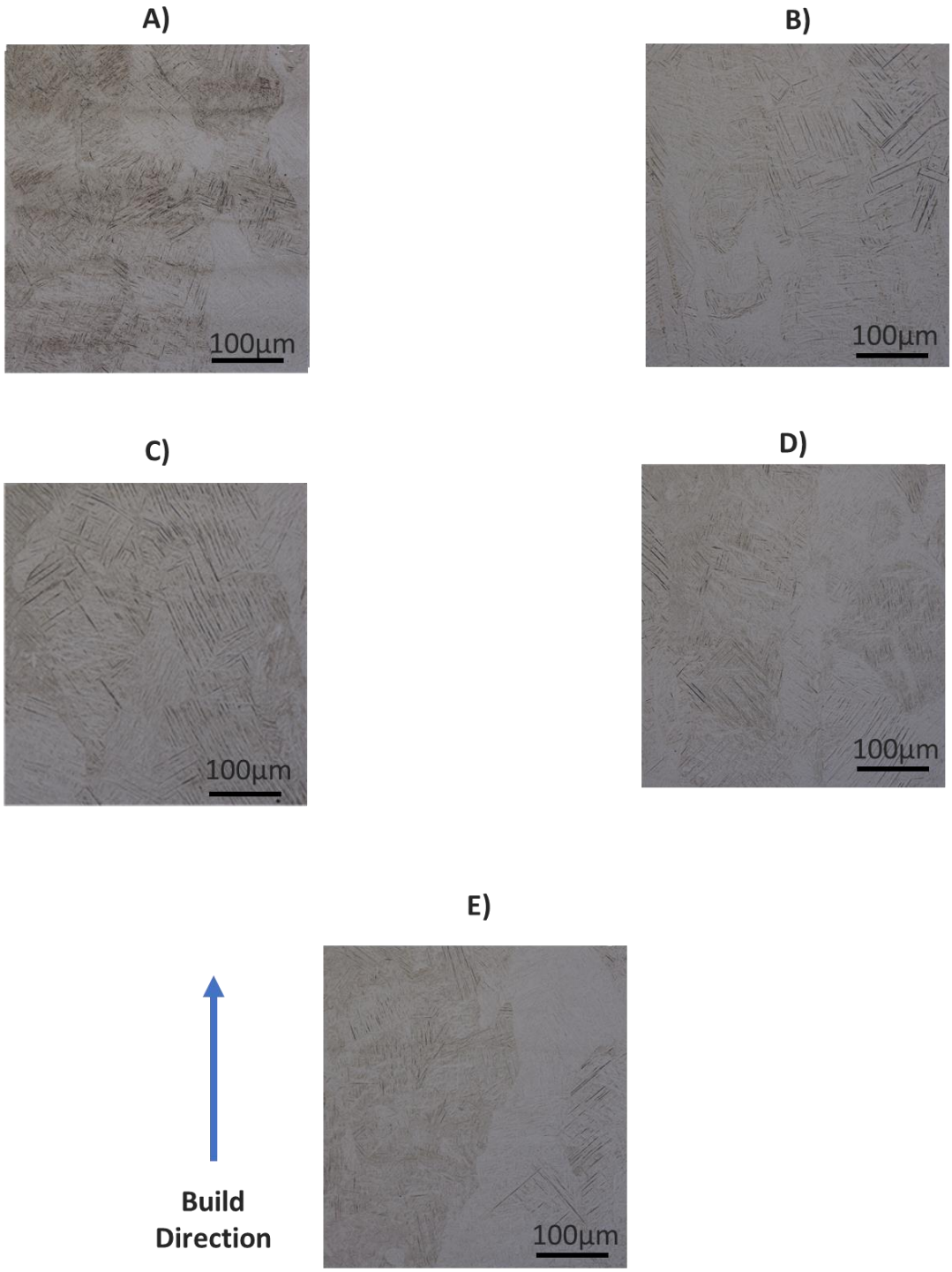

Figure 47 Digital images of process parameters highlighting their microstructure. a)Keyhole process parameter b) LoF process parameter c)NOM process parameter d) NOM IM process Parameter e) PW process parameter.

4.4 FATIGUE LIFE ANALYSIS

The results from fatigue testing are presented graphically, comparing the examined stress level versus the number of cycles until failure (S-N Diagram) shown in Figure 48. The samples were grouped by process parameters using lightly colored groups to distinguish fatigue behavior per stress level better. Using Basquin's Law, a curve was generated per process per process parameter (Figure 49) using the average number of cycles per stress level. In addition, a corresponding table, Table 9, shows the average error between the fit and the test data.

The Keyhole Process parameter averaged $5*10^3$-$7*10^3$ cycles at 90% of the yield strength (945 MPa) and 10^5-$30*10^5$ cycles at 30% of the yield strength, the worst-performing process parameter among all exposure sets. The short fatigue life results from high surface roughness in the keyhole process parameter; however, internal defects did not shorten fatigue life.

Cross sections of LoF contained many defects (Table 6) but had a comparable fatigue life to NOM. At 90% of the yield strength, LoF had a fatigue life between $7*10^3$-10^4 cycles which outperformed the NOM fatigue life (~$7*10^3$ cycles). At 30 % of the yield strength, it is seen that fractured samples of NOM IM had similar fatigue life to LoF as well. The higher fatigue lives also reinforce the idea that surface quality is the main factor of the fatigue life of as-built surfaces.

Between NOM and NOM IM, it is apparent that Infill process parameters do not affect the fatigue life of as-built surfaces as much as contouring parameters. The extra contour (Figure 38) drastically increased the fatigue life of NOM IM. Therefore, evidence suggests that the most significant influence on fatigue life is the integrity of the surface because NOM IM reported a significantly less surface roughness value (Table 7).

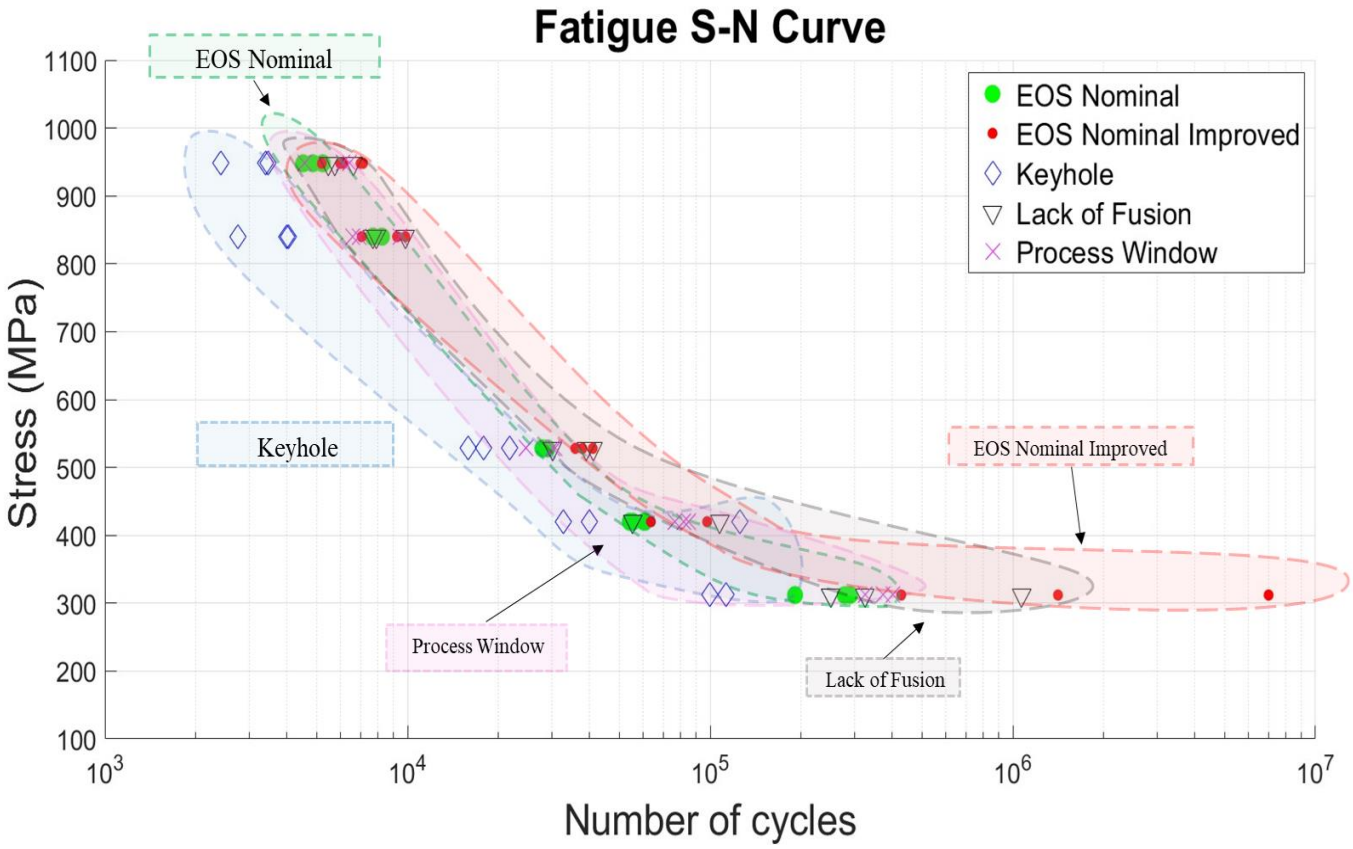

Figure 48 S-N Curve of samples separated by their respective process parameter set.

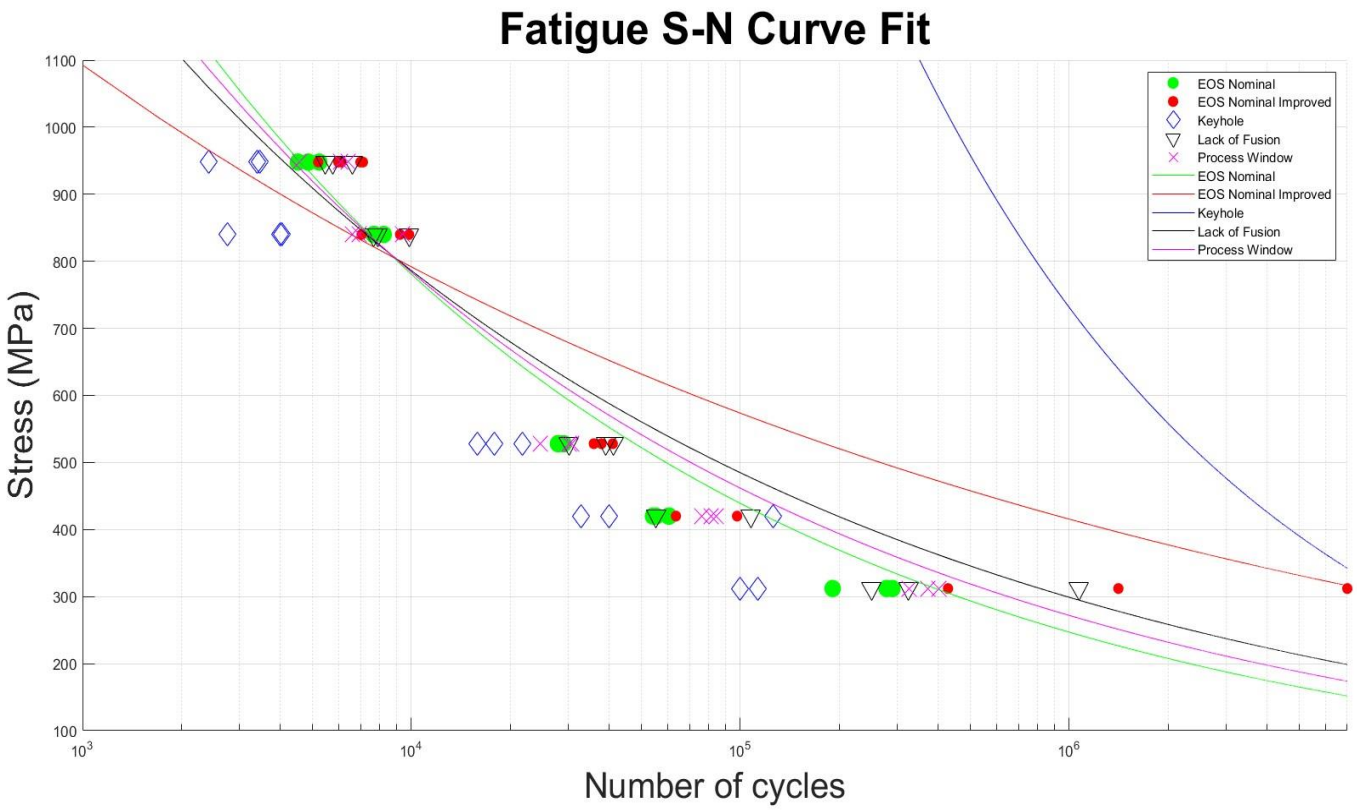

Figure 49 Basquin's law used to fit the fatigue data.

Table 9 Percentage error of Basquin fit to the raw data.

Percentage Error By Process Parameter					
Stress level Tested	NOM	NOM IM	Keyhole	Lof	PW
312	9%	17%	449%	11%	8%
420	17%	43%	387%	23%	13%
528	12%	26%	539%	15%	15%
840	-3%	-3%	664%	-2%	-2%
948	-3%	-10%	618%	-6%	-7%
Average % Error	6%	15%	532%	8%	5%

4.5 Fracture Analysis

Fractured surfaces analyzed showed initiation sites at the surface amongst all stress levels for the as-built surfaces. The primary reason for fracturing was heavily influenced by the surface roughness of the components, regardless of the presence of near-edge defects. While the rate of crack propagation was not measured, it is seen that the propagation region and overload regions are significantly different for each stress level. A larger overload region was seen in samples with higher stress levels, and the opposite was seen in the lower stress levels. Figure 50 compares the Keyhole and PW fractured surfaces at 90% and 30% of the yield stress. For the keyhole, 91% of the fractured surface was classified as the overload region at 90% of yield stress, and at 30% of yield stress, the overload region was 69% of the fractured surface. At 90% of the yield stress for PW, 81% of the fracture surface was considered the overload region, and that region was reduced to 60% of the fracture surface at 30% of the yield stress.

SEM images were taken of the fractured samples at 40% at each process parameter at 18x magnification and at 70x magnification to identify the initiation site, and it is evident that the surface was the primary source of failure for all process parameters from surface initiation. PW, Keyhole, LoF, and NOM IM in Figure 52 all show apparent defects near the surface; the defects did not seem to be initiation sites. In addition, NOM also did show signs of surface initiation and did not show any defects near the surface. At higher magnification levels measured 1 mm above the initiation site, striation marks are typical to the loading surface. The presence of striations becomes prominent at higher stress levels seen in Figure 51.

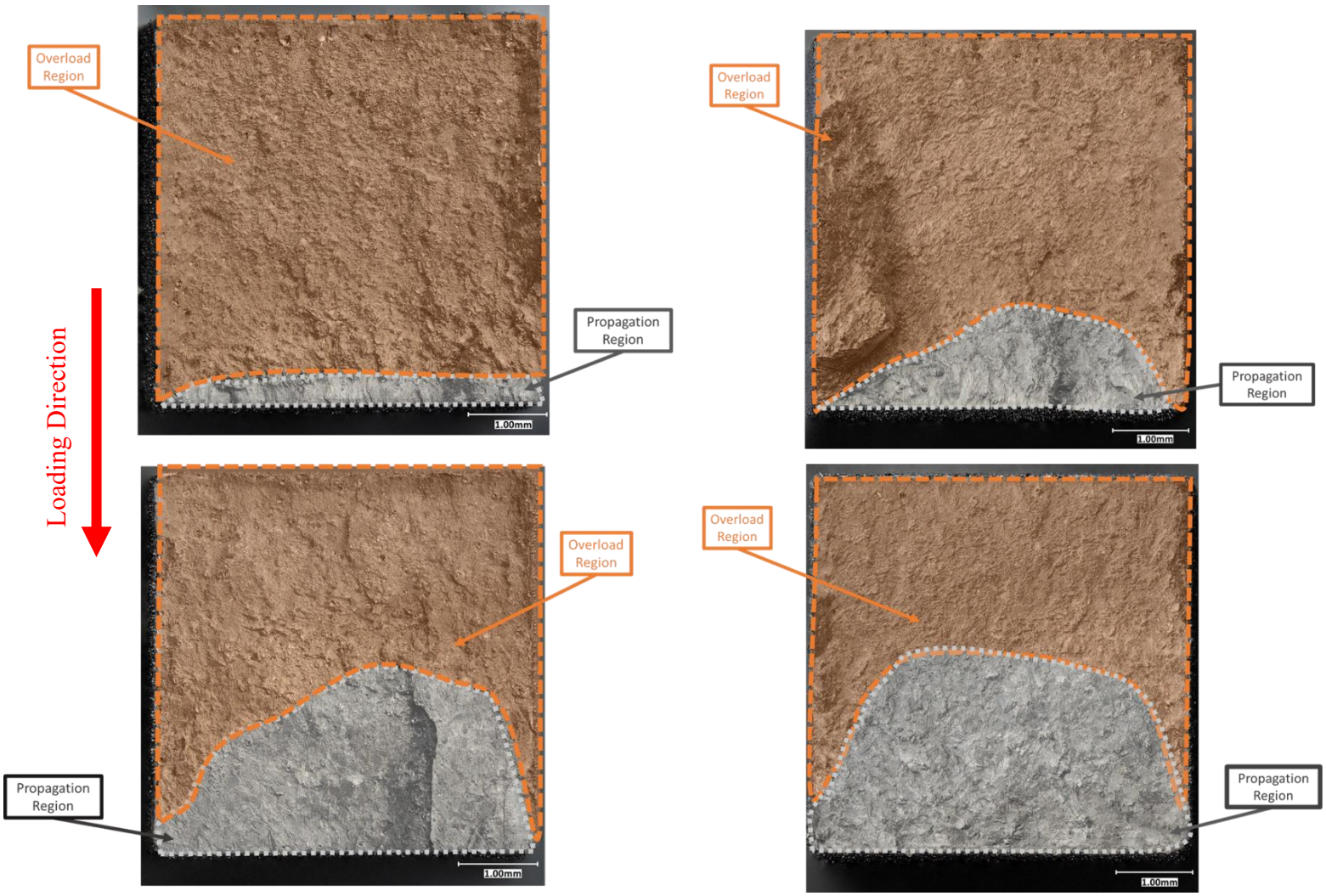

Figure 50 fracture surface of Keyhole(left) and Process Window at 30% and 90% of yield stress

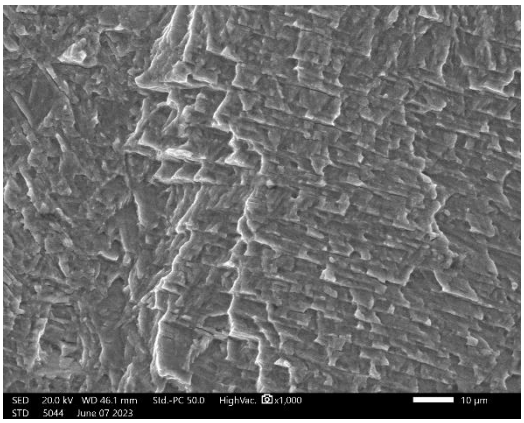

a)

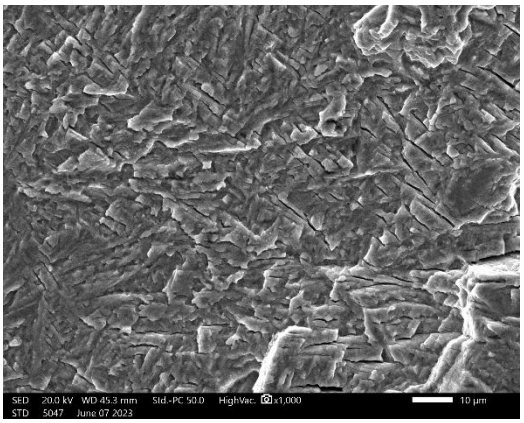

b)

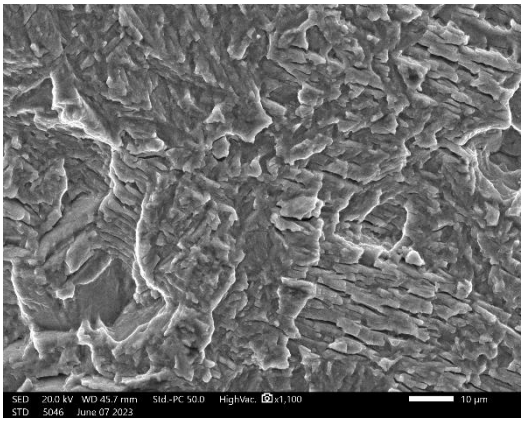

c)

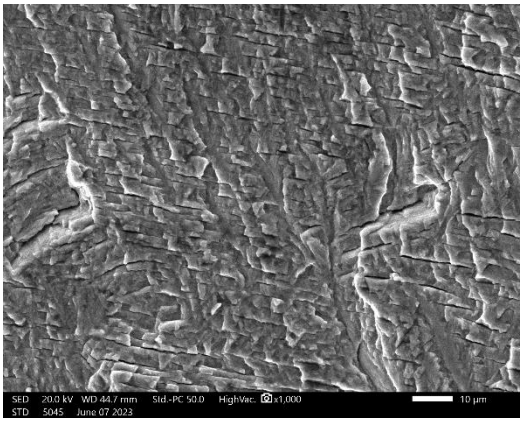

d)

Loading Direction

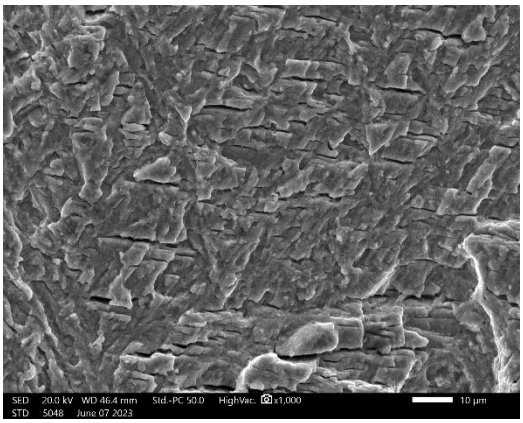

e)

Figure 51 Striation marks photographed 1mm above the fractured surface at 1000x magnification. a)Keyhole process parameter b) LoF process parameter c)NOM process parameter d) NOM IM process Parameter e) PW process parameter.

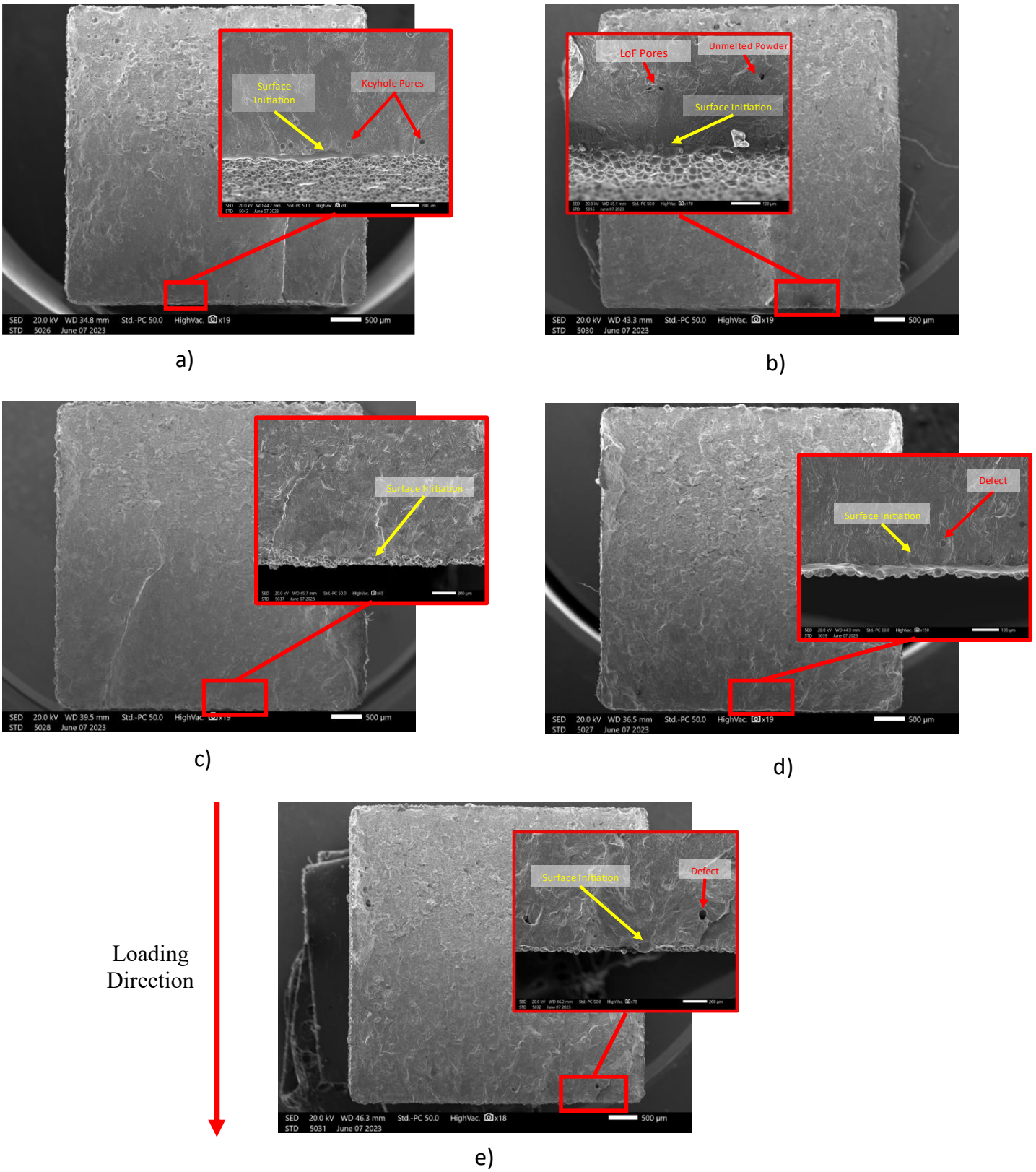

Figure 52 SEM images of fractured surfaces at 40% of the yield stress. a)Keyhole process parameter b) LoF process parameter c)NOM process parameter d) NOM IM process Parameter e) PW process parameter.

Chapter 5: Conclusions

The most significant observation was that all samples examined showed signs of surface initiation that did not propagate through defects. In addition, defects did not seem to be stress concentrations for crack initiation, nor did any cracks significantly propagate through defects located within 300 microns of the as-built surface. This indicates that the process parameters heavily influenced fatigue life, and scanning strategy methods can improve the fatigue life of as-built components.

A significant result of the study was that the same laser power and scanning speed between NOM and NOM IM had different surface qualities by remelting the outer contour. Decreasing the roughness value of NOM from Sa=15 μm to Sa=7 μm with NOM IM leads to fatigue lives as high as $7*10^6$ cycles. Statistical fits of the curve did show similar behavior for all process parameters. They did indicate what was shown by visually analyzing the data, as seen in Figure 48, but the fit for Keyholing specimens did not correlate with the fatigue behavior. This further indicates that surface quality heavily impacts fatigue performance. While this work does not evaluate the relationship between surface post-processed components and internal defects, it can be concluded that surface roughness is the main factor of fatigue failure for stress-relieved as-built components.

References

[1] "Additive manufacturing — General principles — Fundamentals and Vocabulary," American Society for Testing and Materials, ASTM 52900-21, Mar. 2023. Accessed: Jan. 24, 2023. [Online]. Available: https://compass.astm.org/document/?contentCode=ASTM%7CF3177-21%7Cen-US&proxycl=https%3A%2F%2Fsecure.astm.org&fromLogin=true

[2] T. Pereira, J. V. Kennedy, and J. Potgieter, "A comparison of traditional manufacturing vs additive manufacturing, the best method for the job," *Procedia Manuf.*, vol. 30, pp. 11–18, Jan. 2019, doi: 10.1016/j.promfg.2019.02.003.

[3] M. Attaran, "The rise of 3-D printing: The advantages of additive manufacturing over traditional manufacturing," *Bus. Horiz.*, vol. 60, no. 5, pp. 677–688, Sep. 2017, doi: 10.1016/j.bushor.2017.05.011.

[4] D. Dev Singh, T. Mahender, and A. Raji Reddy, "Powder bed fusion process: A brief review," *Mater. Today Proc.*, vol. 46, pp. 350–355, Jan. 2021, doi: 10.1016/j.matpr.2020.08.415.

[5] E. Malekipour and H. El-Mounayri, "Scanning Strategies in the PBF Process: A Critical Review," presented at the ASME 2020 International Mechanical Engineering Congress and Exposition, American Society of Mechanical Engineers Digital Collection, Feb. 2021. doi: 10.1115/IMECE2020-24589.

[6] J. P. Oliveira, A. D. LaLonde, and J. Ma, "Processing parameters in laser powder bed fusion metal additive manufacturing," *Mater. Des.*, vol. 193, p. 108762, Aug. 2020, doi: 10.1016/j.matdes.2020.108762.

[7] A. T. Sutton, C. S. Kriewall, M. C. Leu, and J. W. Newkirk, “Powder characterisation techniques and effects of powder characteristics on part properties in powder-bed fusion processes,” *Virtual Phys. Prototyp.*, vol. 12, no. 1, pp. 3–29, Jan. 2017, doi: 10.1080/17452759.2016.1250605.

[8] S. Cao, Y. Zou, C. V. S. Lim, and X. Wu, “Review of laser powder bed fusion (LPBF) fabricated Ti-6Al-4V: process, post-process treatment, microstructure, and property,” *Light Adv. Manuf.*, vol. 2, no. 3, pp. 313–332, Sep. 2021, doi: 10.37188/lam.2021.020.

[9] A. Vafadar, F. Guzzomi, A. Rassau, and K. Hayward, “Advances in Metal Additive Manufacturing: A Review of Common Processes, Industrial Applications, and Current Challenges,” *Appl. Sci.*, vol. 11, no. 3, Art. no. 3, Jan. 2021, doi: 10.3390/app11031213.

[10] C. Fleißner-Rieger, T. Pfeifer, C. Turk, and H. Clemens, “Optimization of the Post-Process Heat Treatment Strategy for a Near-α Titanium Base Alloy Produced by Laser Powder Bed Fusion,” *Materials*, vol. 15, no. 3, p. 1032, Jan. 2022, doi: 10.3390/ma15031032.

[11] A. Bagheri and J. Jin, “Photopolymerization in 3D Printing,” *ACS Appl. Polym. Mater.*, vol. 1, no. 4, pp. 593–611, Apr. 2019, doi: 10.1021/acsapm.8b00165.

[12] “VAT Photopolymerisation | Additive Manufacturing Research Group | Loughborough University.” https://www.lboro.ac.uk/research/amrg/about/the7categoriesofadditivemanufacturing/vatphotopolymerisation/ (accessed Apr. 09, 2023).

[13] A. Bucciarelli *et al.*, “VAT photopolymerization 3D printing optimization of high aspect ratio structures for additive manufacturing of chips towards biomedical applications,” *Addit. Manuf.*, vol. 60, p. 103200, Dec. 2022, doi: 10.1016/j.addma.2022.103200.

[14] A. Al Rashid, W. Ahmed, M. Y. Khalid, and M. Koç, "Vat photopolymerization of polymers and polymer composites: Processes and applications," *Addit. Manuf.*, vol. 47, p. 102279, Nov. 2021, doi: 10.1016/j.addma.2021.102279.

[15] M. Pagac *et al.*, "A Review of Vat Photopolymerization Technology: Materials, Applications, Challenges, and Future Trends of 3D Printing," *Polymers*, vol. 13, no. 4, Art. no. 4, Jan. 2021, doi: 10.3390/polym13040598.

[16] "Clear Resin," *Formlabs*. https://formlabs.com/store/materials/clear-resin/ (accessed Apr. 09, 2023).

[17] "Buy Dental LT Clear Resin," *Formlabs*. https://formlabs.com/store/materials/dental-lt-clear-resin/ (accessed Apr. 09, 2023).

[18] "Grey Resin," *Formlabs*. https://formlabs.com/store/materials/grey-resin/ (accessed Apr. 10, 2023).

[19] "Black Resin," *Formlabs*. https://formlabs.com/store/materials/grey-resin/ (accessed Apr. 10, 2023).

[20] "Durable Resin," *Formlabs*. https://formlabs.com/store/materials/durable-resin/ (accessed Apr. 10, 2023).

[21] "Tough 2000 Resin," *Formlabs*. https://formlabs.com/store/materials/tough-2000-resin/ (accessed Apr. 10, 2023).

[22] A. M. E. Arefin, N. R. Khatri, N. Kulkarni, and P. F. Egan, "Polymer 3D Printing Review: Materials, Process, and Design Strategies for Medical Applications," *Polymers*, vol. 13, no. 9, p. 1499, May 2021, doi: 10.3390/polym13091499.

[23] N. Shahrubudin, T. C. Lee, and R. Ramlan, “An Overview on 3D Printing Technology: Technological, Materials, and Applications,” *Procedia Manuf.*, vol. 35, pp. 1286–1296, Jan. 2019, doi: 10.1016/j.promfg.2019.06.089.

[24] D. Godec *et al.*, “Introduction to Additive Manufacturing,” in *A Guide to Additive Manufacturing*, D. Godec, J. Gonzalez-Gutierrez, A. Nordin, E. Pei, and J. Ureña Alcázar, Eds., in Springer Tracts in Additive Manufacturing. Cham: Springer International Publishing, 2022, pp. 1–44. doi: 10.1007/978-3-031-05863-9_1.

[25] J. Huang, Q. Qin, and J. Wang, “A Review of Stereolithography: Processes and Systems,” *Processes*, vol. 8, no. 9, Art. no. 9, Sep. 2020, doi: 10.3390/pr8091138.

[26] H. Quan, T. Zhang, H. Xu, S. Luo, J. Nie, and X. Zhu, “Photo-curing 3D printing technique and its challenges,” *Bioact. Mater.*, vol. 5, no. 1, pp. 110–115, Jan. 2020, doi: 10.1016/j.bioactmat.2019.12.003.

[27] J. R. Tumbleston *et al.*, “Continuous liquid interface production of 3D objects,” *Science*, vol. 347, no. 6228, pp. 1349–1352, Mar. 2015, doi: 10.1126/science.aaa2397.

[28] A. R. Johnson *et al.*, “Single-Step Fabrication of Computationally Designed Microneedles by Continuous Liquid Interface Production,” *PLOS ONE*, vol. 11, no. 9, p. e0162518, Sep. 2016, doi: 10.1371/journal.pone.0162518.

[29] J. Stromberg, “Watch: This new type of 3D printing was inspired by Terminator 2,” *Vox*, Mar. 16, 2015. https://www.vox.com/2015/3/16/8227627/3d-printing-liquid-continuous (accessed Apr. 11, 2023).

[30] “Sheet Lamination | Siemens Software,” *Siemens Digital Industries Software*. https://www.plm.automation.siemens.com/global/en/our-story/glossary/sheet-lamination/55512 (accessed Apr. 12, 2023).

[31] “Sheet Lamination | Additive Manufacturing Research Group | Loughborough University.” https://www.lboro.ac.uk/research/amrg/about/the7categoriesofadditivemanufacturing/sheetlamination/ (accessed Apr. 12, 2023).

[32] N. T. Aboulkhair, F. Bosio, N. Gilani, C. Phutela, R. J. M. Hague, and C. J. Tuck, “Chapter Six - Additive manufacturing processes for metals,” in *Quality Analysis of Additively Manufactured Metals*, J. Kadkhodapour, S. Schmauder, and F. Sajadi, Eds., Elsevier, 2023, pp. 201–258. doi: 10.1016/B978-0-323-88664-2.00016-6.

[33] I. Gibson, D. Rosen, and B. Stucker, “Sheet Lamination Processes,” in *Additive Manufacturing Technologies: 3D Printing, Rapid Prototyping, and Direct Digital Manufacturing*, I. Gibson, D. Rosen, and B. Stucker, Eds., New York, NY: Springer, 2015, pp. 219–244. doi: 10.1007/978-1-4939-2113-3_9.

[34] F. J. Mercado Rivera and A. J. Rojas Arciniegas, “Additive manufacturing methods: techniques, materials, and closed-loop control applications,” *Int. J. Adv. Manuf. Technol.*, vol. 109, no. 1, pp. 17–31, Jul. 2020, doi: 10.1007/s00170-020-05663-6.

[35] M. Molitch-Hou, “1 - Overview of additive manufacturing process,” in *Additive Manufacturing*, J. Zhang and Y.-G. Jung, Eds., Butterworth-Heinemann, 2018, pp. 1–38. doi: 10.1016/B978-0-12-812155-9.00001-3.

[36] Z. Wang and Y. Yang, “Application of 3D Printing in Implantable Medical Devices,” *BioMed Res. Int.*, vol. 2021, pp. 1–13, Jan. 2021, doi: 10.1155/2021/6653967.

[37] R. J. Friel, “13 - Power ultrasonics for additive manufacturing and consolidating of materials,” in *Power Ultrasonics*, J. A. Gallego-Juárez and K. F. Graff, Eds., Oxford: Woodhead Publishing, 2015, pp. 313–335. doi: 10.1016/B978-1-78242-028-6.00013-2.

[38] M. Casini, “Chapter 8 - Advanced building construction methods,” in *Construction 4.0*, M. Casini, Ed., in Woodhead Publishing Series in Civil and Structural Engineering. Woodhead Publishing, 2022, pp. 405–470. doi: 10.1016/B978-0-12-821797-9.00006-4.

[39] O. Gülcan, K. Günaydın, and A. Tamer, “The State of the Art of Material Jetting—A Critical Review,” *Polymers*, vol. 13, no. 16, p. 2829, Aug. 2021, doi: 10.3390/polym13162829.

[40] R. Udroiu and I. C. Braga, “Polyjet technology applications for rapid tooling,” *MATEC Web Conf.*, vol. 112, p. 03011, 2017, doi: 10.1051/matecconf/201711203011.

[41] “Material Jetting | Additive Manufacturing Research Group | Loughborough University.” https://www.lboro.ac.uk/research/amrg/about/the7categoriesofadditivemanufacturing/materialjetting/ (accessed Apr. 17, 2023).

[42] R. Mendřický, “Accuracy analysis of additive technique for parts manufacturing,” *MM Sci. J.*, vol. 2016, pp. 1502–1508, Nov. 2016, doi: 10.17973/MMSJ.2016_11_2016169.

[43] I. Gibson, D. Rosen, B. Stucker, and M. Khorasani, “Material Jetting,” in *Additive Manufacturing Technologies*, I. Gibson, D. Rosen, B. Stucker, and M. Khorasani, Eds., Cham: Springer International Publishing, 2021, pp. 203–235. doi: 10.1007/978-3-030-56127-7_7.

[44] E. Willems *et al.*, “Additive manufacturing of zirconia ceramics by material jetting,” *J. Eur. Ceram. Soc.*, vol. 41, no. 10, pp. 5292–5306, Aug. 2021, doi: 10.1016/j.jeurceramsoc.2021.04.018.

[45] M. A. Shah, D.-G. Lee, B.-Y. Lee, and S. Hur, “Classifications and Applications of Inkjet Printing Technology: A Review,” *IEEE Access*, vol. 9, pp. 140079–140102, 2021, doi: 10.1109/ACCESS.2021.3119219.

[46] S. Tyagi, A. Yadav, and S. Deshmukh, “Review on mechanical characterization of 3D printed parts created using material jetting process,” *Mater. Today Proc.*, vol. 51, pp. 1012–1016, Jan. 2022, doi: 10.1016/j.matpr.2021.07.073.

[47] A. Elkaseer, K. J. Chen, J. C. Janhsen, O. Refle, V. Hagenmeyer, and S. G. Scholz, “Material jetting for advanced applications: A state-of-the-art review, gaps and future directions,” *Addit. Manuf.*, vol. 60, p. 103270, Dec. 2022, doi: 10.1016/j.addma.2022.103270.

[48] H. Wijshoff, “The dynamics of the piezo inkjet printhead operation,” *Phys. Rep.*, vol. 491, no. 4, pp. 77–177, Jun. 2010, doi: 10.1016/j.physrep.2010.03.003.

[49] Y. Meng, G. Chen, and M. Huang, “Piezoelectric Materials: Properties, Advancements, and Design Strategies for High-Temperature Applications,” *Nanomaterials*, vol. 12, no. 7, p. 1171, Apr. 2022, doi: 10.3390/nano12071171.

[50] “How Does Thermal Inkjet Printing Work? | InkJet, Inc.” https://www.inkjetinc.com/resources/how-does-thermal-inkjet-printing-work-ij (accessed Apr. 16, 2023).

[51] B. Derby, “Inkjet Printing of Functional and Structural Materials: Fluid Property Requirements, Feature Stability, and Resolution,” *Annu. Rev. Mater. Res.*, vol. 40, no. 1, pp. 395–414, 2010, doi: 10.1146/annurev-matsci-070909-104502.

[52] I. Gibson, D. Rosen, and B. Stucker, “Extrusion-Based Systems,” in *Additive Manufacturing Technologies*, New York, NY: Springer New York, 2015, pp. 147–173. doi: 10.1007/978-1-4939-2113-3_6.

[53] P. Szymczyk-Ziółkowska, M. B. Łabowska, J. Detyna, I. Michalak, and P. Gruber, “A review of fabrication polymer scaffolds for biomedical applications using additive

manufacturing techniques," *Biocybern. Biomed. Eng.*, vol. 40, no. 2, pp. 624–638, Apr. 2020, doi: 10.1016/j.bbe.2020.01.015.

[54] B. N. Turner, R. Strong, and S. A. Gold, "A review of melt extrusion additive manufacturing processes: I. Process design and modeling," *Rapid Prototyp. J.*, vol. 20, no. 3, pp. 192–204, Jan. 2014, doi: 10.1108/RPJ-01-2013-0012.

[55] Z. Liu, Q. Lei, and S. Xing, "Mechanical characteristics of wood, ceramic, metal and carbon fiber-based PLA composites fabricated by FDM," *J. Mater. Res. Technol.*, vol. 8, no. 5, pp. 3741–3751, Sep. 2019, doi: 10.1016/j.jmrt.2019.06.034.

[56] N. S. Hmeidat, R. C. Pack, S. J. Talley, R. B. Moore, and B. G. Compton, "Mechanical anisotropy in polymer composites produced by material extrusion additive manufacturing," *Addit. Manuf.*, vol. 34, p. 101385, Aug. 2020, doi: 10.1016/j.addma.2020.101385.

[57] P. Zhuo, S. Li, I. A. Ashcroft, and A. I. Jones, "Material extrusion additive manufacturing of continuous fibre reinforced polymer matrix composites: A review and outlook," *Compos. Part B Eng.*, vol. 224, p. 109143, Nov. 2021, doi: 10.1016/j.compositesb.2021.109143.

[58] Y. Jin, H. Li, Y. He, and J. Fu, "Quantitative analysis of surface profile in fused deposition modelling," *Addit. Manuf.*, vol. 8, pp. 142–148, Oct. 2015, doi: 10.1016/j.addma.2015.10.001.

[59] "Official Creality Ender 3 3D Printer Fully Open Source with Resume Printing Function DIY 3D Printers Printing Size 8.66x8.66x9.84 inch: Amazon.com: Industrial & Scientific." https://www.amazon.com/Comgrow-Creality-Ender-Aluminum-220x220x250mm/dp/B07BR3F9N6/ref=asc_df_B07BR3F9N6/?tag=hyprod-20&linkCode=df0&hvadid=312378702476&hvpos=&hvnetw=g&hvrand=1019232168232

4807279&hvpone=&hvptwo=&hvqmt=&hvdev=c&hvdvcmdl=&hvlocint=&hvlocphy=9028683&hvtargid=pla-452985168135&psc=1 (accessed Apr. 19, 2023).

[60] F. Clemens, F. Sarraf, A. Borzì, A. Neels, and A. Hadian, "Material extrusion additive manufacturing of advanced ceramics: Towards the production of large components," *J. Eur. Ceram. Soc.*, vol. 43, no. 7, pp. 2752–2760, Jul. 2023, doi: 10.1016/j.jeurceramsoc.2022.10.019.

[61] A. Cañadilla, A. Romero, G. P. Rodríguez, M. Á. Caminero, and Ó. J. Dura, "Mechanical, Electrical, and Thermal Characterization of Pure Copper Parts Manufactured via Material Extrusion Additive Manufacturing," *Materials*, vol. 15, no. 13, Art. no. 13, Jan. 2022, doi: 10.3390/ma15134644.

[62] A. R. Torrado, C. M. Shemelya, J. D. English, Y. Lin, R. B. Wicker, and D. A. Roberson, "Characterizing the effect of additives to ABS on the mechanical property anisotropy of specimens fabricated by material extrusion 3D printing," *Addit. Manuf.*, vol. 6, pp. 16–29, Apr. 2015, doi: 10.1016/j.addma.2015.02.001.

[63] J. Gonzalez-Gutierrez, S. Cano, S. Schuschnigg, C. Kukla, J. Sapkota, and C. Holzer, "Additive Manufacturing of Metallic and Ceramic Components by the Material Extrusion of Highly-Filled Polymers: A Review and Future Perspectives," *Materials*, vol. 11, no. 5, Art. no. 5, May 2018, doi: 10.3390/ma11050840.

[64] S. C. Altıparmak, V. A. Yardley, Z. Shi, and J. Lin, "Extrusion-based additive manufacturing technologies: State of the art and future perspectives," *J. Manuf. Process.*, vol. 83, pp. 607–636, Nov. 2022, doi: 10.1016/j.jmapro.2022.09.032.

[65] I. J. Solomon, P. Sevvel, and J. Gunasekaran, “A review on the various processing parameters in FDM,” *Mater. Today Proc.*, vol. 37, pp. 509–514, Jan. 2021, doi: 10.1016/j.matpr.2020.05.484.

[66] “BAAM.” http://wwwassets.e-ci.com/PDF/Products/baam-fact-sheet.pdf (accessed Apr. 27, 2023).

[67] “Ender-3 3D Printer,” *creality*. https://www.creality.com/products/ender-3-3d-printer (accessed Apr. 28, 2023).

[68] F. M. Mwema and E. T. Akinlabi, “Basics of Fused Deposition Modelling (FDM),” *Fused Depos. Model.*, pp. 1–15, May 2020, doi: 10.1007/978-3-030-48259-6_1.

[69] Y. Tlegenov, W. F. Lu, and G. S. Hong, “A dynamic model for current-based nozzle condition monitoring in fused deposition modelling,” *Prog. Addit. Manuf.*, vol. 4, no. 3, pp. 211–223, Sep. 2019, doi: 10.1007/s40964-019-00089-3.

[70] P. Czyżewski, D. Marciniak, B. Nowinka, M. Borowiak, and M. Bieliński, “Influence of Extruder’s Nozzle Diameter on the Improvement of Functional Properties of 3D-Printed PLA Products,” *Polymers*, vol. 14, no. 2, p. 356, Jan. 2022, doi: 10.3390/polym14020356.

[71] J. Triyono, H. Sukanto, R. M. Saputra, and D. F. Smaradhana, “The effect of nozzle hole diameter of 3D printing on porosity and tensile strength parts using polylactic acid material,” *Open Eng.*, vol. 10, no. 1, pp. 762–768, Jan. 2020, doi: 10.1515/eng-2020-0083.

[72] Md. Q. Tanveer, A. Haleem, and M. Suhaib, “Effect of variable infill density on mechanical behaviour of 3-D printed PLA specimen: an experimental investigation,” *SN Appl. Sci.*, vol. 1, no. 12, p. 1701, Nov. 2019, doi: 10.1007/s42452-019-1744-1.

[73] V. Kishore *et al.*, “Infrared preheating to improve interlayer strength of big area additive manufacturing (BAAM) components,” *Addit. Manuf.*, vol. 14, pp. 7–12, Mar. 2017, doi: 10.1016/j.addma.2016.11.008.

[74] E. Sachs, M. Cima, and J. Cornie, “Three-Dimensional Printing: Rapid Tooling and Prototypes Directly from a CAD Model,” *CIRP Ann.*, vol. 39, no. 1, pp. 201–204, Jan. 1990, doi: 10.1016/S0007-8506(07)61035-X.

[75] I. Gibson, D. Rosen, B. Stucker, and M. Khorasani, “Binder Jetting,” in *Additive Manufacturing Technologies*, I. Gibson, D. Rosen, B. Stucker, and M. Khorasani, Eds., Cham: Springer International Publishing, 2021, pp. 237–252. doi: 10.1007/978-3-030-56127-7_8.

[76] D. Oropeza and A. J. Hart, “A laboratory-scale binder jet additive manufacturing testbed for process exploration and material development,” *Int. J. Adv. Manuf. Technol.*, vol. 114, no. 11, pp. 3459–3473, Jun. 2021, doi: 10.1007/s00170-021-07123-1.

[77] D. Oropeza and A. J. Hart, “Reactive binder jet additive manufacturing for microstructural control and dimensional stability of ceramic materials,” *Addit. Manuf.*, vol. 48, p. 102448, Dec. 2021, doi: 10.1016/j.addma.2021.102448.

[78] A. Malas, D. Isakov, K. Couling, and G. J. Gibbons, “Fabrication of High Permittivity Resin Composite for Vat Photopolymerization 3D Printing: Morphology, Thermal, Dynamic Mechanical and Dielectric Properties,” *Materials*, vol. 12, no. 23, p. 3818, Nov. 2019, doi: 10.3390/ma12233818.

[79] J. Gonzalez-Gutierrez, F. Arbeiter, T. Schlauf, C. Kukla, and C. Holzer, “Tensile properties of sintered 17-4PH stainless steel fabricated by material extrusion additive manufacturing,” *Mater. Lett.*, vol. 248, pp. 165–168, Aug. 2019, doi: 10.1016/j.matlet.2019.04.024.

[80] M. Salmi, “Additive Manufacturing Processes in Medical Applications,” *Materials*, vol. 14, no. 1, Art. no. 1, Jan. 2021, doi: 10.3390/ma14010191.

[81] W. Du, X. Ren, Z. Pei, and C. Ma, “Ceramic Binder Jetting Additive Manufacturing: A Literature Review on Density,” *J. Manuf. Sci. Eng.*, vol. 142, no. 4, Feb. 2020, doi: 10.1115/1.4046248.

[82] M. Bhuvanesh Kumar and P. Sathiya, “Methods and materials for additive manufacturing: A critical review on advancements and challenges,” *Thin-Walled Struct.*, vol. 159, p. 107228, Feb. 2021, doi: 10.1016/j.tws.2020.107228.

[83] A. Mostafaei *et al.*, “Binder jet 3D printing—Process parameters, materials, properties, modeling, and challenges,” *Prog. Mater. Sci.*, vol. 119, p. 100707, Jun. 2021, doi: 10.1016/j.pmatsci.2020.100707.

[84] W. E. Frazier, “Metal Additive Manufacturing: A Review,” *J. Mater. Eng. Perform.*, vol. 23, no. 6, pp. 1917–1928, Jun. 2014, doi: 10.1007/s11665-014-0958-z.

[85] Z. Zhang, L. Wang, L. Zhang, P. Ma, B. Lu, and C. Du, “Binder jetting 3D printing process optimization for rapid casting of green parts with high tensile strength,” *China Foundry*, vol. 18, no. 4, pp. 335–343, Jul. 2021, doi: 10.1007/s41230-021-1057-z.

[86] M. Ziaee and N. B. Crane, “Binder jetting: A review of process, materials, and methods,” *Addit. Manuf.*, vol. 28, pp. 781–801, Aug. 2019, doi: 10.1016/j.addma.2019.05.031.

[87] A. Lores, N. Azurmendi, I. Agote, and E. Zuza, “A review on recent developments in binder jetting metal additive manufacturing: materials and process characteristics,” *Powder Metall.*, vol. 62, no. 5, pp. 267–296, Oct. 2019, doi: 10.1080/00325899.2019.1669299.

[88] S. Sadeghi Borujeni, G. S. Saluja, and V. Ploshikhin, “Compensation of sintering deformation for components manufactured by metal binder jetting using numerical

simulations," *Rapid Prototyp. J.*, vol. 29, no. 3, pp. 612–625, Jan. 2022, doi: 10.1108/RPJ-06-2022-0181.

[89] B. J. Paudel, D. Conover, J.-K. Lee, and A. C. To, "A computational framework for modeling distortion during sintering of binder jet printed parts," *J. Micromechanics Mol. Phys.*, vol. 06, no. 04, pp. 95–102, Dec. 2021, doi: 10.1142/S242491302142008X.

[90] N. Lecis *et al.*, "Effects of process parameters, debinding and sintering on the microstructure of 316L stainless steel produced by binder jetting," *Mater. Sci. Eng. A*, vol. 828, p. 142108, Nov. 2021, doi: 10.1016/j.msea.2021.142108.

[91] H. Miyanaji, K. M. Rahman, M. Da, and C. B. Williams, "Effect of fine powder particles on quality of binder jetting parts," *Addit. Manuf.*, vol. 36, p. 101587, Dec. 2020, doi: 10.1016/j.addma.2020.101587.

[92] M. Mariani *et al.*, "Mechanical and microstructural characterization of WC-Co consolidated by binder jetting additive manufacturing," *Int. J. Refract. Met. Hard Mater.*, vol. 100, p. 105639, Nov. 2021, doi: 10.1016/j.ijrmhm.2021.105639.

[93] I. Gibson, D. Rosen, B. Stucker, and M. Khorasani, "Directed Energy Deposition," in *Additive Manufacturing Technologies*, I. Gibson, D. Rosen, B. Stucker, and M. Khorasani, Eds., Cham: Springer International Publishing, 2021, pp. 285–318. doi: 10.1007/978-3-030-56127-7_10.

[94] D. Svetlizky *et al.*, "Directed energy deposition (DED) additive manufacturing: Physical characteristics, defects, challenges and applications," *Mater. Today*, vol. 49, pp. 271–295, Oct. 2021, doi: 10.1016/j.mattod.2021.03.020.

[95] D.-G. Ahn, "Directed Energy Deposition (DED) Process: State of the Art," *Int. J. Precis. Eng. Manuf.-Green Technol.*, vol. 8, no. 2, pp. 703–742, Mar. 2021, doi: 10.1007/s40684-020-00302-7.

[96] J. L. Dávila, P. I. Neto, P. Y. Noritomi, R. T. Coelho, and J. V. L. da Silva, "Hybrid manufacturing: a review of the synergy between directed energy deposition and subtractive processes," *Int. J. Adv. Manuf. Technol.*, vol. 110, no. 11, pp. 3377–3390, Oct. 2020, doi: 10.1007/s00170-020-06062-7.

[97] B. Li, C. Han, C. W. J. Lim, and K. Zhou, "Interface formation and deformation behaviors of an additively manufactured nickel-aluminum-bronze/15-5 PH multimaterial via laser-powder directed energy deposition," *Mater. Sci. Eng. A*, vol. 829, p. 142101, Jan. 2022, doi: 10.1016/j.msea.2021.142101.

[98] C. Schneider-Maunoury, L. Weiss, P. Acquier, D. Boisselier, and P. Laheurte, "Functionally graded Ti6Al4V-Mo alloy manufactured with DED-CLAD® process," *Addit. Manuf.*, vol. 17, pp. 55–66, Oct. 2017, doi: 10.1016/j.addma.2017.07.008.

[99] M. Rauch, J.-Y. Hascoët, and M. Mallaiah, "Repairing Ti-6Al-4V aeronautical components with DED additive manufacturing," *MATEC Web Conf.*, vol. 321, p. 03017, 2020, doi: 10.1051/matecconf/202032103017.

[100] A. Saboori, A. Aversa, G. Marchese, S. Biamino, M. Lombardi, and P. Fino, "Application of Directed Energy Deposition-Based Additive Manufacturing in Repair," *Appl. Sci.*, vol. 9, no. 16, Art. no. 16, Jan. 2019, doi: 10.3390/app9163316.

[101] "Metal-AM-Selection-Guide.pdf." https://optomec.com/wp-content/uploads/2019/06/Metal-AM-Selection-Guide.pdf (accessed May 27, 2023).

[102] "NASA looks to large-scale DED Additive Manufacturing for future rocket engines," *Metal AM magazine*, Sep. 18, 2020. https://www.metal-am.com/nasa-looks-to-large-scale-ded-additive-manufacturing-for-future-rocket-engines/ (accessed May 27, 2023).

[103] "What is Directed Energy Deposition (DED)?" https://www.twi-global.com/technical-knowledge/faqs/directed-energy-deposition.aspx (accessed May 27, 2023).

[104] "eos_system_data_sheet_eos_m_290_en.pdf." https://www.eos.info/03_system-related-assets/system-related-contents/_pdf_system-data-sheets/eos_system_data_sheet_eos_m_290_en.pdf (accessed May 27, 2023).

[105] "Electron Beam Melting (EBM)." http://additivemanufacturingllc.com/services/electron-beam-melting/#:~:text=The%20EBM%20machine%20uses%20an,that%20have%20homogeneous%20material%20structure. (accessed May 27, 2023).

[106] "(PDF) Additive manufacturing of 3D nano-architected metals." https://www.researchgate.net/publication/323072377_Additive_manufacturing_of_3D_nano-architected_metals (accessed May 27, 2023).

[107] J. Mi *et al.*, "In-situ monitoring laser based directed energy deposition process with deep convolutional neural network," *J. Intell. Manuf.*, vol. 34, no. 2, pp. 683–693, Feb. 2023, doi: 10.1007/s10845-021-01820-0.

[108] S. I. Kim, H. Y. Jung, S. Yang, J. Yoon, H. Lee, and W. Ryu, "3D Printing of a miniature turbine blade model with an embedded fibre Bragg grating sensor for high-temperature monitoring," *Virtual Phys. Prototyp.*, vol. 17, no. 2, pp. 156–169, Apr. 2022, doi: 10.1080/17452759.2021.2017545.

[109] S. M. T. Omar and K. P. Plucknett, “The influence of DED process parameters and heat-treatment cycle on the microstructure and hardness of AISI D2 tool steel,” *J. Manuf. Process.*, vol. 81, pp. 655–671, Sep. 2022, doi: 10.1016/j.jmapro.2022.06.069.

[110] I. Gibson, D. Rosen, B. Stucker, and M. Khorasani, “Hybrid Additive Manufacturing,” in *Additive Manufacturing Technologies*, Springer, Cham, 2021, pp. 347–366. doi: 10.1007/978-3-030-56127-7_12.

[111] “The unrealised potential of Electron Beam Powder Bed Fusion 3D printing,” *Metal AM magazine*, Jul. 15, 2020. https://www.metal-am.com/articles/unrealised-potential-the-story-and-status-of-electron-beam-powder-bed-fusion-3d-printing/ (accessed May 27, 2023).

[112] “Empa - Coating Competence Center - Selective Laser Melting (SLM).” https://www.empa.ch/web/coating-competence-center/selective-laser-melting (accessed May 27, 2023).

[113] L. Murr, S. Gaytan, E. Martinez, F. Medina, and R. Wicker, “Next Generation Orthopaedic Implants by Additive Manufacturing Using Electron Beam Melting,” *Int. J. Biomater.*, vol. 2012, p. 245727, Aug. 2012, doi: 10.1155/2012/245727.

[114] S. Chowdhury *et al.*, “Laser powder bed fusion: a state-of-the-art review of the technology, materials, properties & defects, and numerical modelling,” *J. Mater. Res. Technol.*, vol. 20, pp. 2109–2172, Sep. 2022, doi: 10.1016/j.jmrt.2022.07.121.

[115] M. Xu, H. Guo, Y. Wang, Y. Hou, Z. Dong, and L. Zhang, “Mechanical properties and microstructural characteristics of 316L stainless steel fabricated by laser powder bed fusion and binder jetting,” *J. Mater. Res. Technol.*, vol. 24, pp. 4427–4439, May 2023, doi: 10.1016/j.jmrt.2023.04.069.

[116] N. Hrabe, T. Gnäupel-Herold, and T. Quinn, "Fatigue properties of a titanium alloy (Ti–6Al–4V) fabricated via electron beam melting (EBM): Effects of internal defects and residual stress," *Int. J. Fatigue*, vol. 94, pp. 202–210, Jan. 2017, doi: 10.1016/j.ijfatigue.2016.04.022.

[117] F. Ceccanti, A. Giorgetti, and P. Citti, "A Support Structure Design Strategy for Laser Powder Bed Fused Parts," *Procedia Struct. Integr.*, vol. 24, pp. 667–679, Jan. 2019, doi: 10.1016/j.prostr.2020.02.059.

[118] D. Morgan, E. Agba, and C. Hill, "Support Structure Development and Initial Results for Metal Powder Bed Fusion Additive Manufacturing," *Procedia Manuf.*, vol. 10, pp. 819–830, Jan. 2017, doi: 10.1016/j.promfg.2017.07.083.

[119] "EOS M 400-4 - Ultra Fast 3D Printing." https://www.eos.info/en/industrial-3d-printer/metal/eos-m-400-4 (accessed May 28, 2023).

[120] "GE Additive Arcam EBM Spectra L review - industrial 3D printer," *Aniwaa*. https://www.aniwaa.com/product/3d-printers/ge-additive-arcam-ebm-spectra-l/ (accessed May 28, 2023).

[121] "557XR Laser Deposition System," *RPM Innovations*. https://www.rpm-innovations.com/laser-deposition-systems-557xr.html (accessed May 28, 2023).

[122] "How Much Does a Metal 3D Printer Cost?," *All3DP Pro*, Apr. 08, 2023. https://all3dp.com/2/how-much-does-a-metal-3d-printer-cost/ (accessed May 28, 2023).

[123] "EOS Price." https://www.treatstock.com/ (accessed May 28, 2023).

[124] "How Much Does a Metal 3D Printer Cost?" https://www.xometry.com/resources/3d-printing/metal-3d-printer-cost/ (accessed May 28, 2023).

[125] L. Mugwagwa, I. Yadroitsava, N. W. Makoana, and I. Yadroitsev, “9 - Residual stress in laser powder bed fusion,” in *Fundamentals of Laser Powder Bed Fusion of Metals*, I. Yadroitsev, I. Yadroitsava, A. du Plessis, and E. MacDonald, Eds., in Additive Manufacturing Materials and Technologies. Elsevier, 2021, pp. 245–276. doi: 10.1016/B978-0-12-824090-8.00014-7.

[126] N. Nadammal *et al.*, “Critical role of scan strategies on the development of microstructure, texture, and residual stresses during laser powder bed fusion additive manufacturing,” *Addit. Manuf.*, vol. 38, p. 101792, Feb. 2021, doi: 10.1016/j.addma.2020.101792.

[127] J. Robinson, I. Ashton, P. Fox, E. Jones, and C. Sutcliffe, “Determination of the effect of scan strategy on residual stress in laser powder bed fusion additive manufacturing,” *Addit. Manuf.*, vol. 23, pp. 13–24, Oct. 2018, doi: 10.1016/j.addma.2018.07.001.

[128] M. S. Knieps, W. J. Reynolds, J. Dejaune, A. T. Clare, and A. Evirgen, “In-situ alloying in powder bed fusion: The role of powder morphology,” *Mater. Sci. Eng. A*, vol. 807, p. 140849, Mar. 2021, doi: 10.1016/j.msea.2021.140849.

[129] A. Mussatto, R. Groarke, A. O’Neill, M. A. Obeidi, Y. Delaure, and D. Brabazon, “Influences of powder morphology and spreading parameters on the powder bed topography uniformity in powder bed fusion metal additive manufacturing,” *Addit. Manuf.*, vol. 38, p. 101807, Feb. 2021, doi: 10.1016/j.addma.2020.101807.

[130] S. E. Brika, M. Letenneur, C. A. Dion, and V. Brailovski, “Influence of particle morphology and size distribution on the powder flowability and laser powder bed fusion manufacturability of Ti-6Al-4V alloy,” *Addit. Manuf.*, vol. 31, p. 100929, Jan. 2020, doi: 10.1016/j.addma.2019.100929.

[131] E. Malekipour and H. El-Mounayri, “Common defects and contributing parameters in powder bed fusion AM process and their classification for online monitoring and control: a review,” *Int. J. Adv. Manuf. Technol.*, vol. 95, no. 1, pp. 527–550, Mar. 2018, doi: 10.1007/s00170-017-1172-6.

[132] D. J. Huang and H. Li, “A machine learning guided investigation of quality repeatability in metal laser powder bed fusion additive manufacturing,” *Mater. Des.*, vol. 203, p. 109606, May 2021, doi: 10.1016/j.matdes.2021.109606.

[133] J. P. Oliveira, A. D. LaLonde, and J. Ma, “Processing parameters in laser powder bed fusion metal additive manufacturing,” *Mater. Des.*, vol. 193, p. 108762, Aug. 2020, doi: 10.1016/j.matdes.2020.108762.

[134] R. Esmaeilizadeh *et al.*, “On the effect of laser powder-bed fusion process parameters on quasi-static and fatigue behaviour of Hastelloy X: A microstructure/defect interaction study,” *Addit. Manuf.*, vol. 38, p. 101805, Feb. 2021, doi: 10.1016/j.addma.2020.101805.

[135] S. Cao, Y. Zou, C. V. S. Lim, and X. Wu, “Review of laser powder bed fusion (LPBF) fabricated Ti-6Al-4V: process, post-process treatment, microstructure, and property,” *Light Adv. Manuf.*, vol. 2, no. 2, p. 1, 2021, doi: 10.37188/lam.2021.020.

[136] J. K. Veetil *et al.*, “Build position-based dimensional deviations of laser powder-bed fusion of stainless steel 316L,” *Precis. Eng.*, vol. 67, pp. 58–68, Jan. 2021, doi: 10.1016/j.precisioneng.2020.09.024.

[137] M. Kahlin *et al.*, “Improved fatigue strength of additively manufactured Ti6Al4V by surface post processing,” *Int. J. Fatigue*, vol. 134, p. 105497, May 2020, doi: 10.1016/j.ijfatigue.2020.105497.

[138] S. Shrestha and K. Chou, “Formation of keyhole and lack of fusion pores during the laser powder bed fusion process,” *Manuf. Lett.*, vol. 32, pp. 19–23, Apr. 2022, doi: 10.1016/j.mfglet.2022.01.005.

[139] J. G. Santos Macías, C. Elangeswaran, L. Zhao, J.-Y. Buffière, B. Van Hooreweder, and A. Simar, “Fatigue crack nucleation and growth in laser powder bed fusion AlSi10Mg under as built and post-treated conditions,” *Mater. Des.*, vol. 210, p. 110084, Nov. 2021, doi: 10.1016/j.matdes.2021.110084.

[140] S. Coeck, M. Bisht, J. Plas, and F. Verbist, “Prediction of lack of fusion porosity in selective laser melting based on melt pool monitoring data,” *Addit. Manuf.*, vol. 25, pp. 347–356, Jan. 2019, doi: 10.1016/j.addma.2018.11.015.

[141] S. Ziri, A. Hor, and C. Mabru, “Effect of powder size and processing parameters on surface, density and mechanical properties of 316L elaborated by Laser Powder Bed Fusion,” *https://popups.uliege.be/esaform21*, Apr. 05, 2021. https://popups.uliege.be/esaform21/index.php?id=1563 (accessed May 29, 2023).

[142] “How process parameters drive successful metal AM part production,” *Metal AM magazine*, Jun. 01, 2018. https://www.metal-am.com/articles/70927-2/ (accessed May 29, 2023).

[143] W. E. King *et al.*, “Observation of keyhole-mode laser melting in laser powder-bed fusion additive manufacturing,” *J. Mater. Process. Technol.*, vol. 214, no. 12, pp. 2915–2925, Dec. 2014, doi: 10.1016/j.jmatprotec.2014.06.005.

[144] X. Yang, Y. Li, and B. Li, “Formation mechanisms of lack of fusion and keyhole-induced pore defects in laser powder bed fusion process: A numerical study,” *Int. J. Therm. Sci.*, vol. 188, p. 108221, Jun. 2023, doi: 10.1016/j.ijthermalsci.2023.108221.

[145] L. Guo *et al.*, “Understanding keyhole induced-porosities in laser powder bed fusion of aluminum and elimination strategy,” *Int. J. Mach. Tools Manuf.*, vol. 184, p. 103977, Jan. 2023, doi: 10.1016/j.ijmachtools.2022.103977.

[146] F. H. Kim and S. P. Moylan, “Literature review of metal additive manufacturing defects,” National Institute of Standards and Technology, Gaithersburg, MD, NIST AMS 100-16, May 2018. doi: 10.6028/NIST.AMS.100-16.

[147] M. Balbaa, S. Mekhiel, M. Elbestawi, and J. McIsaac, “On selective laser melting of Inconel 718: Densification, surface roughness, and residual stresses,” *Mater. Des.*, May 2020, doi: 10.1016/j.matdes.2020.108818.

[148] J.-B. Forien, N. P. Calta, P. J. DePond, G. M. Guss, T. T. Roehling, and M. J. Matthews, “Detecting keyhole pore defects and monitoring process signatures during laser powder bed fusion: A correlation between in situ pyrometry and ex situ X-ray radiography,” *Addit. Manuf.*, vol. 35, p. 101336, Oct. 2020, doi: 10.1016/j.addma.2020.101336.

[149] H. Hyer *et al.*, “Understanding the Laser Powder Bed Fusion of AlSi10Mg Alloy,” *Metallogr. Microstruct. Anal.*, vol. 9, Jul. 2020, doi: 10.1007/s13632-020-00659-w.

[150] H. Gong, K. Rafi, H. Gu, G. D. Janaki Ram, T. Starr, and B. Stucker, “Influence of defects on mechanical properties of Ti–6Al–4V components produced by selective laser melting and electron beam melting,” *Mater. Des.*, vol. 86, pp. 545–554, Dec. 2015, doi: 10.1016/j.matdes.2015.07.147.

[151] N. O. Larrosa *et al.*, “Linking microstructure and processing defects to mechanical properties of selectively laser melted AlSi10Mg alloy,” *Theor. Appl. Fract. Mech.*, vol. 98, pp. 123–133, Dec. 2018, doi: 10.1016/j.tafmec.2018.09.011.

[152] A. Hilaire, E. Andrieu, and X. Wu, “High-temperature mechanical properties of alloy 718 produced by laser powder bed fusion with different processing parameters,” *Addit. Manuf.*, vol. 26, pp. 147–160, Mar. 2019, doi: 10.1016/j.addma.2019.01.012.

[153] D. L. Butler, “Surface Roughness Measurement,” in *Encyclopedia of Microfluidics and Nanofluidics*, D. Li, Ed., Boston, MA: Springer US, 2008, pp. 1945–1949. doi: 10.1007/978-0-387-48998-8_1506.

[154] A. H. Chern *et al.*, “Build orientation, surface roughness, and scan path influence on the microstructure, mechanical properties, and flexural fatigue behavior of Ti–6Al–4V fabricated by electron beam melting,” *Mater. Sci. Eng. A*, vol. 772, p. 138740, Jan. 2020, doi: 10.1016/j.msea.2019.138740.

[155] E. Santecchia *et al.*, “A Review on Fatigue Life Prediction Methods for Metals,” *Adv. Mater. Sci. Eng.*, vol. 2016, p. e9573524, Sep. 2016, doi: 10.1155/2016/9573524.

[156] Z. Sun *et al.*, “Experimental study of microstructure changes due to low cycle fatigue of a steel nanocrystallised by Surface Mechanical Attrition Treatment (SMAT),” *Mater. Charact.*, vol. 124, pp. 117–121, Feb. 2017, doi: 10.1016/j.matchar.2016.12.017.

[157] A. P. Mouritz, Ed., “20 - Fatigue of aerospace materials,” in *Introduction to Aerospace Materials*, Woodhead Publishing, 2012, pp. 469–497. doi: 10.1533/9780857095152.469.

[158] M. Böhm and K. Głowacka, “Fatigue Life Estimation with Mean Stress Effect Compensation for Lightweight Structures—The Case of GLARE 2 Composite,” *Polymers*, vol. 12, no. 2, p. 251, Jan. 2020, doi: 10.3390/polym12020251.

[159] “Description of a S-N Curve – Fatec Engineering.” https://www.fatec-engineering.com/2018/02/20/description-of-a-s-n-curve/ (accessed Jun. 04, 2023).

[160] D. B. Marghitu, C. I. Diaconescu, and B. O. Ciocirlan, “3 - Mechanics of Materials,” in *Mechanical Engineer’s Handbook*, D. B. Marghitu, Ed., in Academic Press Series in Engineering. San Diego: Academic Press, 2001, pp. 119–188. doi: 10.1016/B978-012471370-3/50004-8.

[161] S. Manson and M. Hirschberg, “Fatigue: an interdisciplinary approach,” *Syracuse Univ. N. Y.*, 1964.

[162] “Low Cycle Fatigue,” *Metal Fatigue Life Prediction*. https://fatigue-life.com/low-cycle-fatigue/ (accessed Jun. 05, 2023).

[163] V. M. Kaoushik, U. Nichul, V. Chavan, and V. Hiwarkar, “Development of microstructure and high hardness of Ti6Al4V alloy fabricated using laser beam powder bed fusion: A novel sub-transus heat treatment approach,” *J. Alloys Compd.*, vol. 937, p. 168387, Mar. 2023, doi: 10.1016/j.jallcom.2022.168387.

Vita

I am a Mechanical Engineering graduate with a Bachelor of Science degree from the University of Texas at El Paso, located in El Paso, Texas. I earned my degree in May 2020, and my academic journey has been filled with research and teaching experiences. Throughout my master's coursework, I had the opportunity to work as a Graduate Research Assistant at the prestigious W.M. Keck Center, affiliated with the University of Texas at El Paso. During this period, I delved into the fascinating realm of advanced additive manufacturing techniques. Collaborating with a team of experts, we explored the development of innovative 3D printing materials and processes. Additionally, I contributed to the academic community by serving as a Teaching Assistant (TA) at the University of Texas at El Paso. As a TA, I mentored and supported students in grasping the fundamentals of Computer-Aided Design (CAD). My responsibilities included lecturing and offering personalized assistance to students who required further guidance.

Contact Information: bramirez16@miners.utep.edu